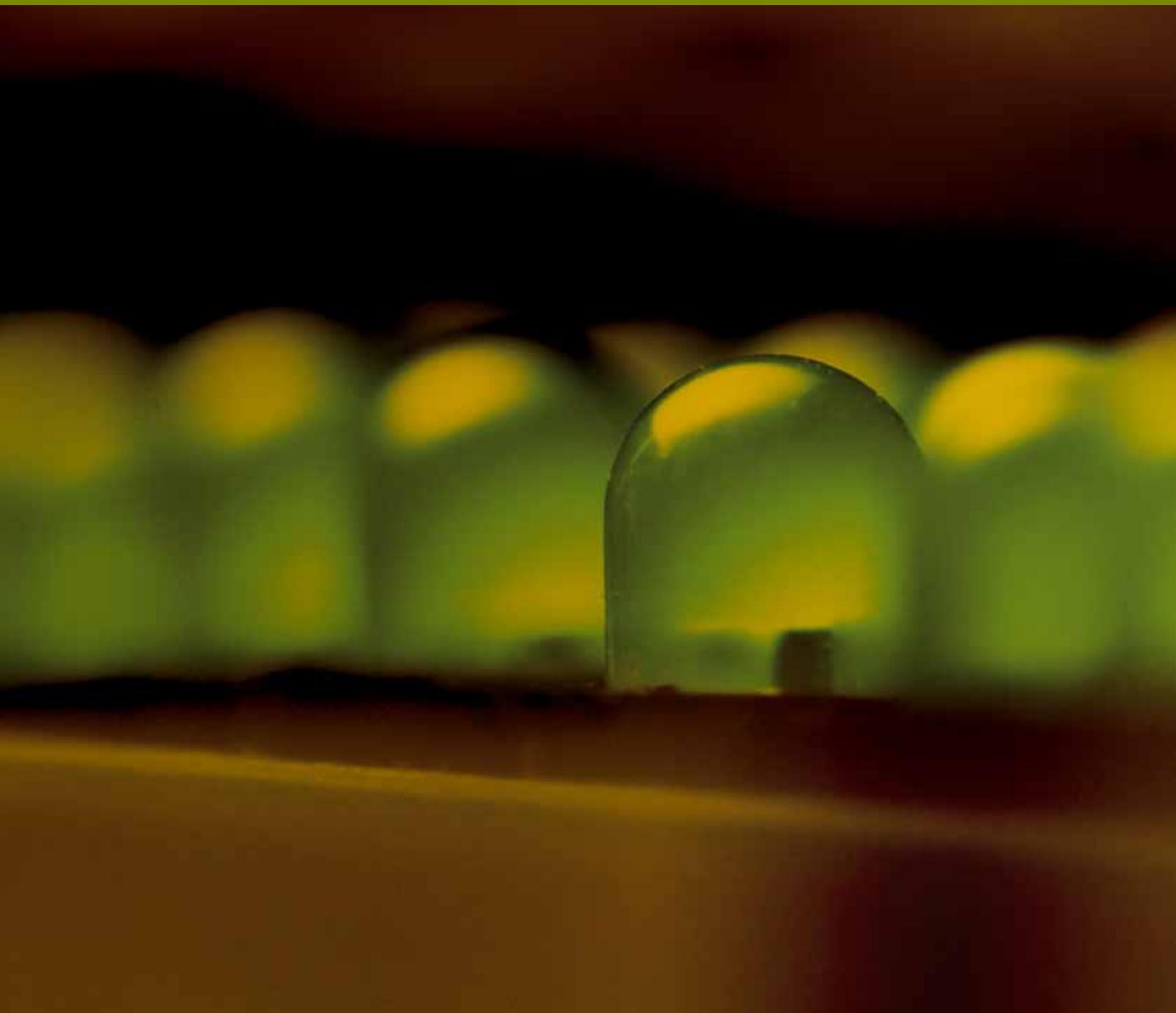


Advances in OptoElectronics

Optical Waveguides and Resonant Cavities

Guest Editors: Ana Vukovic, Martin Cryan,
Snjezana Tomljenovic-Hanic, and Jun Shibayama





Optical Waveguides and Resonant Cavities

Advances in OptoElectronics

Optical Waveguides and Resonant Cavities

Guest Editors: Ana Vukovic, Martin Cryan,
Snjezana Tomljenovic-Hanic, and Jun Shibayama



Copyright © 2011 Hindawi Publishing Corporation. All rights reserved.

This is a special issue published in volume 2011 of “Advances in OptoElectronics.” All articles are open access articles distributed under the Creative Commons Attribution License, which permits unrestricted use, distribution, and reproduction in any medium, provided the original work is properly cited.

Editorial Board

Armin G. Aberle, Singapore
Ralf Bergmann, Germany
Xian An Cao, USA
Wen-Chang Chen, Taiwan
Philippe Goldner, France
Jung Y. Huang, Taiwan
Anthony J. Kenyon, UK

Yaomin Lin, USA
Wenning Liu, USA
Yalin Lu, USA
Alfred Margaryan, USA
Samir K Mondal, India
Satishchandra B. Ogale, India
Adrian Podoleanu, UK

Lucimara Stolz Roman, Brazil
Jayanta K. Sahu, UK
Somenath N. Sarkar, India
Vasily Spirin, Mexico
Chang Q. Sun, Singapore
Yuqin Zong, USA

Contents

Optical Waveguides and Resonant Cavities, Ana Vukovic, Martin Cryan, Snjezana Tomljenovic-Hanic, and Jun Shibayama

Volume 2011, Article ID 393980, 2 pages

A TM-Pass/TE-Stop Polarizer Based on a Surface Plasmon Resonance, Yuu Wakabayashi, Junji Yamauchi, and Hisamatsu Nakano

Volume 2011, Article ID 867271, 6 pages

Analysis of Plasmonic Waveguides and Gratings Using Implicit Finite-Difference Methods, Jun Shibayama, Junji Yamauchi, and Hisamatsu Nakano

Volume 2011, Article ID 287284, 6 pages

Oblique Du-Fort Frankel Beam Propagation Method, Ken Chan, Philip Sewell, Ana Vukovic, and Trevor Benson

Volume 2011, Article ID 196707, 6 pages

Controlled On-Chip Single-Photon Transfer Using Photonic Crystal Coupled-Cavity Waveguides, Hubert Pascal Seigneur, Matthew Weed, Michael Niklaus Leuenberger, and Winston Vaughan Schoenfeld

Volume 2011, Article ID 893086, 13 pages

Ultrabroadband Electro-Optic Modulator Based on Hybrid Silicon-Polymer Dual Vertical Slot Waveguide, Shouyuan Shi and Dennis W. Prather

Volume 2011, Article ID 714895, 6 pages

Microcavity Silicon Photodetectors at 1.55 μm , M. Casalino, G. Coppola, M. Giofrè, M. Iodice, L. Moretti, I. Rendina, and L. Sirleto

Volume 2011, Article ID 965967, 10 pages

Editorial

Optical Waveguides and Resonant Cavities

Ana Vukovic,¹ Martin Cryan,² Snjezana Tomljenovic-Hanic,³ and Jun Shibayama⁴

¹ George Green Institute for Electromagnetic Research, The University of Nottingham, Nottingham NG7 2RD, UK

² Department of Electrical and Electronic Engineering, University of Bristol, Bristol BS8 1UB, UK

³ School of Physics, The University of Melbourne, Parkville, VIC 3010, Australia

⁴ Faculty of Science and Engineering, Hosei University, 3-7-2 Kajino-cho, Koganei, Tokyo 184-8584, Japan

Correspondence should be addressed to Ana Vukovic, ana.vukovic@nottingham.ac.uk

Received 30 November 2010; Accepted 30 November 2010

Copyright © 2011 Ana Vukovic et al. This is an open access article distributed under the Creative Commons Attribution License, which permits unrestricted use, distribution, and reproduction in any medium, provided the original work is properly cited.

Optical waveguides and resonant cavities offer highly valuable ways of manipulating and processing light over short distances. Low loss propagation, efficient coupling to fibres, and ultracompact bends are paramount for creating low-cost photonics suitable for mass markets. Novel forms of waveguiding are being further exploited: photonic crystal waveguides have the potential for low loss guiding and exhibit slow light phenomena, and surface plasmon waveguides are increasingly used for sensing and imaging applications. Development of new devices is accelerated when strong links between research, development, and production are established, and in that process accurate numerical modelling is needed to reliably predict the performance and scope of a new device. This special issue reports on recent developments in design of photonic devices and addresses issues that need to be considered and approaches that need to be used for modelling purposes. In this special issue, we have invited a few papers that address these issues.

The first and second papers report on modelling and design of plasmonic-based devices. Plasmonic structures are very sensitive to design parameters and immediate environment and are ideal candidates for sensor devices. Furthermore, as plasmonics offers to integrate light with electronics on a single platform, large research is being conducted in the area of design and optimisation of a variety of optoelectronic devices. The first paper investigates two structures for the TM-pass/TE-stop surface plasmon polarizer. The first structure has a thin film sandwiched between periodic dielectric gratings. Numerical Finite Difference Time Domain (FDTD) method is used for analysis and optimisation and reports 94% transmission and an extinction ratio better than 17 dB. The second structure

addresses a more practical device in terms of fabrication in which a dielectric grating is sandwiched between two thin metal layers but reports reduced TM transmission and extinction ratio. The second paper compares the performance of various plasmonic waveguides and gratings using the Yee-mesh-based Beam-Propagation Method (YMBPM) and frequency-dependent FDTD method. Plasmonic waveguides are compared in terms of their effective index and propagation loss, whilst plasmonic gratings are compared in terms of their transmission spectrum. It is shown that the shape of the grating can greatly affect the transmission spectrum of a device.

The third paper considers modelling of photonic waveguides with oblique and tilted incidence in order to eliminate nonphysical staircasing noise that appears when Cartesian mesh is used. For this purpose, the oblique BPM method is implemented with Du-Fort Frankel scheme for fast computation. The implementation of the method is presented, and its accuracy and stability is compared with oblique Crank-Nicholson BPM method.

The fourth paper presents theoretical and numerical analysis of tunable photonic crystal coupled cavity waveguides for use in single photon transfer. The current challenge is to reduce the size of components for single photon manipulation by using either photonic crystals or plasmonics. The paper shows that useful performance could be achieved with coupled cavity waveguides and will act as an impetus to experimentalists in the field.

The fifth paper presents an improved design for CMOS compatible Electro-Optic (EO) modulator that combines lithium niobate and organic polymers on a silicon substrate. Combining these materials in the slot waveguide design

enables tight concentration of both RF and optical fields for maximum interaction and reports on reduced RF losses making the modulator applicable for RF frequencies of up to 250 GHz. The hybrid modelling method is used whereby the modelling of the optical signal is done using the frequency domain FDTD method, whilst for modelling of the RF signal Finite Element Method with adaptive meshing is used in order to accurately describe both the subwavelength and larger features of the modulator.

The final paper investigates design, characterization, and realization of silicon microcavity photodetectors operating at $1.55\text{ }\mu\text{m}$. The authors compare top- and back-illuminated configurations with a view to enhance the responsivity of the Schottky diode-based photodetectors.

Ana Vukovic
Martin Cryan
Snjezana Tomljenovic-Hanic
Jun Shibayama

Research Article

A TM-Pass/TE-Stop Polarizer Based on a Surface Plasmon Resonance

Yuu Wakabayashi, Junji Yamauchi, and Hisamatsu Nakano

Faculty of Engineering, Hosei University, 3-7-2 Kajino-cho, Koganei, Tokyo 184-8584, Japan

Correspondence should be addressed to Yuu Wakabayashi, yuu.wakabayashi.27@gs-eng.hosei.ac.jp

Received 15 June 2010; Accepted 16 July 2010

Academic Editor: Ana Vukovic

Copyright © 2011 Yuu Wakabayashi et al. This is an open access article distributed under the Creative Commons Attribution License, which permits unrestricted use, distribution, and reproduction in any medium, provided the original work is properly cited.

A TM-pass/TE-stop polarizer consisting of a metal film sandwiched between dielectric gratings is investigated using the finite-difference time-domain method. At normal incidence with respect to the grating plane, a transmissivity of more than 94% and a reflectivity of more than 98% are obtained at $\lambda = 1.55 \mu\text{m}$ for the TM and TE waves, respectively. The extinction ratio is more than 17 dB over a wavelength range of $1.50 \mu\text{m}$ to $1.75 \mu\text{m}$. A high extinction ratio is maintained at oblique incidence, although the wavelength range shifts towards longer wavelengths. The TM-pass/TE-stop operation is also achieved with a modified structure, in which a dielectric grating is sandwiched between metal films.

1. Introduction

There are a great number of papers devoted to the study of light propagation in periodic structures [1]. One of the important applications of the periodic structures is to construct a polarizer, which is used in optical communications and sensing devices. Recently, high transmission of the transverse magnetic (TM) wave through a thin metal film has been suggested and discussed [2–4]. The transmission is closely related to a surface plasmon (SP) resonance [5]. The SP resonance is realized using a thin metal film sandwiched between dielectric gratings. We should also note that recent interest has been directed toward plasmon waveguides operating at $\lambda \approx 1.55 \mu\text{m}$ (optical communication band) [6, 7].

In this paper, the SP-based enhanced transmission through a thin metal film is investigated in more detail in the optical communication band. The finite-difference time-domain (FDTD) method is used for the analysis. To obtain a high transmissivity for the TM wave and a high reflectivity for the transverse electric (TE) wave with a subsequent high extinction ratio (ER), we appropriately choose the width and thickness of the dielectric grating. In addition to normal incidence with respect to the grating plane, we consider the case of oblique incidence. It was found that the wavelength

range, in which the high ER is observed, shifts towards longer wavelengths.

To alleviate the fabrication difficulty, we also deal with a modified structure, in which a dielectric grating is sandwiched between metal films. The TM-pass/TE-stop operation is achieved at $\lambda = 1.55 \mu\text{m}$, although the transmissivity is low compared with that obtained from the original structure.

2. Configuration and Numerical Method

Figure 1 illustrates the periodic structure of the polarizer, in which a two-dimensional model is treated. The configuration is similar to that treated in [2, 3]. We illuminate a uniform plane wave of either the TE or the TM wave from the input side and intend to extract the TE wave as a reflected field at the input side and the TM wave as a transmission field at the output side. Note that from a different aspect, a similar structure was also investigated as a low-loss surface plasmon Bragg grating [8].

The refractive indices of the dielectric materials are taken to be $n_H = 3.715$ and $n_L = 2.049$. The width and thickness of the dielectric grating are designated as w and t_d , respectively. The widths of the low- and high-index dielectric regions

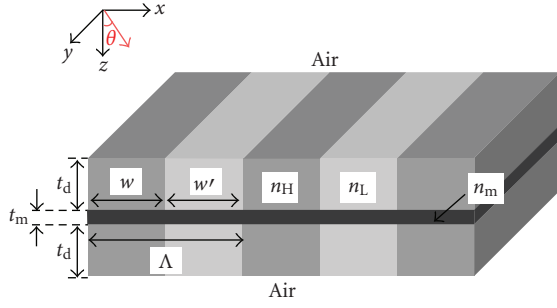
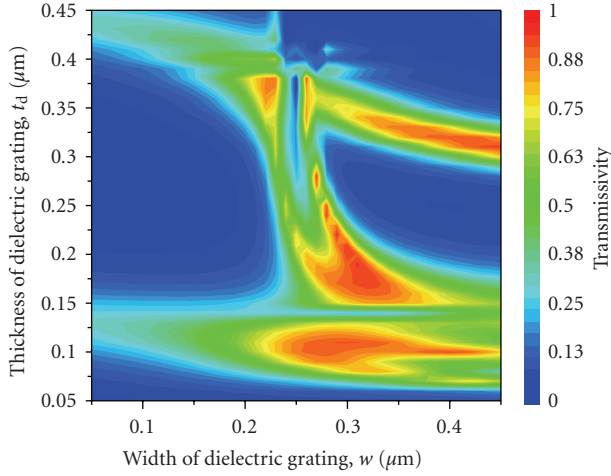


FIGURE 1: Configuration.

FIGURE 2: Transmissivity of TM wave ($\lambda = 1.55 \mu\text{m}$).

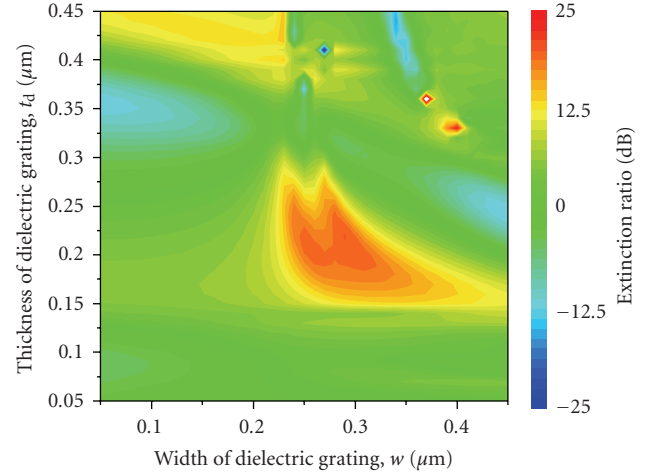
are set to be the same, that is, $w = w'$. The Drude model is used to express the dispersion of a metal. The refractive index and thickness of the metal (Ag) film are chosen to be $n_m = 0.144 - j11.214$ at $\lambda = 1.55 \mu\text{m}$ [9] and $t_m = 0.03 \mu\text{m}$.

To analyze the present polarizer, we adopt the FDTD method together with the periodic boundary condition, to which the field transformation technique [10] is applied. The piecewise linear recursive convolution technique [11] is employed so as to treat the structure involving the metal film. The numerical parameters are chosen to be $\Delta x = \Delta z = 5 \text{ nm}$. We consider the case where a linearly polarized plane wave is incident towards the $+z$ direction whose angle of incidence is defined by θ .

To obtain a high transmissivity for the TM wave with a subsequent high ER, we determine the configuration parameters of dielectric gratings. Figures 2 and 3, respectively, show the transmissivity for the TM wave and the ER at $\lambda = 1.55 \mu\text{m}$ as a joint function of w and t_d . The angle of incidence is typically fixed to be $\theta = 0^\circ$. The ER is defined by

$$\text{ER} = 10 \log_{10} \frac{T_{\text{TM}}}{T_{\text{TE}}}, \quad (1)$$

where T_{TM} and T_{TE} are the transmissivities for the TM and TE waves, respectively. Calculation shows that the transmissivity reaches a maximum value of 94% with an ER of 20 dB

FIGURE 3: Extinction ratio observed at the output ($\lambda = 1.55 \mu\text{m}$).

for $w = 0.29 \mu\text{m}$ and $t_d = 0.22 \mu\text{m}$. We, therefore, adopt these configuration parameters in the following discussion.

The determined periodicity is consistent with the following relationship at normal incidence, that is, $\theta = 0^\circ$:

$$k_{\text{sp}} = k_0 \sin \theta \pm \frac{2\pi}{\Lambda}, \quad (2)$$

where k_0 is the free-space wavenumber; $\Lambda (=2w)$ is the periodicity; k_{sp} is the propagation constant of the SP mode, which can be obtained by the eigenmode analysis. Note that in the eigenmode analysis the refractive index of the dielectric grating is approximately modeled as a homogeneous layer with second-order effective index for the TM wave ($n_{\text{TM}}^{(2)}$), which is calculated by the effective medium theory [1]:

$$n_{\text{TM}}^{(2)} = \left[n_{\text{TM}}^2 + \frac{1}{3} \left\{ \pi \frac{\Lambda}{\lambda_0} f (1-f) \right\}^2 (n_{\text{H}}^{-2} - n_{\text{L}}^{-2})^2 n_{\text{TM}}^6 n_{\text{TE}}^2 \right]^{1/2}, \quad (3)$$

where λ_0 is the free-space wavelength, and f is the grating fill factor. n_{TE} and n_{TM} are the first-order effective indices for the TE and TM waves, which are, respectively, expressed as

$$\begin{aligned} n_{\text{TE}} &= [n_{\text{L}}^2 + f(n_{\text{H}}^2 - n_{\text{L}}^2)]^{1/2}, \\ n_{\text{TM}} &= [n_{\text{L}}^{-2} + f(n_{\text{H}}^{-2} - n_{\text{L}}^{-2})]^{-1/2}. \end{aligned} \quad (4)$$

3. Wavelength Characteristics

Figure 4 shows the reflectivity and transmissivity at normal incidence as a function of wavelength. For the TE wave, the reflectivity is close to unity over a wide range of wavelengths. The maximum transmissivity for the TM wave is calculated to be 94% at $\lambda = 1.55 \mu\text{m}$. The ratio of the transmitted field to the reflected field is less than -30 dB . This means that the nontransmitted power is almost absorbed in the metal film. It should be noted that the double-humped behavior is observed in the transmissivity. This behavior is caused by the fact that the structure supports asymmetric

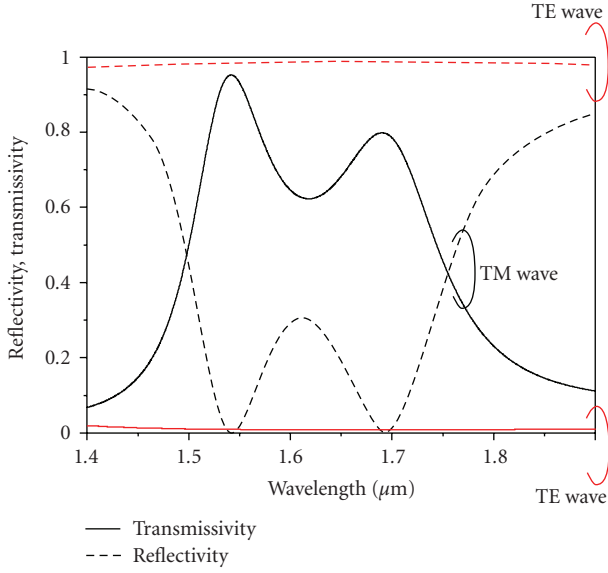


FIGURE 4: Wavelength characteristics at normal incidence ($\theta = 0^\circ$).

and symmetric modes, which, respectively, correspond to the first and second SP modes [12]. Figures 5(a) and 5(b) show the H_y -field distributions observed at $\lambda = 1.69 \mu\text{m}$ and $1.55 \mu\text{m}$, respectively. Only the fields observed in single cells are presented due to the periodicity. The high-index region is situated from $x = -0.145 \mu\text{m}$ to $x = 0.145 \mu\text{m}$. The field in Figure 5(a) exhibits the asymmetric distribution with respect to the middle plane of the metal film, while that in Figure 5(b) exhibits the symmetric distribution.

The ERs observed at the input and output sides are presented in Figure 6. The present polarizer maintains a high ER of more than 17 dB for the TM wave (at the output) over a wavelength range of $1.50 \mu\text{m}$ to $1.75 \mu\text{m}$. The maximum ER is calculated to be approximately 20 dB at $\lambda = 1.55 \mu\text{m}$. The ER for the TE wave (at the input) is more than 30 dB at $\lambda = 1.55 \mu\text{m}$.

We next study the case of oblique incidence, where θ is typically set to be 20° . Figures 7 and 8, respectively, show the transmissivity and the ER each as a function of wavelength. For reference, the data at normal incidence shown in Figures 4 and 6 are again plotted. The maximum transmissivity is obtained at $\lambda = 1.62 \mu\text{m}$, and then the triple-humped behavior is observed in this wavelength range. Figure 8 also shows that the region where the high ER is maintained shifts towards longer wavelengths. This behavior can be explained in terms of (2). At normal incidence, only the SP mode whose propagation constant is determined by $\pm 2\pi/\Lambda$ is excited, propagating in opposite directions along the metal-dielectric interface. However, when the angle of incidence is varied from $\theta = 0^\circ$, this symmetry is broken. In other words, (2) provides the following two relationships:

$$\begin{aligned} k_{\text{sp}}^+ &= k_0 \sin \theta + \frac{2\pi}{\Lambda}, \\ k_{\text{sp}}^- &= k_0 \sin \theta - \frac{2\pi}{\Lambda}. \end{aligned} \quad (5)$$

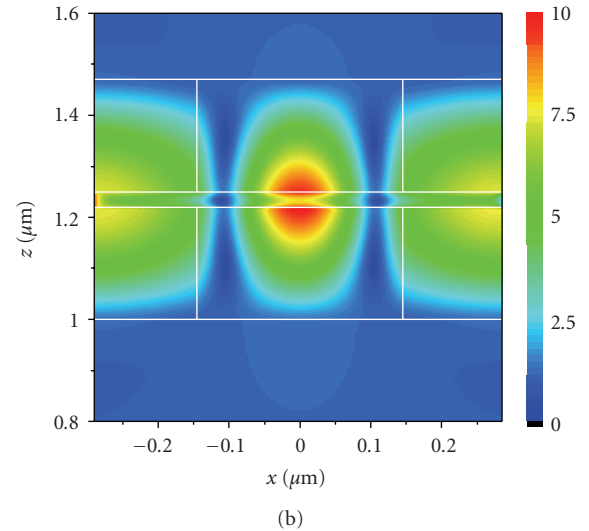
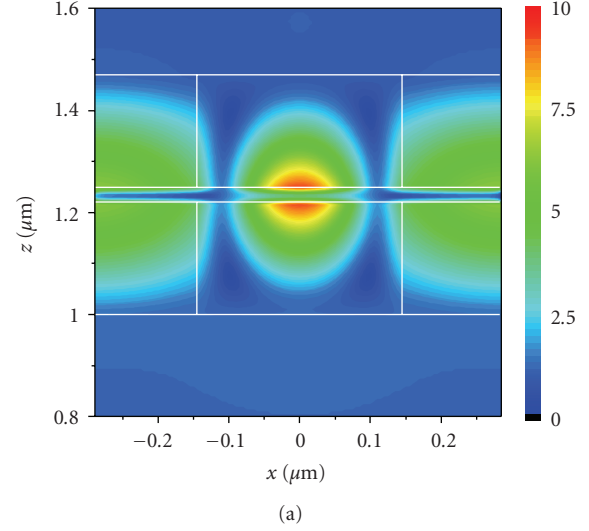


FIGURE 5: Field distributions at (a) $\lambda = 1.69 \mu\text{m}$ and (b) $\lambda = 1.55 \mu\text{m}$.

Therefore, the wavelength at which the SP mode is excited at normal incidence is separated into two wavelengths. In Figure 7, the first two modes are excited at $\lambda_{\text{sp}}^+ = 1.53 \mu\text{m}$ and $\lambda_{\text{sp}}^- = 1.79 \mu\text{m}$, which are separated from $\lambda_{\text{sp}} = 1.69 \mu\text{m}$ for $\theta = 0^\circ$. Only the second mode determined by k_{sp}^- can be seen at $\lambda_{\text{sp}}^- = 1.63 \mu\text{m}$ because the other one ($\lambda_{\text{sp}}^+ = 1.33 \mu\text{m}$) is beyond the scale. As a result, the triple-humped behavior of the transmissivity at oblique incidence is observed in this wavelength range.

4. Modified Structure

In the preceding section, we have studied the characteristics of the polarizer consisting of the metal film sandwiched between dielectric gratings. This polarizer requires that the structure be symmetric with respect to the metal film to excite the SP mode. It is, however, not easy to fabricate the symmetrical structure at a lightwave frequency, since a set of

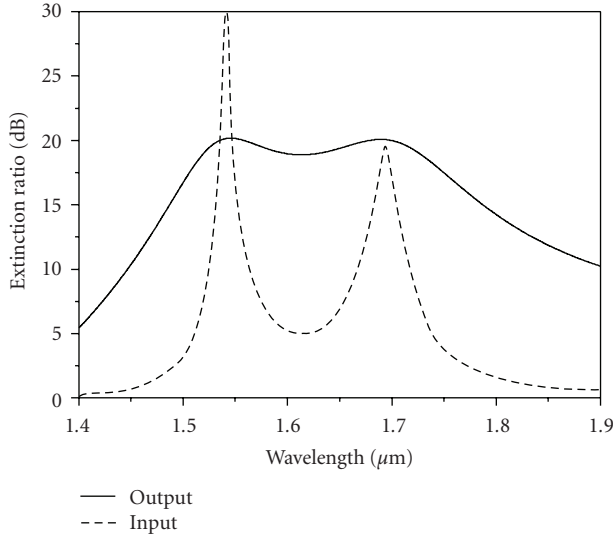
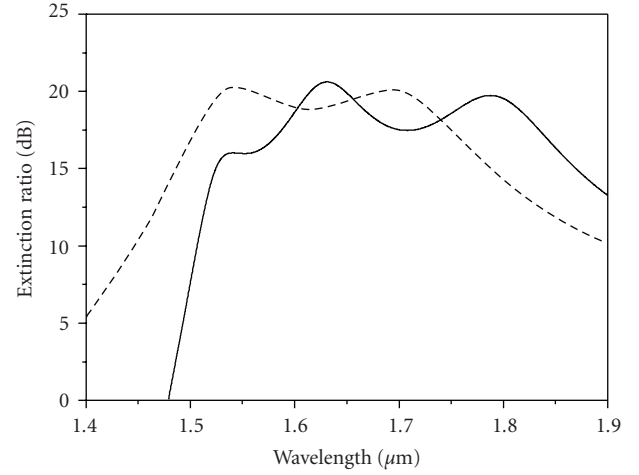
FIGURE 6: Extinction ratio at normal incidence ($\theta = 0^\circ$).

FIGURE 8: Extinction ratio as a function of wavelength.

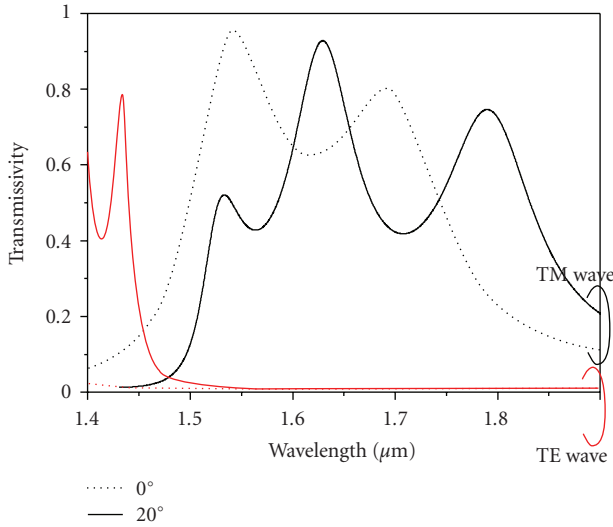


FIGURE 7: Transmissivity as a function of wavelength.

dielectric gratings must be placed precisely. In this section, we, therefore, investigate a more practical configuration.

We propose the configuration shown in Figure 9, in which a single dielectric grating is sandwiched between metal films. The refractive indices are the same as those treated in the previous section. It should be noted that the absorption loss is closely related to the thickness of the metal film. Since there exist the two metal films in the modified structure, we have decreased the metal thickness to sufficiently reduce the loss, so that t_m is taken to be $0.01 \mu\text{m}$. To achieve the TM-pass/TE-stop operation at $\lambda = 1.55 \mu\text{m}$, we have carried out some preliminary calculations similar to those shown in Figure 2 and finally chose $t_d = 0.44 \mu\text{m}$ and $w = w' = 0.25 \mu\text{m}$.

Figures 10 and 11 show the data corresponding to those shown in Figures 4 and 6, respectively. It was found that a transmissivity of more than 76% for the TM wave and a

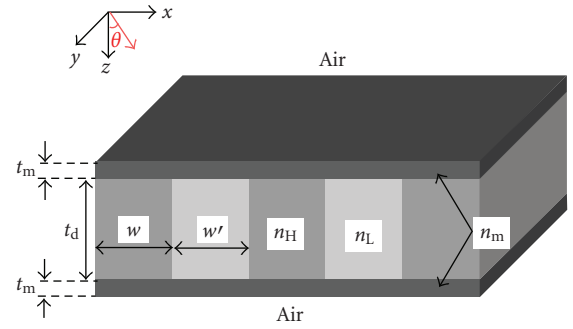


FIGURE 9: Configuration of a modified structure.

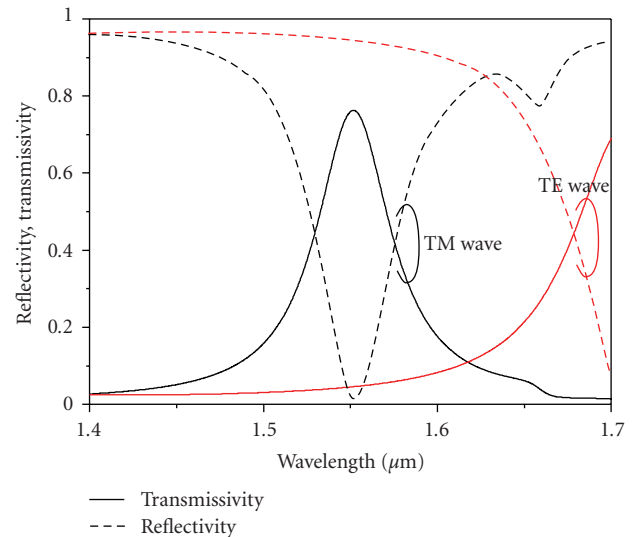


FIGURE 10: Wavelength characteristics.

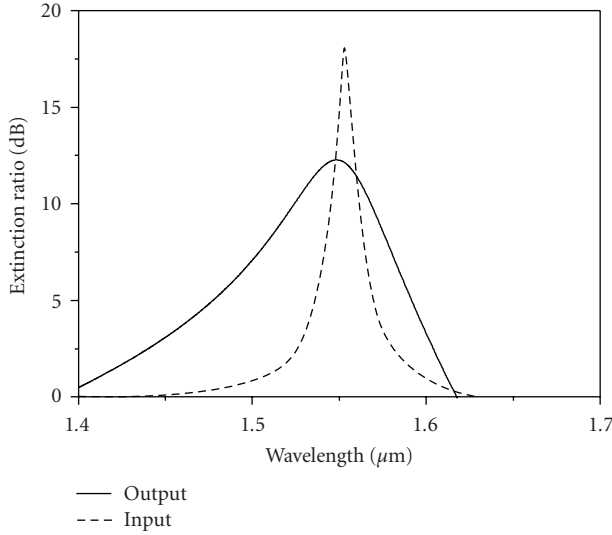
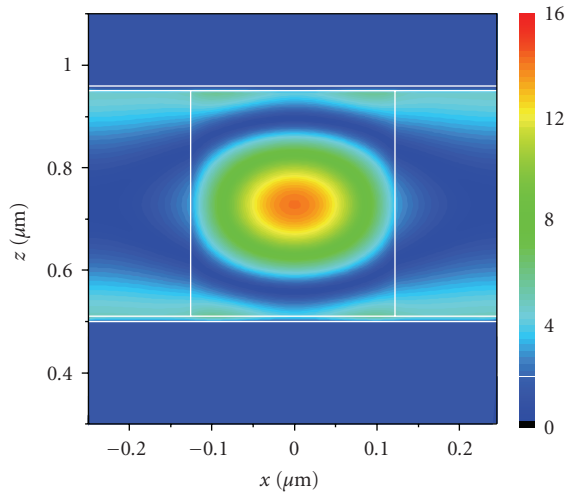


FIGURE 11: Extinction ratio as a function of wavelength.

FIGURE 12: Field distribution ($\lambda = 1.55 \mu\text{m}$).

reflectivity of more than 94% for the TE wave are obtained at $\lambda = 1.55 \mu\text{m}$, although the transmissivity is low compared with that obtained from the original structure discussed in Section 3. In contrast with the original structure, the enhanced transmission can be explained in terms of the Fabry-Pérot-like resonance in the cavity between the metal films [13]. The field distribution observed at $\lambda = 1.55 \mu\text{m}$ is illustrated in Figure 12, which clearly indicates a standing wave behavior in the high-index region. The ERs at the output and input sides are calculated to be 12 dB and 18 dB at $\lambda = 1.55 \mu\text{m}$, respectively.

5. Conclusion

A TM-pass/TE-stop polarizer using the surface plasmon resonance has been analyzed by the FDTD method. At normal incidence, calculation shows that a transmissivity of

more than 94% for the TM wave is obtained at $\lambda = 1.55 \mu\text{m}$. A high ER of more than 17 dB is observed over a wavelength range of $1.50 \mu\text{m}$ to $1.75 \mu\text{m}$. The high ER region is also maintained at oblique incidence, although the wavelength range shifts towards longer wavelengths.

Further consideration has been devoted to a more practical model in which a dielectric grating is sandwiched between metal films. The TM-pass/TE-stop operation is achieved at $\lambda = 1.55 \mu\text{m}$ with a transmissivity of more than 76%. The ER at the output side is calculated to be 12 dB.

Acknowledgments

The authors would like to thank Mr. Koji Sumida for his basic investigations of the present work. This paper was supported in part by MEXT, Grant-in-Aid for Scientific Research (c) (22560350).

References

- [1] R. Magnusson and D. Shin, "Diffractive optical components," in *Encyclopedia of Physical Science and Technology*, vol. 4, pp. 421–440, Academic Press, New York, NY, USA, 3rd edition, 2002.
- [2] V. M. Fitio and Y. V. Bobitski, "High transmission of system "dielectric grating thin metal film—dielectric grating,"" in *Proceedings of the 7th International Conference on Laser and Fiber-Optical Networks Modeling (LFNM '05)*, pp. 163–166, September 2005.
- [3] J. Yamauchi, K. Sumida, and H. Nakano, "A TMpass/ TE-stop polarizer consisting of a metal film sandwiched with dielectric gratings," in *Proceedings of the 10th International Symposium on Contemporary Photonics Technology*, vol. G-15, pp. 93–94, Tokyo, Japan, 2007.
- [4] J. Yamauchi, T. Yamazaki, K. Sumida, and H. Nakano, "TM/TE wave splitters using surface plasmon polaritons," in *Integrated Photonics and Nanophotonics Research and Applications*, Salt Lake City, Utah, USA, July 2007.
- [5] J. M. Steele, C. E. Moran, A. Lee, C. M. Aguirre, and N. J. Halas, "Metallodielectric gratings with subwavelength slots: optical properties," *Physical Review B*, vol. 68, no. 20, Article ID 205103, 7 pages, 2003.
- [6] T. Nikolajsen, K. Leosson, and S. I. Bozhevolnyi, "Surface plasmon polariton based modulators and switches operating at telecom wavelengths," *Applied Physics Letters*, vol. 85, no. 24, pp. 5833–5835, 2004.
- [7] K.-Y. Jung, F. L. Teixeira, and R. M. Reano, "Au/SiO₂ nanoring plasmon waveguides at optical communication band," *Journal of Lightwave Technology*, vol. 25, no. 9, pp. 2757–2765, 2007.
- [8] J.-W. Mu and W.-P. Huang, "A low-loss surface plasmonic Bragg grating," *Journal of Lightwave Technology*, vol. 27, no. 4, pp. 436–439, 2009.
- [9] P. B. Johnson and R. W. Christy, "Optical constants of the noble metals," *Physical Review B*, vol. 6, no. 12, pp. 4370–4379, 1972.
- [10] A. Taflove and S. Hagness, *Computational Electrodynamics: The Finite-Difference Time-Domain Method*, Artech House, Norwood, Mass, USA, 2000.
- [11] D. F. Kelley and R. I. Luebbers, "Piecewise linear recursive convolution for dispersive media using FDTD," *IEEE Transactions on Antennas and Propagation*, vol. 44, no. 6, pp. 792–797, 1996.

- [12] P. Berini, "Plasmon-polariton waves guided by thin lossy metal films of finite width: bound modes of symmetric structures," *Physical Review B*, vol. 61, no. 15, pp. 10484–10503, 2000.
- [13] E. Popov, S. Enoch, G. Tayeb, M. Nevière, B. Gralak, and N. Bonod, "Enhanced transmission due to nonplasmon resonances in one- and two-dimensional gratings," *Applied Optics*, vol. 43, no. 5, pp. 999–1008, 2004.

Research Article

Analysis of Plasmonic Waveguides and Gratings Using Implicit Finite-Difference Methods

Jun Shibayama, Junji Yamauchi, and Hisamatsu Nakano

Faculty of Engineering, Hosei University, 3-7-2 Kajino-cho Koganei, Tokyo 184-8584, Japan

Correspondence should be addressed to Jun Shibayama, shiba@hosei.ac.jp

Received 12 June 2010; Accepted 30 July 2010

Academic Editor: Ana Vukovic

Copyright © 2011 Jun Shibayama et al. This is an open access article distributed under the Creative Commons Attribution License, which permits unrestricted use, distribution, and reproduction in any medium, provided the original work is properly cited.

Various metal-insulator-metal- (MIM-) type plasmonic waveguides and gratings are investigated numerically. Three gratings are treated: one is formed by alternately stacking two kinds of MIM waveguides, another by periodic changes in the dielectric insulator materials of an MIM waveguide, and the other by a periodic variation of the air core width in an MIM waveguide. The dispersion property of each MIM waveguide of which the grating consists is analyzed using the implicit Yee-mesh-based beam-propagation method. It is shown that the third one has a relatively large effective index modulation of the guided mode with a simple grating structure, while maintaining a low propagation loss. Further examination is given to modifications of this grating structure. The transmission characteristics are examined using the frequency-dependent implicit locally one-dimensional FDTD method. We discuss how the modified grating structure affects the bandgap of the transmission characteristics.

1. Introduction

Recently, metal-insulator-metal- (MIM-) type plasmonic waveguides have received considerable attention, since compact optical circuits may be realized [1, 2]. The alternative effective index modulation of an MIM waveguide leads to a plasmonic waveguide Bragg grating that is one of the basic building blocks for small size plasmonic circuits. Three gratings have been mainly investigated: one is formed by alternately stacking two kinds of MIM waveguides (Figure 1(a)) [3], another by periodic changes in the dielectric insulator materials of an MIM waveguide (Figure 1(b)) [4], and the other by a periodic variation of the air core width in an MIM waveguide (Figure 1(c)) [5, 6]. We have numerically studied the sidelobe suppression of the latter one [7]. It is found that apodized and chirped gratings are quite effective in reducing the sidelobes. In addition, we have proposed a plasmonic microcavity offering a tunable resonance wavelength with varying an air core width. Note, however, that the characteristics of the above-mentioned three structures have not been compared in terms of an effective index modulation that is quite important to design gratings.

In this paper, we compare the basic characteristics of several MIM waveguides of which gratings are composed.

The effective index versus core width of each MIM waveguide is calculated using the imaginary-distance Yee-mesh-based beam-propagation method (YM-BPM) [8]. It is shown that the grating with a periodic variation of the air core width (Figure 1(c)) yields a relatively large effective index modulation of the guided mode in the grating section, while maintaining a low propagation loss. We next examine the transmission coefficient of several gratings, that is, concave and convex gratings are calculated using the frequency-dependent locally one-dimensional finite-difference time-domain method (LOD-FDTD) [7, 9]. It is found that the convex grating gives a wide bandgap in the transmission coefficient because of a large index modulation. In addition, a slight modification to the plasmonic grating is found to yield a large variation in the bandgap, which is not easily obtainable using conventional dielectric gratings.

This paper is organized as follows. Section 2 gives the dispersion model of a metal and the brief explanations of the numerical techniques based on the efficient implicit schemes. Section 3 discusses the dispersion properties of each MIM waveguide with respect to the core width. Section 4 investigates the transmission coefficient of several modified gratings. Section 5 provides the concluding remarks.

2. Numerical Methods

2.1. Dispersion Model. The metal dispersion treated here is expressed by the following Drude model [5–7]:

$$\epsilon_r(\omega) = \epsilon_\infty + \frac{\omega_D^2}{j\omega(\gamma_D + j\omega)}, \quad (1)$$

where ϵ_∞ is the dielectric constant of the material at infinite frequency, ω is the angular frequency, ω_D is the electron plasma frequency, and γ_D is the effective electron collision frequency.

2.2. Implicit Imaginary-Distance YM-BPM. The BPM is widely used to analyze optical waveguides. The BPM can also produce eigenmode fields quite efficiently, with the help of the imaginary-distance procedure. Note however that the conventional BPM cannot simultaneously offer all the electromagnetic fields, since it is based on the wave equation of either an electric or magnetic field. To simultaneously evaluate electric and magnetic field components, the YM-BPM has been developed on the basis of the explicit scheme [10]. The implicit scheme has also been introduced to the YM-BPM for efficient unconditionally stable calculations [8]. The use of Yee's mesh also means that the obtained eigenmode profile is readily used as an initial field in the following FDTD analysis. Detailed derivation of the three-dimensional YM-BPM can be found in [8], where the operator splitting is adopted in the propagation direction. Here, we present the resultant unsplit FD equations for the transverse magnetic (TM) waves suitable to the two-dimensional calculations as follows:

$$\begin{aligned} & \left(b_+^2 - a_-^2 \epsilon_{r,i+1/2} - \frac{b_+}{2} \delta_x^2 \right) E_{x,i+1/2}^{l+1} \\ &= \left(b_+ b_- - a_+ a_- \epsilon_{r,i+1/2} + \frac{b_+}{2} \delta_x^2 \right) E_{x,i+1/2}^l \\ & \quad - (a_+ b_+ - a_- b_-) H_{y,i+1/2}^l, \\ & H_{y,i+1/2}^{l+1} = \frac{1}{a_-} \left(a_+ H_{y,i+1/2}^l + b_+ E_{x,i+1/2}^{l+1} \right. \\ & \quad \left. - b_- E_{x,i+1/2}^l - \frac{1}{2} \delta_x^2 E_{x,i+1/2}^{l+1} - \frac{1}{2} \delta_x^2 E_{x,i+1/2}^l \right), \end{aligned} \quad (2)$$

where

$$\begin{aligned} a_\pm &= jk_0 \left(\frac{1}{\Delta z} \pm \frac{jk_0 n_0}{2} \right), \\ b_\pm &= 4jk_0 n_0 \pm \frac{k_0^2 n_0^2}{2}, \\ \delta_x^2 E_{x,i+1/2} &= \frac{c_1 E_{x,i-1/2} - c_2 E_{x,i+1/2} + c_3 E_{x,i+3/2}}{\Delta x^2} \end{aligned} \quad (4)$$

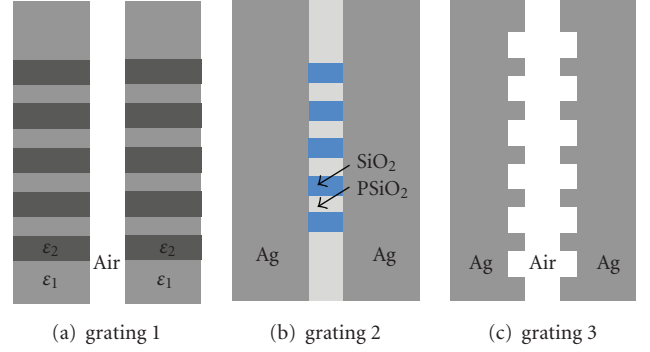


FIGURE 1: Configurations of plasmonic gratings. (a) grating 1: formed by alternately stacking two kinds of MIM waveguides, (b) grating 2: formed by periodic changes in the dielectric insulator materials of an MIM waveguide, and (c) grating 3: formed by a periodic variation of the air core width in an MIM waveguide.

in which

$$\begin{aligned} c_1 &= \frac{\epsilon_{r,i-1/2}}{\epsilon_{r,i}}, \\ c_2 &= \frac{\epsilon_{r,i+1/2}}{\epsilon_{r,i}} + \frac{\epsilon_{r,i+1/2}}{\epsilon_{r,i+1}}, \\ c_3 &= \frac{\epsilon_{r,i+3/2}}{\epsilon_{r,i+1}}. \end{aligned} \quad (5)$$

In the above equations, k_0 , n_0 , and ϵ_r , respectively, represent the free-space wavenumber, the reference refractive index, and the relative permittivity that is determined with (1) at a specific ω . As is observed, (2) gives a tridiagonal system of linear equations that are efficiently solved by the Thomas algorithm. Once E_x^{l+1} is obtained, H_y^{l+1} is explicitly calculated by (3).

To perform the eigenmode analysis, we apply the imaginary-distance procedure to the above YM-BPM [8], where the real propagation axis z is changed into the imaginary axis $j\tau$. This means that the phase variation of the propagating field turns into the amplification of the eigenmode field. The effective index gradually converges using the technique for renewing the reference refractive index n_0 .

2.3. Frequency-Dependent Implicit LOD-FDTD Method. For the time-domain analysis of a metal in optical wavelengths, we have to utilize the frequency-dependent FDTD [11]. Note that the spatial sampling widths should be quite small for the analysis of a surface plasmon wave localized around the metal-dielectric interface. This gives rise to a small time step due to the Courant-Friedrich-Levy (CFL) condition of the traditional explicit FDTD, resulting in long computational time. To efficiently perform the time-domain analysis, we have developed the frequency-dependent implicit LOD-FDTD [12, 13] that is free from the CFL condition [14]. In addition, to simply take into account the convolution integral, we have adopted the trapezoidal recursive convolution (TRC) technique requiring a single convolution [15, 16], which leads to almost the same accuracy as the piecewise

linear RC (PLRC) counterpart requiring two convolution integrals [17]. We here present the basic equation (TM waves) of the frequency-dependent LOD-FDTD based on the TRC technique for the Drude model as follows [7, 9]:

$$E'_x = E_x^n, \quad (6a)$$

$$E'_z = \frac{\epsilon_\infty - \chi_D^0/2}{\epsilon_\infty + \chi_D^0/2} E_z^n + \frac{1}{\epsilon_\infty + \chi_D^0/2} \phi_z^n + \frac{c\Delta t}{2(\epsilon_\infty + \chi_D^0/2)} \left(\frac{\partial H'_y}{\partial x} + \frac{\partial H_y^n}{\partial x} \right), \quad (6b)$$

$$\frac{H'_y - H_y^n}{\Delta t/2} = c \left(\frac{\partial E'_z}{\partial x} + \frac{\partial E_z^n}{\partial x} \right), \quad (6c)$$

for the first step and

$$E_z^{n+1} = E'_z, \quad (7a)$$

$$E_x^{n+1} = \frac{\epsilon_\infty - \chi_D^0/2}{\epsilon_\infty + \chi_D^0/2} E'_x + \frac{1}{\epsilon_\infty + \chi_D^0/2} \phi_x^n - \frac{c\Delta t}{2(\epsilon_\infty + \chi_D^0/2)} \left(\frac{\partial H_y^{n+1}}{\partial z} + \frac{\partial H'_y}{\partial z} \right), \quad (7b)$$

$$\frac{H_y^{n+1} - H'_y}{\Delta t/2} = -c \left(\frac{\partial E_x^{n+1}}{\partial z} + \frac{\partial E'_x}{\partial z} \right), \quad (7c)$$

for the second step, where E' and H' represent the intermediate fields, and c is the speed of light in a vacuum. The parameters used above are expressed as follows:

$$\begin{aligned} \phi_\delta^n &= \frac{E_\delta^n + E_\delta^{n-1}}{2} \Delta \chi_D^0 + e^{-\nu_D \Delta t} \phi_\delta^{n-1}, \\ \chi_D^0 &= \frac{\omega_D^2}{\nu_D} \left\{ \Delta t - \frac{1}{\nu_D} (1 - e^{-\nu_D \Delta t}) \right\}, \\ \Delta \chi_D^0 &= -\frac{\omega_D^2}{\nu_D^2} (1 - e^{-\nu_D \Delta t})^2 \end{aligned} \quad (8)$$

in which $\delta = x$ or z . Note that the normalized expression of field components is used. The equations for the TRC-LOD-FDTD are simpler than those for the PLRC-LOD-FDTD [13]. In the first step, we substitute (6c) into (6b) and implicitly solve the resultant equation using the Thomas algorithm. Then, (6c) is explicitly solved. In the second step, the equations are calculated in the same way as in the first step. It should be noted that the frequency-dependent implementation of the LOD-FDTD is much simpler than that of the frequency-dependent alternating-direction implicit (ADI) FDTD.

3. Dispersion Properties of MIM Waveguides

It is important to calculate the effective indexes of waveguides of which the grating is composed, since the alternative

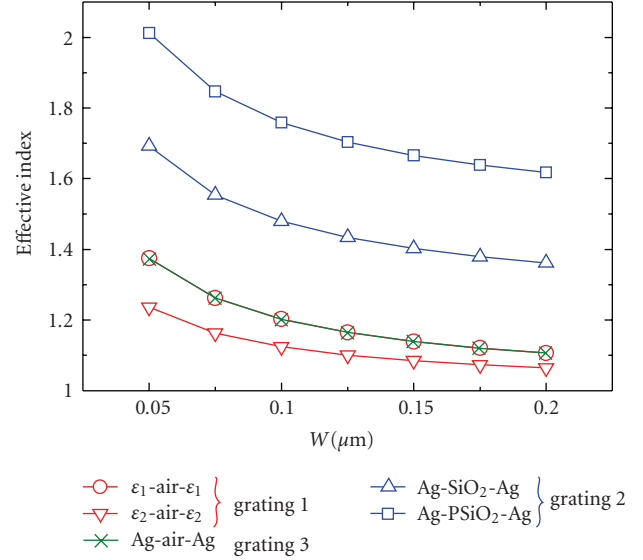


FIGURE 2: Effective index of the MIM waveguide.

effective index modulation predominates grating characteristics. Therefore, we first calculate the dispersion property of various MIM waveguides with respect to the core width. To obtain the effective index, we use the YM-BPM with the imaginary-distance procedure.

Three plasmonic gratings treated here are as follows (see Figure 1): one is formed by alternately stacking two kinds of MIM waveguides (grating 1) [3], another by periodic changes in the dielectric insulator materials of an MIM waveguide (grating 2) [4], and the other by a periodic variation of the dielectric insulator width in an MIM waveguide (grating 3) [5, 6]. For grating 1, $\omega_D = 15$ eV and $\nu_D = 0.01$ eV are used for ϵ_1 , and $\omega_D = 9$ eV and $\nu_D = 0.001$ eV are for ϵ_2 , where $\epsilon_\infty = 1$ is commonly adopted (metals are not specified) [3]. For grating 2, the permittivity of Ag is determined with $\epsilon_\infty = 3.7$, $\omega_D = 9.1$ eV, and $\nu_D = 0.018$ eV (in consistent with the experimental results), and those of SiO₂ and PSiO₂ are 1.46² and 1.23², respectively [4]. For grating 3, the Ag permittivity is the same as that used for grating 2.

Figure 2 shows the effective index of the MIM waveguide of which each grating is composed, as a function of core width W at a wavelength of $\lambda = 1.55 \mu\text{m}$. In Figure 2, the results of ϵ_1 -air- ϵ_1 and ϵ_2 -air- ϵ_2 are presented for grating 1, those of Ag-SiO₂-Ag and Ag-PSiO₂-Ag are for grating 2, and the result of Ag-air-Ag is for grating 3. It is interesting to note that the effective index becomes large as the core width W is decreased. This contrasts to the case of a conventional dielectric waveguide, where the effective index becomes small as the core width is decreased.

Now, we pay attention to the effective index difference Δn_e , when the two MIM waveguides are used to form gratings. For grating 1, Δn_e is calculated to be 0.138 at $W = 0.05 \mu\text{m}$ and 0.078 at $W = 0.1 \mu\text{m}$ from the results in Figure 2. For grating 2, Δn_e is to be 0.329 at $W = 0.05 \mu\text{m}$ and 0.278 at $W = 0.1 \mu\text{m}$. For grating 3, Δn_e is evaluated

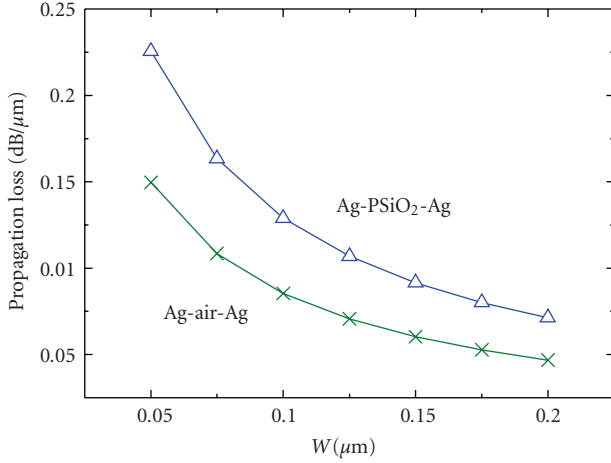


FIGURE 3: Propagation loss.

to be 0.172 with a combination of $W_1 = 0.05 \mu\text{m}$ and $W_2 = 0.1 \mu\text{m}$. As a result, a large Δn_e can be obtained for grating 2, although three materials (Ag, SiO_2 , and PSiO_2) are required. In contrast, for grating 3, a relatively large Δn_e is obtainable with a simple grating structure (Ag-air-Ag). The propagation losses for the latter two cases are calculated in Figure 3. It is seen that the propagation loss for Ag-air-Ag is smaller than that for Ag- PSiO_2 -Ag. Therefore, we choose the Ag-air-Ag waveguide (grating 3) because of a relatively large Δn_e and a low propagation loss, and investigate various modified gratings in the following analysis.

4. Characteristics of Modified Plasmonic Gratings

Using the frequency-dependent LOD-FDTD, we investigate four plasmonic gratings consisting of the Ag-air-Ag MIM waveguide with the input core width W_1 being fixed. The reference grating (concave type) is shown in Figure 4(a), the parameters of which are $W_1 = 0.1 \mu\text{m}$, $W_2 = 0.15 \mu\text{m}$, $L_p = 0.660 \mu\text{m}$, and $L_s = 0.292 \mu\text{m}$. The number of the grating period is 14. The normalized transmission coefficient for concave type is presented in Figure 5(a), which is indicated by the black solid line. Note that the Bragg condition is expressed by $k[n_{e1}(L_p - L_s) + n_{e2}L_s] = (2m + 1)\pi$. For this grating, the effective indexes are found to be $n_{e1} = 1.20204$ and $n_{e2} = 1.139$ in Figure 2. Then, the Bragg wavelength is calculated to be $\approx 1.55 \mu\text{m}$ from the above condition, which almost agrees with the center wavelength of the transmission coefficient for concave type.

Next, we examine another grating with $W_3 = 0.05 \mu\text{m}$ shown in Figure 4(b) (convex type). For this grating, the effective index for W_3 is $n_{e3} = 1.37428$, leading to a Bragg wavelength of $\approx 1.69 \mu\text{m}$ (recall that the effective index for the MIM waveguide becomes large, as the core width is reduced). The red solid line in Figure 5(a) represents the coefficient for convex type, in which the bandgap is found to be much wider than that for concave type. This is due to the fact that the bandgap becomes wide as the contrast between the effective

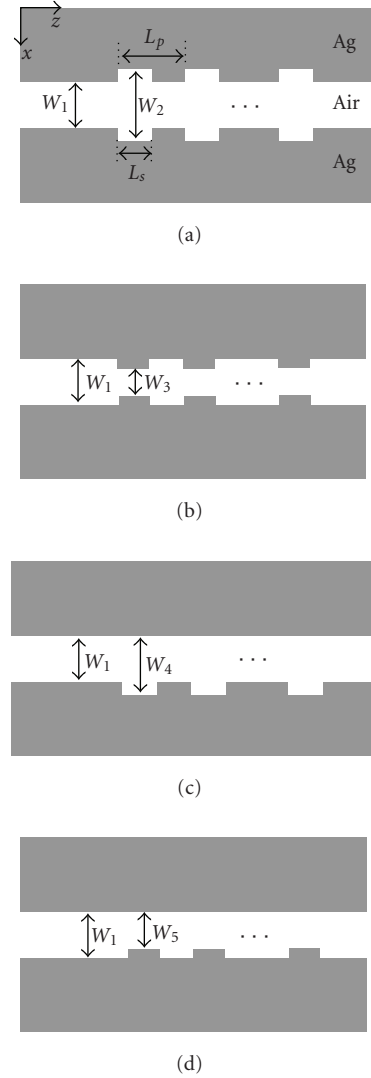
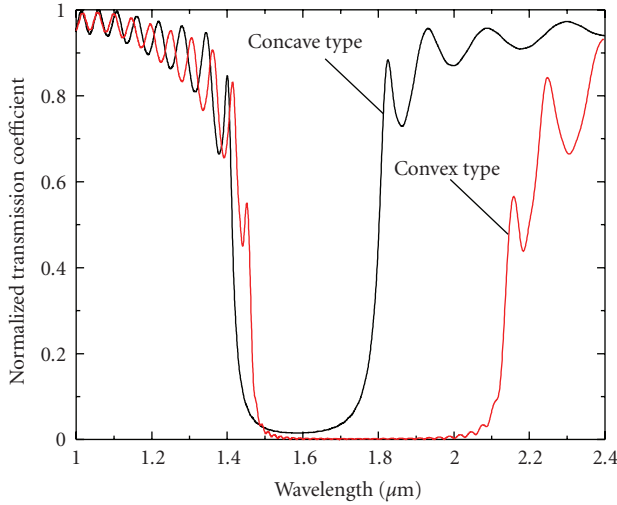


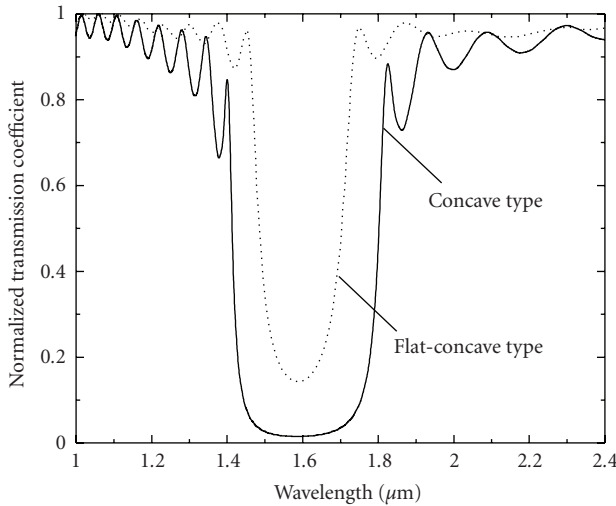
FIGURE 4: Various plasmonic gratings. (a) concave type, (b) convex type, (c) flat-concave type, and (d) flat-convex type.

indexes of alternating layers is increased [4]. In this case, the index contrast for convex type is 0.172, while that for concave type is 0.063, leading to the wide bandgap for convex type. As a result, the convex type plasmonic grating can yield a wide bandgap, compared with the concave type where a large effective index modulation cannot be obtained for a large W as shown in Figure 2.

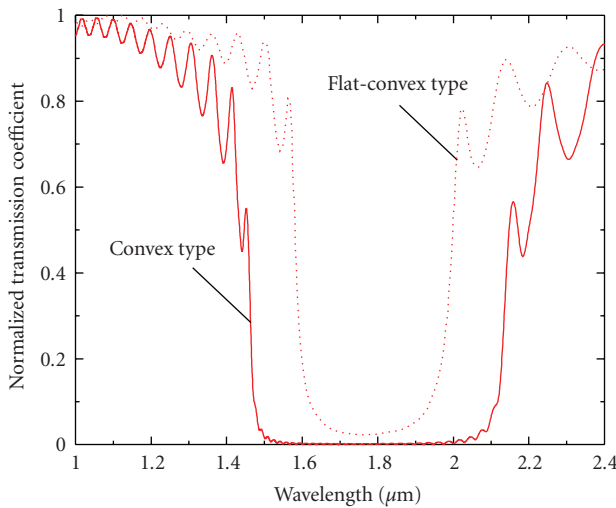
We further modify the gratings, in which the one side of the metals for concave type is replaced with a flat metal, as shown in Figure 4(c) (flat-concave type). For this type, the effective index of the $W_4 (= 0.125 \mu\text{m})$ section is 1.165, resulting in a Bragg wavelength of ≈ 1.56 . This Bragg wavelength is close to that without the modification (≈ 1.55 for concave type). It is therefore expected that the bandgap of the transmission coefficient for flat-concave type is reduced with the Bragg wavelength being almost fixed. The black dotted line in Figure 5(b) is the coefficient for flat-concave type. As expected, the bandgap becomes narrower than that



(a) Comparison between concave type (Figure 4(a)) and convex type (Figure 4(b))



(b) Comparison between concave type (Figure 4(a)) and flat-concave type (Figure 4(c))



(c) Comparison between convex type (Figure 4(b)) and flat-convex type (Figure 4(d))

FIGURE 5: Normalized transmission coefficient.

for concave type, while maintaining the Bragg wavelength. This is almost true for flat-convex type (the one side of the metals for convex type is taken flat as shown in Figure 4(d)), in which the coefficient is approximately centered in that for convex type (see Figure 5(c)). It should be noted that even the slight modification to the plasmonic grating structure shown above leads to a large variation in the bandgap, which is not easily obtainable from conventional dielectric gratings.

Finally, we point out the efficiency of the LOD-FDTD. In the above analysis, we have used a time step of 0.102 fs ten times as large as that determined from the CFL condition of the explicit FDTD. As a result, the computational time of the LOD-FDTD is successfully reduced to 30% of the explicit counterpart, where a PC with Core2Quad processor (2.66 GHz) is used. The LOD-FDTD is suitable for the analysis of plasmonic devices in which quite small sampling widths should be required.

5. Conclusion

We have investigated the dispersion characteristics of several MIM waveguides and examined the transmission coefficient of several modified gratings. First, we briefly present the numerical techniques, that is, the implicit YM-BPM for the eigenmode analysis and the frequency-dependent LOD-FDTD for the time-domain analysis. Next, we calculate the effective index of each MIM waveguide. A simple MIM waveguide made of Ag-air-Ag is found to provide a relatively large effective index modulation, maintaining a low propagation loss. We further calculate the characteristics of concave and convex gratings. The convex grating is shown to yield a wide bandgap of the transmission coefficient. Finally, we modify the grating structures to study the effect on the transmission coefficient. A slight modification to the grating leads to a significant change in the transmission coefficient. Applications to three-dimensional gratings are now under consideration.

Acknowledgments

The authors would like to thank Mr. Ryo Takahashi for calculating the characteristics of plasmonic waveguides and gratings. This work was supported in part by MEXT, Grant-in-Aid for Young Scientists (B) (21760266).

References

- [1] K. Tanaka and M. Tanaka, "Simulations of nanometric optical circuits based on surface plasmon polariton gap waveguide," *Applied Physics Letters*, vol. 82, no. 8, pp. 1158–1160, 2003.
- [2] J. Takahara and F. Kusunoki, "Guiding and nanofocusing of two-dimensional optical beam for nano-optical integrated circuits," *IEICE Transactions on Electronics*, vol. E90-C, no. 1, pp. 87–94, 2007.
- [3] B. Wang and G. P. Wang, "Plasmon Bragg reflectors and nanocavities on flat metallic surfaces," *Applied Physics Letters*, vol. 87, no. 1, Article ID 013107, 3 pages, 2005.

- [4] A. Hosseini and Y. Massoud, "A low-loss metal-insulator-metal plasmonic bragg reflector," *Optics Express*, vol. 14, no. 23, pp. 11318–11323, 2006.
- [5] Z. Han, E. Forsberg, and S. He, "Surface plasmon Bragg gratings formed in metal-insulator-metal waveguides," *IEEE Photonics Technology Letters*, vol. 19, no. 2, pp. 91–93, 2007.
- [6] L. Yuan and Y. Y. Lu, "A recursive-doubling Dirichlet-to-Neumann-map method for periodic waveguides," *Journal of Lightwave Technology*, vol. 25, no. 11, pp. 3649–3656, 2007.
- [7] J. Shibayama, A. Nomura, R. Ando, J. Yamauchi, and H. Nakano, "A frequency-dependent LOD-FDTD method and its application to the analyses of plasmonic waveguide devices," *IEEE Journal of Quantum Electronics*, vol. 46, no. 1, pp. 40–49, 2010.
- [8] J. Yamauchi, T. Mugita, and H. Nakano, "Implicit Yee-mesh-based finite-difference full-vectorial beam-propagation method," *Journal of Lightwave Technology*, vol. 23, no. 5, pp. 1947–1955, 2005.
- [9] J. Shibayama, R. Ando, A. Nomura, J. Yamauchi, and H. Nakano, "Simple trapezoidal recursive convolution technique for the frequency-dependent FDTD analysis of a drude-lorentz model," *IEEE Photonics Technology Letters*, vol. 21, no. 2, pp. 100–102, 2009.
- [10] S. M. Lee, "Finite-difference vectorial-beam-propagation method using Yee's discretization scheme for modal fields," *Journal of the Optical Society of America A*, vol. 13, no. 7, pp. 1369–1377, 1996.
- [11] A. Taflov and S. C. Hagness, *Computational Electrodynamics: The Finite-Difference Time-Domain Method*, Artech House, Norwood, Mass, USA, 3rd edition, 2005.
- [12] J. Shibayama, R. Takahashi, J. Yamauchi, and H. Nakano, "Frequency-dependent LOD-FDTD implementations for dispersive media," *Electronics Letters*, vol. 42, no. 19, pp. 1084–1086, 2006.
- [13] J. Shibayama, R. Takahashi, J. Yamauchi, and H. Nakano, "Frequency-dependent locally one-dimensional FDTD implementation with a combined dispersion model for the analysis of surface plasmon waveguides," *IEEE Photonics Technology Letters*, vol. 20, no. 10, pp. 824–826, 2008.
- [14] J. Shibayama, M. Muraki, J. Yamauchi, and H. Nakano, "Efficient implicit FDTD algorithm based on locally one-dimensional scheme," *Electronics Letters*, vol. 41, no. 19, pp. 1046–1047, 2005.
- [15] R. Siushansian and J. LoVetri, "Comparison of numerical techniques for modeling electromagnetic dispersive media," *IEEE Microwave and Guided Wave Letters*, vol. 5, no. 12, pp. 426–428, 1995.
- [16] R. Siushansian and J. LoVetri, "Efficient evaluation of convolution integrals arising in FDTD formulations of electromagnetic dispersive media," *Journal of Electromagnetic Waves and Applications*, vol. 11, no. 1, pp. 101–117, 1997.
- [17] D. F. Kelley and R. I. Luebbers, "Piecewise linear recursive convolution for dispersive media using FDTD," *IEEE Transactions on Antennas and Propagation*, vol. 44, no. 6, pp. 792–797, 1996.

Research Article

Oblique Du-Fort Frankel Beam Propagation Method

Ken Chan, Philip Sewell, Ana Vukovic, and Trevor Benson

The George Green Institute for Electromagnetic Research, University of Nottingham, Nottingham NG7 2RD, UK

Correspondence should be addressed to Ken Chan, eexkc1@nottingham.ac.uk

Received 15 May 2010; Accepted 24 July 2010

Academic Editor: Jun Shibayama

Copyright © 2011 Ken Chan et al. This is an open access article distributed under the Creative Commons Attribution License, which permits unrestricted use, distribution, and reproduction in any medium, provided the original work is properly cited.

The oblique BPM based on the Du-Fort Frankel method is presented. The paper demonstrates the accuracy and the computational improvements of the scheme compared to the oblique BPM based on Crank-Nicholson (CN) scheme.

1. Introduction

Increasingly complex optical devices demand computationally fast and memory efficient algorithms for modelling purposes. Finite difference beam propagation method (FD-BPM) is a popular numerical technique for simulating large network of optical components due to its computational advantages over classical numerical techniques such as Finite Difference Time Domain (FDTD) method. The BPM method is commonly applied in the Cartesian coordinate system. However when the boundaries of an optical component are not aligned to the Cartesian mesh, for example in the case of tilted waveguides, bends and Mach-Zehnder modulators, sampling on the Cartesian mesh introduces nonphysical staircasing noise. The noise can be minimised by using very fine mesh but that in return incurs large computational costs. To more efficiently reduce the sampling error an improved three-point formulas are used at the interface which take into account the distance between the boundary and the transverse sampling points [1–3]. Further increase in accuracy of the Cartesian BPM, particularly for strongly guided waveguides, is achieved by considering the longitudinal component of magnetic field which is commonly neglected in the standard FD-BPM method [4]. In contrast to Cartesian system, Oblique and Structure Related (SR) coordinate system offers an accurate and efficient alternative for modelling nonorthogonal structures and automatically satisfies $\partial n / \partial z = 0$. The sampling grid of the SR mesh is aligned with the component material boundary thus eliminating staircase error and allowing relaxation in mesh size. Various SR-BPM schemes have been

introduced [5–11] and different schemes can be combined together to map out the optical component. Furthermore, the SR coordinate system ensures high accuracy for the simple paraxial BPM formulation even without the use of wide-angled schemes [10]. The oblique equation takes into account the propagation direction, which is usually parallel to the structure boundary. Hence the mode-mismatch error is small. One of the motivations for implementation in oblique coordinates is to remove the need for high-order wide-angle scheme which requires substantial computational resources. Wide-angle for oblique coordinate has been developed by Sujecki [11]. However the author has also confirmed that the wide-angle oblique approach should in principle only be applied to low refractive index contrast structures [12].

So far SR and oblique BPM schemes have been implemented using implicit scheme such as CN. Whilst for the two-dimensional (2D) structures this is computationally fast, in the case of modelling three-dimensional (3D) structures the CN scheme uses iterative matrix solvers such as BI-CGSTAB or GMRES [13] and thus requires huge computational resources. More computationally efficient Alternate Direction Iterative (ADI) schemes [14] cannot be implemented in SR coordinates due to mixed derivatives in transverse directions and are limited to Cartesian meshes. Alternatively, Du-Fort Frankel (DFF) schemes provide larger step size and better stability condition than simple explicit schemes and can be implemented on a parallel computational platform thus providing computational efficiency for modelling realistic 3D optical components. The downside of the DFF scheme is the inherent spurious or “ghost” mode

that can affect the accuracy and stability of the scheme and which can be alleviated by the right choice of parameters and initial fields [15, 16].

In this paper, the oblique BPM method is implemented using the DFF scheme. Section 2 outlines the formulation of the method and Section 3 presents the results for the power loss and computational efficiency of the scheme and compares it against the oblique CN BPM scheme. The results are presented for tilted 2D and 3D waveguides and scalar fields.

2. Formulation

A general approach for formulating oblique BPM is outlined in [5] and is limited to structures that do not vary with the propagation direction and the β reference is parallel to the propagating direction.

In this section an oblique BPM method based on the paraxial approximation and implemented in the DFF algorithm is outlined. Figure 1 shows schematic presentation of two coordinate systems u, y, z' , and x, y, z , where z and z' form an angle θ . It is assumed that the fields propagate with respect to the z' axis. The 3D oblique coordinate BPM equation adopted from [9] is used as

$$\left(\frac{\partial^2}{\partial x^2} + \frac{\partial^2}{\partial y^2} + \frac{\partial^2}{\partial z^2} + k^2(x, y, z) \right) \Psi = 0, \quad (1)$$

where Ψ represents the scalar field of the form

$$\Psi(u, z') = \varphi(u, z') \exp(-j\beta_0 z'). \quad (2)$$

The relationship between the oblique and the Cartesian coordinate systems is given as

$$\begin{aligned} x &= u + z' \sin \theta, \\ z &= z' \cos \theta. \end{aligned} \quad (3)$$

The difference equations are obtained using the chain rule as

$$\frac{\partial \Psi}{\partial u} = \frac{\partial \Psi}{\partial x}, \quad (4)$$

$$\frac{\partial \Psi}{\partial z'} = \frac{\partial \Psi}{\partial x} \sin \theta + \frac{\partial \Psi}{\partial z} \cos \theta, \quad (5)$$

$$\frac{\partial^2 \Psi}{\partial u^2} = \frac{\partial^2 \Psi}{\partial x^2}, \quad (6)$$

$$\frac{\partial^2 \Psi}{\partial u \partial z'} = \frac{\partial^2 \Psi}{\partial x^2} \sin \theta + \frac{\partial^2 \Psi}{\partial x \partial z} \cos \theta, \quad (7)$$

$$\frac{\partial^2 \Psi}{\partial z'^2} = \frac{\partial^2 \Psi}{\partial x^2} \sin^2 \theta + 2 \frac{\partial^2 \Psi}{\partial x \partial z} \sin \theta \cos \theta + \frac{\partial^2 \Psi}{\partial z^2} \cos^2 \theta. \quad (8)$$

Rearranging (6)–(8) and substituting into (1) results in the oblique wave equation:

$$\left(\frac{\partial^2 \Psi}{\partial z'^2} - 2 \frac{\partial^2 \Psi}{\partial u \partial z'} \sin \theta + \frac{\partial^2 \Psi}{\partial u^2} + \frac{\partial^2}{\partial y^2} \right) + k^2 \cos \theta \Psi = 0. \quad (9)$$

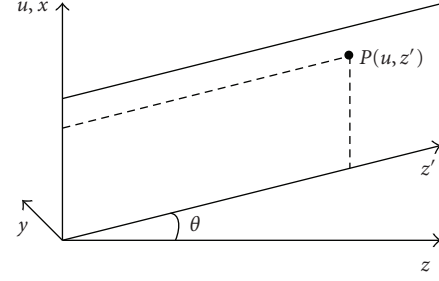


FIGURE 1: Oblique coordinate system.

Substituting the field from (2) into (9) gives the scalar oblique BPM equation as

$$\begin{aligned} 2j\beta_0 \frac{\partial \varphi}{\partial z'} + \sin \theta \frac{\partial^2 \varphi}{\partial u \partial z'} \\ = 2j\beta_0 \sin \theta \frac{\partial \varphi}{\partial u} + \frac{\partial^2 \varphi}{\partial u^2} + \frac{\partial^2}{\partial y^2} + (k^2 \cos \theta - \beta_0^2) \varphi. \end{aligned} \quad (10)$$

This equation can be straightforwardly implemented using the CN scheme. In the case of the 2D modelling where the $\partial^2 / \partial^2 y = 0$, CN scheme requires tridiagonal matrix solver known as Thomas algorithm is used to solve (10) which is much faster than the sparse matrix solver. However in the 3D modelling, term $\partial^2 / \partial^2 y$ in (10) introduces two additional unknown field points in each calculation step thus resulting in five unknown field points. In CN scheme this requires sparse matrix solver such as the commonly used BI-CGSTAB iterative solver [17].

In order to implement DFF scheme the local field point $\varphi_{l,m,n}$ and the transverse second derivatives are discretized as

$$\begin{aligned} \varphi_{l,m,n} &\approx \frac{\varphi_{l+1,m,n} + \varphi_{l-1,m,n}}{2}, \\ \frac{\partial^2 \varphi_{l,m,n}}{\partial u^2} &\approx \frac{\varphi_{l,m+1,n} + \varphi_{l,m-1,n} - (\varphi_{l+1,m,n} + \varphi_{l-1,m,n})}{\Delta u^2}, \end{aligned} \quad (11)$$

where l, m , and n are the discretised position in the z' , u , and y direction. Substituting the DFF scheme into (10), the numerical implementation for oblique DFF BPM is as follows:

$$\begin{aligned} \frac{L}{2} \left(\frac{\varphi_{l+1,m,n} - \varphi_{l-1,m,n}}{\Delta z'} - \sin \theta \frac{\varphi_{l,m+1,n} - \varphi_{l,m-1,n}}{2\Delta u} \right) \\ + \sin \theta \left(\frac{\varphi_{l+1,m+1,n} - \varphi_{l-1,m+1,n}}{2\Delta u \Delta z'} \right. \\ \left. - \frac{\varphi_{l+1,m-1,n} + \varphi_{l-1,m-1,n}}{2\Delta u \Delta z'} \right) \\ = \varphi_{u''} + \varphi_{y''} + (k^2 - \beta_0^2) \frac{(\varphi_{l+1,m,n} + \varphi_{l-1,m,n})}{2}, \end{aligned} \quad (12)$$

where $L = 2j\beta_0$, and $\varphi_a'' = (\varphi_{m,a+1} + \varphi_{m,a-1} - \varphi_{m+1,a} - \varphi_{m-1,a}) / \Delta a^2$. The additional term in (10) diminishes the explicit nature of the DFF, the 3D oblique DFF scheme corresponds to separable tri-diagonal matrices on each layer of the 3D structure. This can be efficiently solved by

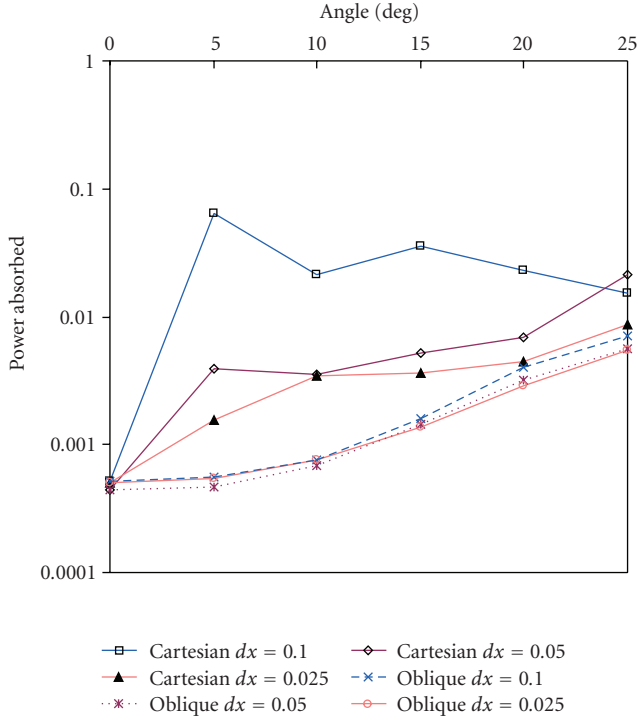


FIGURE 2: Power loss for a range of tilted angles for the oblique DFF-BPM and the Cartesian DFF-BPM method.

Thomas algorithm and is algorithmically efficient for parallel computing. Solving of the tri-diagonal matrix is more computationally efficient than solving the sparse matrix thus ensuring better computational efficiency of the 3D oblique DFF-BPM compared to the oblique CN-BPM.

3. Results

In this section the accuracy and computational stability of the oblique DFF-BPM method is analyzed and compared with the oblique CN-BPM method. Both 2D and 3D tilted waveguides are analyzed.

In an oblique coordinate system a tilted waveguide is essentially a straight waveguide and ideally the power transmitted in a tilted waveguide in the oblique system is identical to the power transmitted in a straight waveguide in the Cartesian mesh. Figure 2 compares power loss of the 2D tilted waveguide analyzed using the oblique DFF-BPM with that analyzed using the DFF scheme in Cartesian mesh for different tilted angles and different sampling meshes. Perfectly matched layer (PML) is used for absorbing any leakage from the simulation window. The implementation of PML for the DFF method is described in [16]. The PML layer is set as $1.0 \mu\text{m}$ and strength, σ/ω is set as 10. Guided mode at the wavelength of $1.15 \mu\text{m}$ is launched in the $1 \mu\text{m}$ wide slab waveguide with core refractive index $n = 1.1$ surrounded by air. Longitudinal sampling $\Delta z'$ is fixed at $0.1 \mu\text{m}$ and the waveguide length is $409.6 \mu\text{m}$. It can be seen that by reducing the sampling of the mesh the power loss in the Cartesian BPM is reduced whilst for the oblique DFF-BPM the change

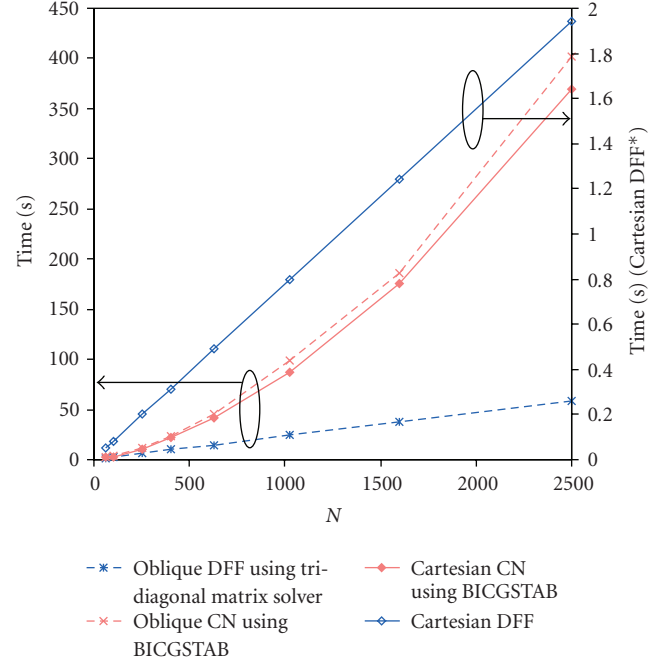


FIGURE 3: Comparison of the computational time for the oblique and Cartesian DFF-BPM and CN-BPM w.r.t. the total number of mesh points N .

of the mesh size does not significantly change the power loss. This indicates that the mesh size can be more relaxed in the case of the oblique DFF-BPM ensuring faster run time.

Figure 3 compares the computational runtime of the 3D oblique and Cartesian DFF- and CN-BPM methods for different number of total mesh points N . A simple $1 \mu\text{m}$ by $1 \mu\text{m}$ square metal-air waveguide is chosen for a fair speed test. Longitudinal step $\Delta z'$ is fixed at $0.05 \mu\text{m}$, $\Delta u = \Delta y$, and the waveguide is $100 \mu\text{m}$ long. For the oblique simulation, the same waveguide is used but tilted at an angle of 5° . Figure 3 shows that the Cartesian DFF excels in speed even without any parallelization involved. Figure 3 also shows that oblique DFF-BPM is substantially slower than Cartesian DFF-BPM due to the implementation of the Thomas algorithm. However, when compared with the Cartesian and oblique CN-BPM methods, the oblique DFF-BPM method is much faster, especially for large mesh sizes. However, it should be noted that DFF-BPM requires smaller longitudinal step size than CN-BPM to achieve the same level of accuracy and maintain stability. The 3D oblique DFF-BPM is also suitable for parallel computing platform allowing for more computationally efficient simulations.

Figure 4 analyses the stability of the oblique DFF-BPM method. It is well known that the main weakness of the DFF algorithm is the appearance of the spurious solution [15]. The position of the spurious mode can be controlled by appropriate choice of the mesh size and the excitation [16]. It is desirable that the spurious mode is not too close to the waveguide true mode so that the stability of the algorithm is not affected. Generally increasing the transverse

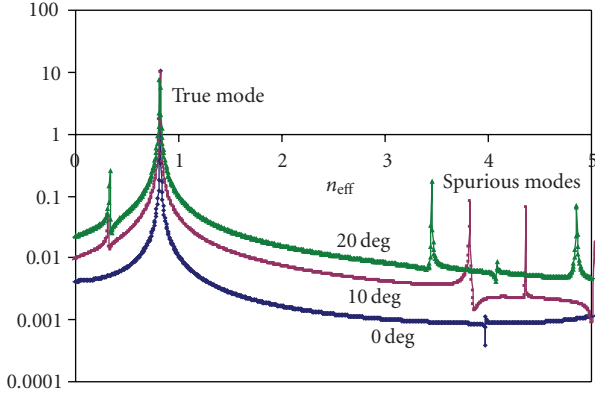


FIGURE 4: Fourier transform of field overlaps along the waveguide to identify the true mode ($n_{\text{eff}} = 0.82$) and the appearance of spurious modes at various tilted angles.

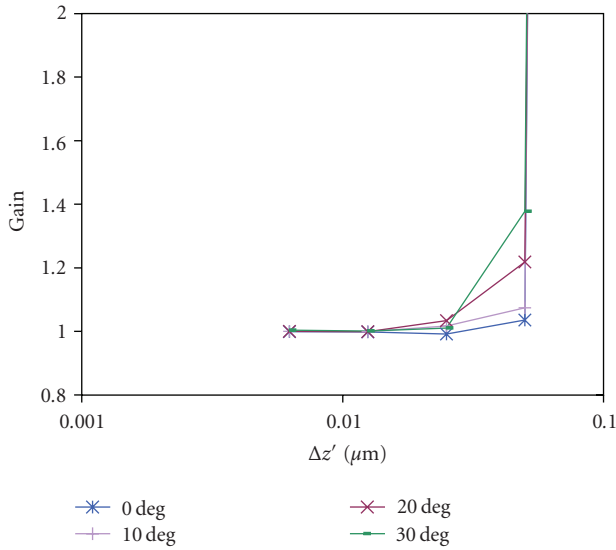


FIGURE 5: Power gain for oblique DFF. It shows the necessity for keeping the propagation step size small to maintain stability when transverse mesh size is small ($\Delta u = 0.01 \mu\text{m}$).

mesh size and reducing the propagation size step will place the spurious mode further away from the true mode [16]. Figure 4 investigates the impact of the tilted angle on the position of the spurious mode for a fixed mesh size. Figure 4 gives the Fourier transform of the field overlap between the incident field and the field evolved along the waveguide for different tilted angles. The 3D waveguide is a rectangular metal-air waveguide with dimensions of $1 \mu\text{m}$ by $0.5 \mu\text{m}$ and $204.8 \mu\text{m}$ long. Transverse mesh size is $\Delta u = \Delta y = 0.1 \mu\text{m}$ and longitudinal step sized is $\Delta z' = 0.05 \mu\text{m}$. Half sine wave of $1.15 \mu\text{m}$ wavelength is launched at the input. Figure 4 shows that the increase of the tilted angle brings the spurious and the true mode closer together. This will have implications on the maximum tilted angle that can be considered using the oblique DFF-BPM method.

The stability of oblique DFF is determined by the oblique angle and the mesh size. The effect of the mesh size is

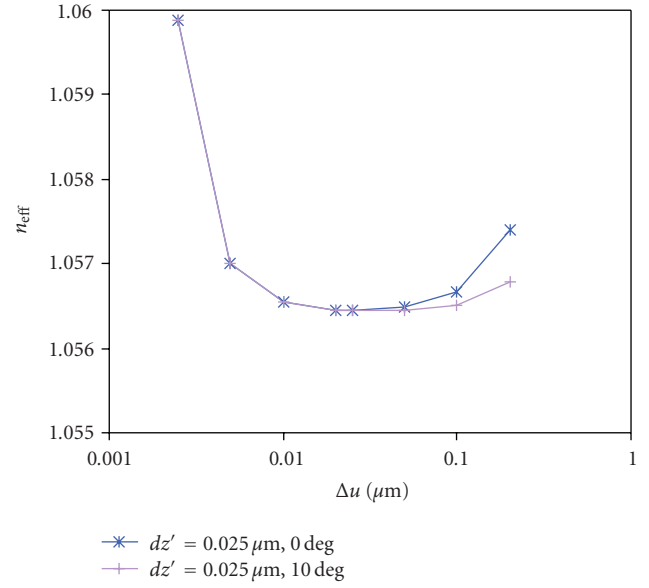


FIGURE 6: Effective index of a slab waveguide using Cartesian DFF and 10 degree tilted oblique DFF method. Accuracy deteriorates as it reaches the unstable region.

examined in Figure 5 for $\Delta u = 0.01 \mu\text{m}$ and different tilted angles. The waveguide parameters are as in Figure 2. It shows that for small transverse mesh size, it is necessary to keep the propagation step size small to maintain stability. It can be seen that when the oblique angle is small, the oblique DFF behaves similar to the Cartesian DFF. As the oblique angle increases, the oblique DFF requires smaller propagation step or larger transverse mesh size to maintain the stability.

Figure 6 examines the parameter choice and instability on the calculation of the effective index. The waveguide parameters are the same as in Figure 2. The obtained effective index is plotted for $\Delta z' = 0.025 \mu\text{m}$ with various mesh sizes and compared between the Cartesian DFF applied to the straight waveguides and the oblique DFF applied to the 10° tilted waveguide. Figure 6 shows the Cartesian DFF and the 10° tilted oblique DFF agree very well for small mesh sizes but have significant discrepancy when the transverse mesh size is increased. It can be concluded that the stability condition has restrained the use of very small transverse mesh size in DFF. However, using large transverse mesh size would risk losing accuracy. However, it should be noted that the difference in coordinate system makes it difficult to compare results directly. A slice in the oblique coordinate is equivalent to a diagonal cross-section through multiple slices on a Cartesian coordinate system.

Figures 7(a)–7(c) shows the field profiles of the 2D tilted waveguide obtained using the oblique and Cartesian DFF-BPM method. The slab waveguide is as in Figure 2 but $10 \mu\text{m}$ long and tilted by 10° . Figure 7(a) shows the field profile of the 10° tilted waveguide mapped in the Cartesian mesh and Figure 7(b) shows the same waveguide analysed using the oblique DFF-BPM method. It can be seen that the Cartesian mesh introduces large staircasing noise even for very fine sampling mesh. For comparison, the field profile

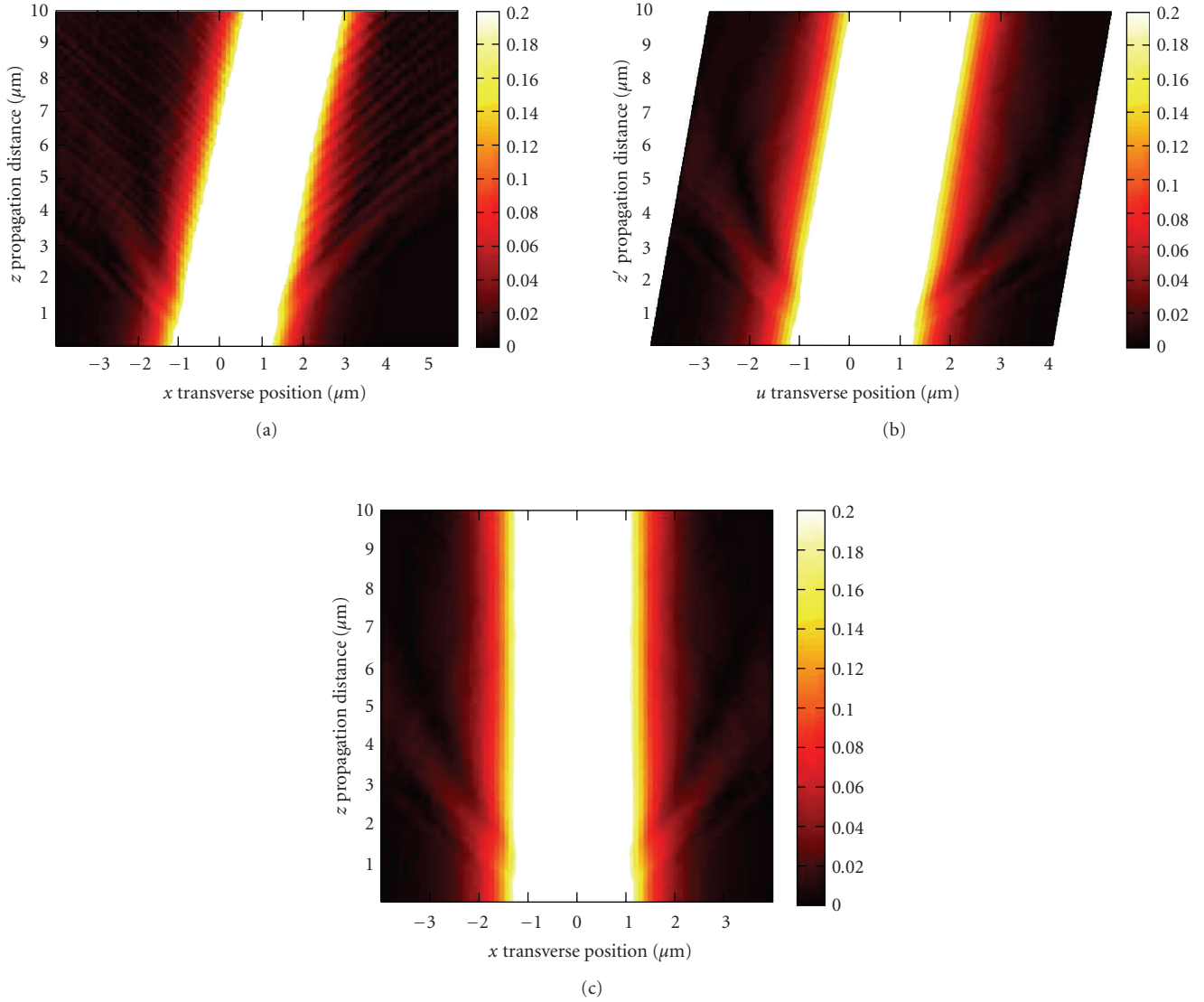


FIGURE 7: (a) Field surface plot for 10° tilted waveguide on Cartesian mesh. Scale has been capped to show the stair case noise. (b) Field surface plot for 10° tilted waveguide on oblique coordinate. (c) Field surface plot for straight waveguide on Cartesian mesh.

of a standard nontilted waveguide modelled on the Cartesian mesh in Figure 7(c) behaves similarly to the tilted waveguide modelled on oblique coordinate. Perfectly Matched Layer (PML) boundary condition is used to absorb the wave leakage from the waveguide and the nonphysical staircase noise. The slight leakage of the guided mode near the input of the waveguide is due to the mismatch of the analytical mode used to excite the waveguide and the actual numerical field solution. This leakage disappears as the propagating mode is settled in the waveguide.

4. Conclusion

The paper demonstrates the implementation of the DFF algorithm into the 3D scalar oblique BPM method. The accuracy and stability of the oblique DFF is investigated

on the 2D and 3D tilted waveguides and compared against the oblique CN-BPM method. The resulting method is computationally faster than oblique CN-BPM method and is suitable for parallel computing for further computational savings. It is noted that the appearance of the spurious mode can potentially limit the application of the DFF to very large tilted angles.

References

- [1] C. Vassallo, "Interest of improved three-point formulas for finite-difference modeling of optical devices," *Journal of the Optical Society of America A*, vol. 14, no. 12, pp. 3273–3284, 1997.
- [2] Y.-P. Chiou, Y.-C. Chiang, and H.-C. Chang, "Improved three-point formulas considering the interface conditions in the

- finite-difference analysis of step-index optical devices," *Journal of Lightwave Technology*, vol. 18, no. 2, pp. 243–251, 2000.
- [3] Y.-C. Chiang, Y.-P. Chiou, and H.-C. Chang, "Improved full-vectorial finite-difference mode solver for optical waveguides with step-index profiles," *Journal of Lightwave Technology*, vol. 20, no. 8, pp. 1609–1618, 2002.
 - [4] J. Yamauchi, Y. Nito, and H. Nakano, "A modified semivectorial BPM retaining the effects of the longitudinal field component and its application to the design of a spot-size converter," *Journal of Lightwave Technology*, vol. 27, no. 13, pp. 2470–2476, 2009.
 - [5] T. M. Benson, P. Sewell, S. Sujecki, and P. C. Kendall, "Structure related beam propagation," *Optical and Quantum Electronics*, vol. 31, no. 9, pp. 689–703, 1999.
 - [6] D. Z. Djurdjevic, T. M. Benson, P. Sewell, and A. Vukovic, "Fast and accurate analysis of 3-D curved optical waveguide couplers," *Journal of Lightwave Technology*, vol. 22, no. 10, pp. 2333–2340, 2004.
 - [7] S. Sujecki, P. Sewell, T. M. Benson, and P. C. Kendall, "Novel beam propagation algorithms for tapered optical structures," *Journal of Lightwave Technology*, vol. 17, no. 11, pp. 2379–2388, 1999.
 - [8] G. R. Hadley, "Slanted-wall beam propagation," *Journal of Lightwave Technology*, vol. 25, no. 9, pp. 2367–2375, 2007.
 - [9] J. Yamauchi, J. Shibayama, and H. Nakano, "Finite-difference beam propagation method using the oblique coordinate system," *Electronics and Communications in Japan, Part II: Electronics*, vol. 78, no. 6, pp. 20–27, 1995.
 - [10] P. Sewell, T. M. Benson, T. Anada, and P. C. Kendall, "Bi-oblique propagation analysis of symmetric and asymmetric Y-junctions," *Journal of Lightwave Technology*, vol. 15, no. 4, pp. 688–696, 1997.
 - [11] S. Sujecki, "Wide-angle, finite-difference beam propagation in oblique coordinate system," *Journal of the Optical Society of America A*, vol. 25, no. 1, pp. 138–145, 2008.
 - [12] S. Sujecki, "Generalized rectangular finite difference beam propagation method," *Applied Optics*, vol. 47, no. 23, pp. 4280–4286, 2008.
 - [13] H. A. van der Vorst, "Bi-CGSTAB: a fast and smoothly converging variant of Bi-CG for the solution of nonsymmetric linear systems," *SIAM Journal on Scientific Computing*, vol. 13, no. 2, pp. 631–644, 1992.
 - [14] D. W. Peaceman and H. H. Rachford, "The numerical solution of parabolic and elliptic differential equations," *Journal of the Society for Industrial and Applied Mathematics*, vol. 3, p. 28, 1955.
 - [15] H. M. Masoudi and J. M. Arnold, "Spurious modes in the DuFort-Frankel finite-difference beam propagation method," *IEEE Photonics Technology Letters*, vol. 9, no. 10, pp. 1382–1384, 1997.
 - [16] P. Sewell, T. M. Benson, and A. Vukovic, "A stable DuFort-Frankel Beam-Propagation method for lossy structures and those with perfectly matched layers," *Journal of Lightwave Technology*, vol. 23, no. 1, pp. 374–381, 2005.
 - [17] S. Sujecki, T. M. Benson, P. Sewell, and P. C. Kendall, "Novel vectorial analysis of optical waveguides," *Journal of Lightwave Technology*, vol. 16, no. 7, pp. 1329–1335, 1998.

Research Article

Controlled On-Chip Single-Photon Transfer Using Photonic Crystal Coupled-Cavity Waveguides

Hubert Pascal Seigneur,¹ Matthew Weed,¹ Michael Niklaus Leuenberger,^{2,3} and Winston Vaughan Schoenfeld¹

¹CREOL, The College of Optics and Photonics, University of Central Florida, Orlando, FL 32826, USA

²NanoScience Technology Center, University of Central Florida, Orlando, FL 32816, USA

³Department of Physics, University of Central Florida, P.O. Box 162385, Orlando, FL 32816, USA

Correspondence should be addressed to Hubert Pascal Seigneur, seigneur@creol.ucf.edu

Received 15 June 2010; Revised 21 September 2010; Accepted 1 November 2010

Academic Editor: Martin Cryan

Copyright © 2011 Hubert Pascal Seigneur et al. This is an open access article distributed under the Creative Commons Attribution License, which permits unrestricted use, distribution, and reproduction in any medium, provided the original work is properly cited.

To the end of realizing a quantum network on-chip, single photons must be guided consistently to their proper destination both on demand and without alteration to the information they carry. Coupled cavity waveguides are anticipated to play a significant role in this regard for two important reasons. First, these structures can easily be included within fully quantum-mechanical models using the phenomenological description of the tight-binding Hamiltonian, which is simply written down in the basis of creation and annihilation operators that move photons from one quasimode to another. This allows for a deeper understanding of the underlying physics and the identification and characterization of features that are truly critical to the behavior of the quantum network using only a few parameters. Second, their unique dispersive properties together with the careful engineering of the dynamic coupling between nearest neighbor cavities provide the necessary control for high-efficiency single-photon on-chip transfer. In this publication, we report transfer efficiencies in the upwards of 93% with respect to a fully quantum-mechanical approach and unprecedented 77% in terms of transferring the energy density contained in a classical quasibound mode from one cavity to another.

1. Introduction

In order to obtain an efficient quantum computing architecture, the general consensus is that various implementations of the qubit should be combined. This calls on the one hand for stationary qubits that are good for storage, such as atoms to be used at quantum network nodes, and on the other hand for flying qubits that have desirable properties for travel, such as photons to be used as quantum interconnects. Moreover, the storage qubits can map their quantum state onto the traveling qubits and vice versa by means of coherent interfaces [1–3]. With the intention of realizing an efficient quantum computing architecture, this composite qubit approach to a quantum technology has been proposed for ion trap qubits [4] and also for neutral atoms [5]. We, in addition, have proposed a similar approach in connection with semiconductor-based artificial atoms or quantum dots

[6]. Regardless of choice, these various implementations of the composite qubit architecture are only possible if single photons are able to be guided from one node to another with both high efficiency and fidelity.

Recently, the on-chip generation and transfer of microwave single photons have been demonstrated in connection with superconducting qubits via transmission line cavities [7–10]. In addition, the generation and transfer of single photons on photonic crystal chips using a 25 μm long defect waveguide structure has been studied by England et al. showing 12% transfer efficiency with quantum dots inside the nodes and 49% transfer efficiency without [11]. In this publication, we investigate the use of a photonic crystal coupled-cavity waveguide (CCW) for the generation and transfer of single photons on-chip. Such approach to an on-chip quantum network present several advantages. For example, since the photons we use have a wavelength of

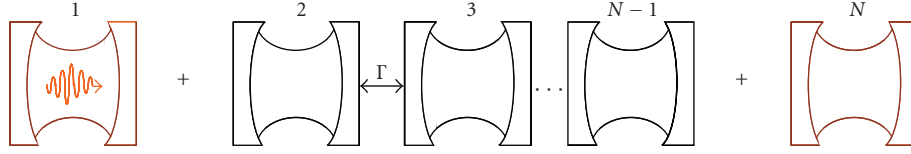


FIGURE 1: Two high-Q cavities connected via a coupled-cavity waveguide.

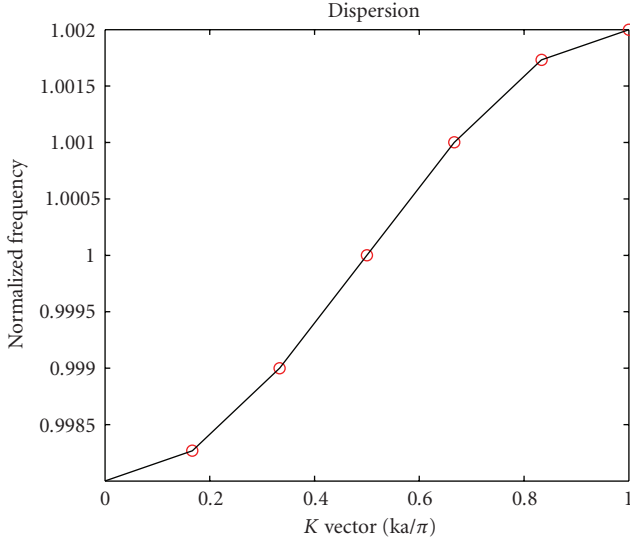


FIGURE 2: Dispersion of a 12 coupled-cavities waveguide.

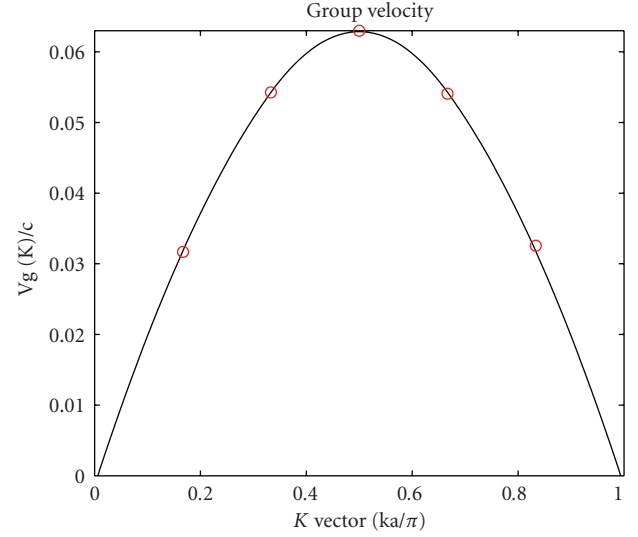


FIGURE 3: Group Velocity.

around $1\mu\text{m}$ (IR) as opposed to 1 cm or more (microwave), the surface area of a quantum network in any optical system would be a great deal smaller and thus much more suitable for on-chip integration. In addition, the transfer of microwave photons was shown to take few hundred nanoseconds, whereas the transfer of optical photons inside the photonic crystal chip is anticipated to take no more than few tens of picoseconds.

Furthermore, CCWs offer a truly unique and sophisticated control over the transport of single photons [12]. Because modes of CCWs resemble those of the high-Q cavity modes and possess the same field symmetries, these devices can be used to make bends with no reflection. In addition, they can dramatically slow down optical waves, and because of their versatile dispersion properties (both positive and negative dispersion are achievable), they allow for a great deal of control over a single-photon pulse propagation. Moreover, since each mode is strongly localized, the guided mode is composed of a linear combination of these individual bound modes. This renders the propagating mode easy to model quantum-mechanically [13], therefore allowing for their guiding behavior to be optimized with respect to maximized fidelity of quantum operations inside the quantum network. And, once their guiding behavior has been characterized with a few parameters, namely, the coupling coefficient κ and resonant frequency ω_c , their physical structure can be constructed to emulate their intended behavior.

The paper is organized as follows. The modeling of the on-chip single-photon transfer dynamics is described in Section 2. Included in that section are the single-photon pulse propagation characteristics, the engineering of the source/target cavity to waveguide dynamic coupling as well as resulting transfer efficiencies. A physical implementation of a CCW based on a photonic crystal structure for the purpose of transferring single photon on-chip is presented in Section 3. An analysis and discussion of the performance of CCWs is provided in Section 4, followed by a final summary and conclusions in Section 5.

2. Modeling On-Chip Single-Photon Transfer Dynamics

The device under investigation is depicted in Figure 1. It consists of two cavities, cavity 1 and cavity N , linked to one another by means of a CCW, consisting of cavity 2 through cavity $N - 1$. In this specific example, N is 12. The coefficient Γ describes the weak coupling between the cavities forming the waveguide.

A general Hamiltonian for this system is derived from the tight-binding Hamiltonian and it is shown in (1). \hat{a}_j^\dagger and \hat{a}_j are the creation and the annihilation for the field in the j th cavity, ω_c is the resonant cavities frequency, $V_{C1-W}(t)$ is the time-dependent interaction between the first cavity and the

waveguide, and $V_{W-C_N}(t)$ is the time-dependent interaction between the waveguide and the last cavity

$$\hat{H} = \sum_j \hbar\omega_c \hat{a}_j^\dagger \hat{a}_j + \sum_{j=2}^{N-2} \Gamma (\hat{a}_j^\dagger \hat{a}_{j+1} + \hat{a}_{j+1}^\dagger \hat{a}_j) + V_{C_1-W}(t) + V_{W-C_N}(t). \quad (1)$$

Our key concern in this publication is the engineering of the interaction between cavities and the waveguide structure $V_{C_1-W}(t)$ and $V_{W-C_N}(t)$. First, we consider the waveguide by itself and design its characteristics. Then, both the cavities and the waveguide are considered, and the system is engineered such that the photon is unloaded into the

waveguide and transferred to its destination with minimum loss.

2.1. Waveguide. First, it is useful to consider a CCW by itself. The Hamiltonian that can describe such a waveguide is exactly the tight-binding Hamiltonian in

$$\hat{H}_{TB} = \sum_j \hbar\omega_c \hat{a}_j^\dagger \hat{a}_j + \sum_j \Gamma (\hat{a}_j^\dagger \hat{a}_{j+1} + \hat{a}_{j+1}^\dagger \hat{a}_j), \quad (2)$$

In the Wannier representation, essentially a real-space picture of localized orbitals, this Hamiltonian matrix is written as

$$\hat{H}_{TB} = \begin{array}{c} \begin{array}{cccccccccccccc} \langle 1_n | & \langle 2_n | & \langle 3_n | & \langle 4_n | & \langle 5_n | & \langle 6_n | & \langle 7_n | & \langle 8_n | & \langle 9_n | & \langle 10_n | & \langle 11_n | & \langle 12_n | \\ \begin{bmatrix} E_c & \Gamma & 0 & 0 & 0 & 0 & 0 & 0 & 0 & 0 & 0 & \Gamma \\ \Gamma & E_c & \Gamma & 0 & 0 & 0 & 0 & 0 & 0 & 0 & 0 & 0 \\ 0 & \Gamma & E_c & \Gamma & 0 & 0 & 0 & 0 & 0 & 0 & 0 & 0 \\ 0 & 0 & \Gamma & E_c & \Gamma & 0 & 0 & 0 & 0 & 0 & 0 & 0 \\ 0 & 0 & 0 & \Gamma & E_c & \Gamma & 0 & 0 & 0 & 0 & 0 & 0 \\ 0 & 0 & 0 & 0 & \Gamma & E_c & \Gamma & 0 & 0 & 0 & 0 & 0 \\ 0 & 0 & 0 & 0 & 0 & \Gamma & E_c & \Gamma & 0 & 0 & 0 & 0 \\ 0 & 0 & 0 & 0 & 0 & 0 & \Gamma & E_c & \Gamma & 0 & 0 & 0 \\ 0 & 0 & 0 & 0 & 0 & 0 & 0 & \Gamma & E_c & \Gamma & 0 & 0 \\ 0 & 0 & 0 & 0 & 0 & 0 & 0 & 0 & \Gamma & E_c & \Gamma & 0 \\ \Gamma & 0 & 0 & 0 & 0 & 0 & 0 & 0 & 0 & 0 & \Gamma & E_c \end{bmatrix} & \begin{array}{l} |1_n\rangle \\ |2_n\rangle \\ |3_n\rangle \\ |4_n\rangle \\ |5_n\rangle \\ |6_n\rangle \\ |7_n\rangle \\ |8_n\rangle \\ |9_n\rangle \\ |10_n\rangle \\ |11_n\rangle \\ |12_n\rangle \end{array} \end{array} \end{array}, \quad (3)$$

where state $|1_n\rangle$ corresponds to the Wannier function localized in the first cavity forming the CCW, and state $|2_n\rangle$ corresponds to the Wannier function localized in the second cavity forming the waveguide, and so on. The diagonal matrix element for each site is E_c , this is the energy of the resonant mode for each cavity. Periodic boundary conditions are expressed at the waveguide ends as $\hat{a}_1^\dagger = \hat{a}_{12}^\dagger$ and $\hat{a}_1 = \hat{a}_{12}$.

2.2. Dispersion, Group Velocity, and GVD. It is assumed that the wavelength of the single photon λ_{ph} of $1.182 \mu\text{m}$, which is a realistic wavelength for a GaAs/InGaAs-based QD emitter. This wavelength corresponds to the cavity resonant frequency $\omega_c = 1.594 \cdot 10^{15} \text{ rad/s}$, where $E_c = \hbar\omega_c$. Next, assuming a quality factor $Q = 1000$ for each cavity of the CCW, the coupling rate between neighboring cavities is thus calculated to be $\Gamma = 1.594 \cdot 10^{12} \text{ rad/s}$, where Γ is defined as ω_c/Q . This definition of Γ assumes that coupling to the nearest neighbor cavity is the only loss channel, that is, out-of-plan losses are ignored.

The dispersion relation of this CCW is solved from the diagonalization of the Hamiltonian matrix. Although working in a real space representation, the problem is fully equivalent to the reciprocal space-based Bloch representation. In fact, for N sites, Nk points exist in reciprocal space and are defined as $k = 2\pi\mathbf{K}/Na$ where \mathbf{K} is a quantum number such that $\mathbf{K} = -N/2 + 1, \dots, N/2$ and a the lattice constant of the periodic waveguide. As a result, the same energy eigenvalues are obtained. They are plotted in red for the normalized positive k points of the first Brillouin zone in Figure 2.

The dispersion obtained numerically matches very well the theoretical dispersion for CCWs in (4) in the linear dispersion approximation. Under this approximation, we assume weak coupling, which means that photons may only leak into the nearest neighbor cavity [14–18]. The tight-binding model yields the optical carrier frequencies

$$\omega_k = \omega_c [1 + \kappa \cos(ka)], \quad (4)$$

where ω_c is the resonant frequency of a single cavity, κ is the coupling coefficient between cavities, k is the Bloch wave

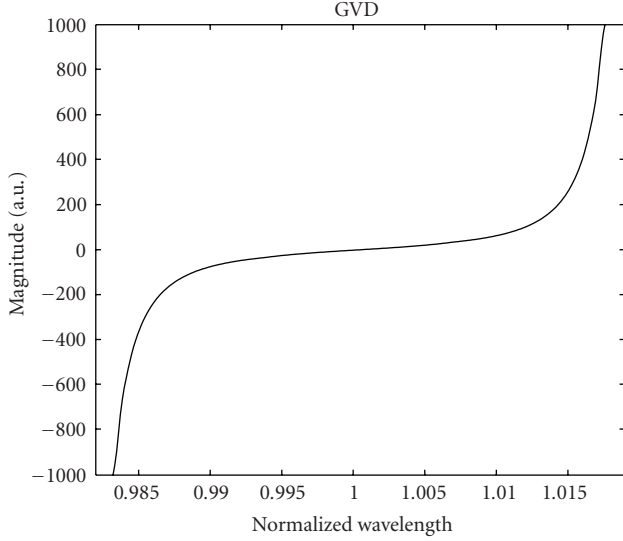


FIGURE 4: Group Velocity Dispersion.

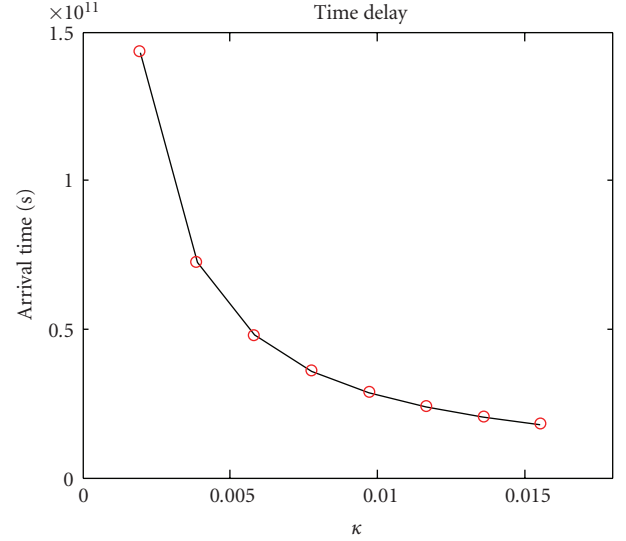


FIGURE 6: Time Delay.

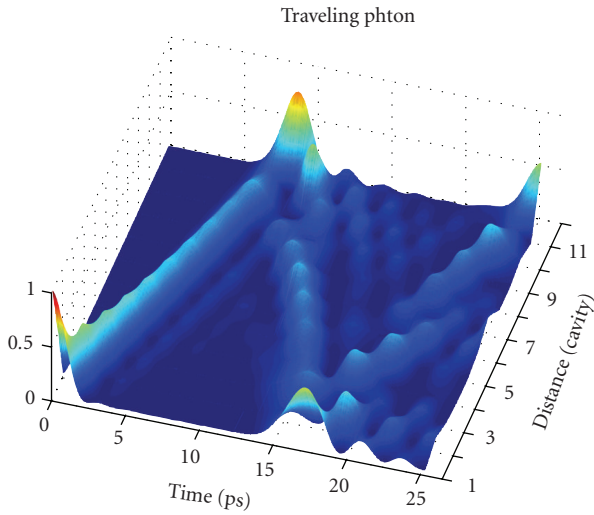


FIGURE 5: Traveling Photon.

number, and a is the lattice constant. For this waveguide, the coupling coefficient was found to be $\kappa = -0.002$.

An expression for the group velocity v_g can be derived from (4) as follows:

$$v_g = \nabla_k \omega_k = -\omega_c \kappa a \sin(ka). \quad (5)$$

The group velocity v_g normalized over c (the speed of light in vacuum) is plotted in Figure 3 throughout the normalized coupled cavity waveguide band. It is obtained by taking the derivative of obtained energy eigenvalues with respect to k . At the edges of the waveguide band, that which corresponds to when k is 0 or 1, the group velocity tends toward zero.

This result has two important consequences. First, the group velocity dispersion is ill defined when k is 0 or 1 according to the standard definition in (6). Second, the

group velocity dispersion may be either positive or negative depending on which band edge k is closest to

$$\text{GVD} = -\left(\frac{2\pi c}{\lambda^2}\right) \frac{d}{d\omega} \left(\frac{1}{v_g(k)}\right). \quad (6)$$

The group velocity dispersion (GVD) for the 12 cavities forming the waveguide is plotted in Figure 4 within the CCW band. For practical applications, Mookherjea derived more appropriate definitions of GVD that satisfy a small fractional change of the GVD coefficient over the range of frequencies of interest [19].

2.3. Single-Photon Propagation. A single-photon pulse is shown propagating for the waveguide composed of 12 cavities in Figure 5. The time dependence for the coupled-cavity waveguide is obtained numerically using the Louiville or Von Neumann Equation (similar to the approach discussed in [20]) in conjunction with the tight-binding Hamiltonian to solve for the time evolution of the density matrix whose states correspond to the Wannier functions localized in the cavities forming the waveguide. It is assumed that there are neither any out-of-plane losses or material absorption causing the CCW mode to decay nor any scattering resulting in a sudden change of the phase.

The single photon pulse can be seen traveling from cavity 1 to Cavity 12 in about 9 picoseconds before being reflected. An oscillatory structure at the trailing edge of the pulse can be noticed. We believe this feature has to do with the single-photon pulse defined initially at a precise point in space and time. The consequence is a wideband single-photon pulse, and therefore higher-order terms can no longer be neglected resulting in envelope distortion. It is also helpful to compare that propagation time with the decoherence time of atoms or QDs. The time it takes to transfer a photon from a source cavity to a target cavity is a relatively fast process compared to the decoherence processes associated

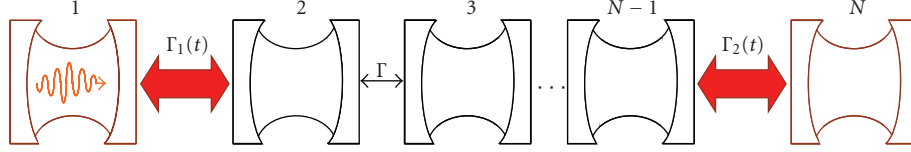


FIGURE 7: Unloading/loading by means of time-varying coupling coefficients.

with electron spin qubits in self-assembled QD (our storage qubit of interest). In a recent publication of ours [20], we showed how the coherent exchange between a photon qubit and an electron spin qubit in a QD is affected by decoherence resulting from hyperfine interactions. Although these decoherence processes prevented the interacting qubits from reaching maximum entanglement, there were at least partially entangled. It is important to note that these interactions were taking place over a longer period of time, about 1 to 2 orders of magnitude longer than the time needed for a photon to propagate down 12 cavities. In addition, a novel scheme based on ultrafast optical spin echo shows that decoherence times on the order of microseconds are achievable [21]. Therefore, it is anticipated that the propagation time of the photon will not be much of an issue over small to medium range distances.

Figure 5 also depicts the single-photon pulse propagation in the linear region of the CCW; therefore, the single-photon frequency is tuned to the middle of the waveguide band. (This corresponds to a normalized frequency equal to 1 in Figure 2.) As a result, ignoring the oscillatory structure at the trailing edge of the pulse, a pulse propagates mostly unchanged in shape. On the other hand, when the single-photon pulse propagation is determined by the flat region of the CCW dispersion corresponding to one of the edges of the transmission band, there exists a considerable slowing of the group velocity. Figure 6 depicts the travel time from cavity 1 to cavity 12 as a function of coupling coefficient κ .

2.4. Engineering Cavity-Waveguide Couplings. Dynamically coupling the end cavities to the waveguide can be achieved in two different ways. On one hand, this can be done by setting all the resonant modes to be the same for all cavities including the end cavities while varying the coupling coefficients between the end cavities and the waveguide in time in order to load and unload the photon from and onto the waveguide. This is depicted in Figure 7, and its corresponding Hamiltonian is described in

$$\hat{H} = \sum_j \hbar \omega_c \hat{a}_j^\dagger \hat{a}_j + \sum_{j=2}^{N-2} \Gamma (\hat{a}_j^\dagger \hat{a}_{j+1} + \hat{a}_{j+1}^\dagger \hat{a}_j) + \Gamma_1(t) (\hat{a}_1^\dagger \hat{a}_2 + \hat{a}_2^\dagger \hat{a}_1) + \Gamma_2(t) (\hat{a}_{N-1}^\dagger \hat{a}_N + \hat{a}_N^\dagger \hat{a}_{N-1}). \quad (7)$$

On the other hand, dynamic coupling can also be completed by setting coupling coefficients to be the same for all cavities including the end cavities while varying the resonant modes of cavity 2 and cavity $N - 1$ in time in order to load and unload the photon from and onto the waveguide. This is

depicted in Figure 8, and its corresponding Hamiltonian is described in

$$\hat{H} = \sum_{j \neq 2, N-1} \hbar \omega_c \hat{a}_j^\dagger \hat{a}_j + \hbar \omega_2(t) \hat{a}_2^\dagger \hat{a}_2 + \hbar \omega_{N-1}(t) \hat{a}_{N-1}^\dagger \hat{a}_{N-1} + \sum_{j=1}^{N-1} \Gamma (\hat{a}_j^\dagger \hat{a}_{j+1} + \hat{a}_{j+1}^\dagger \hat{a}_j). \quad (8)$$

In practice, both of these approaches can be realized by means of a spatial modulation of the refractive index within the quantum network. In order for these loading and unloading operations to be feasible in a functioning quantum network though, they must be performed at speeds much greater than usual decoherence possesses therefore requiring the assistance of ultrafast optical pulses. Methods for the dynamical tuning of refractive index are based on nonlinear effects, carrier injection by linear absorption of an optical pump (free-carrier plasma dispersion effect), carrier injection using a PIN diode, or thermal tuning via optical heating. We are interested in carrier injection by linear absorption of an optical pump which many groups have shown to be a viable method. For example, Tanaka et al. demonstrated a change in cavity Q from 12,000 to 3,000 in 4 ps [22]. Lipson's group at Cornell University used a 100 fs pump pulse to generate a 18 ps index change pulse [23] and also demonstrated how a 1.5 ps pump pulse corresponding to a 25 ps index change pulse could change the Q factor of a cavity from 60000 to 17000 [24]. Tanabe et al. generated a 14 ps pump pulse resulting in a change in photon lifetime from 320 ps to 70 ps inside a high Q cavity [25]. Carrier injection using PIN diode is an interesting alternative and allows for both the injection and extraction of carrier simultaneously. The resulting shape of the free carrier index change looks a lot like a square pulse. Gardes et al. showed a 7 ps rise and fall time in the index change was possible [26].

2.5. Transfer Efficiencies. On-chip on-demand single-photon transfer stipulates that the photon is unloaded onto a waveguide from a cavity 1 at a time t_1 allowing it to travel down the waveguide before being loaded into a cavity 2 at a time t_2 . Considering the two approaches mentioned in the previous section, a critical question to be answered is what transfer efficiencies can be obtained.

First, we consider the case of time-varying coupling coefficients. The unloading of the photon onto the waveguide is achieved by dynamically switching the magnitude of the coupling coefficient between cavity 1 and cavity 2 starting at t_1 . Perhaps, this can be realized using an approach similar to Noda's [22]. Then, the loading of the photon from

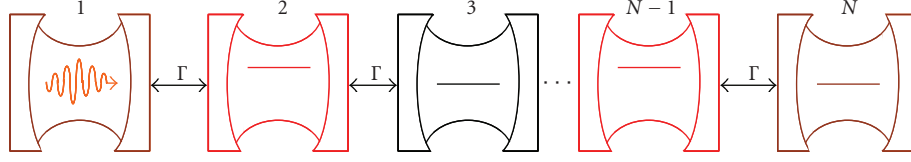


FIGURE 8: Unloading/loading by means of time-varying resonant frequencies

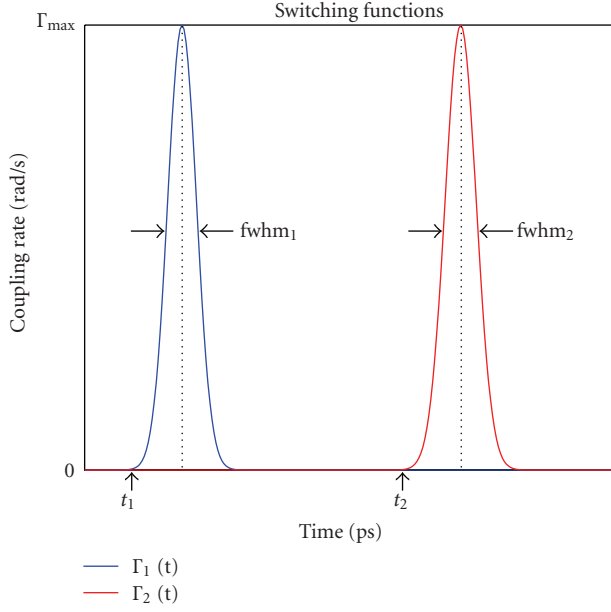
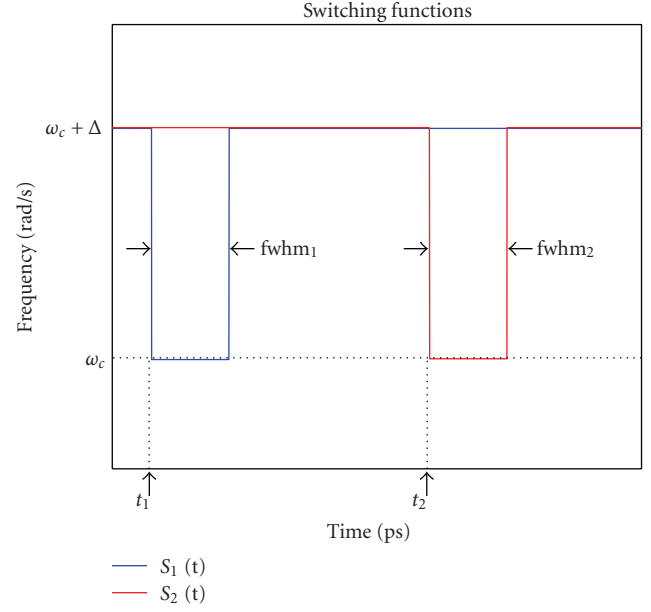
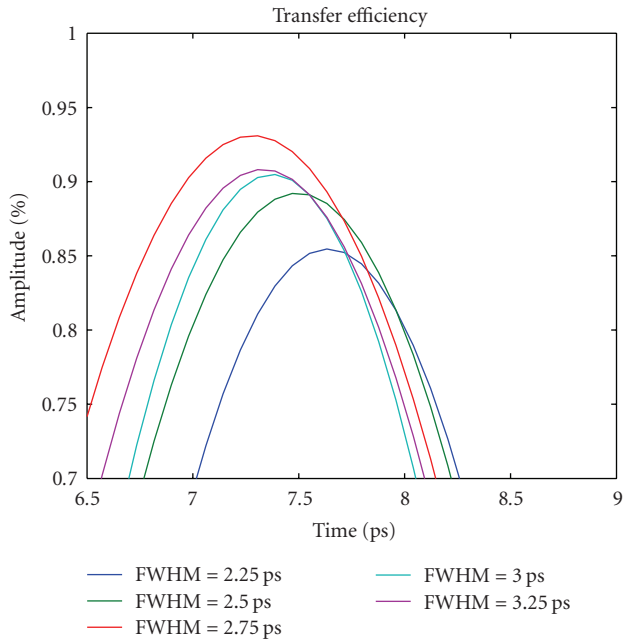
FIGURE 9: Switching functions $\Gamma_1(t)$ and $\Gamma_2(t)$.FIGURE 11: Switching functions $S_1(t)$ and $S_2(t)$.

FIGURE 10: Transfer efficiency with time-varying coupling coefficients.

the waveguide into cavity N is achieved by once again dynamically switching the magnitude of coupling coefficient between cavity $N - 1$ and cavity N starting at t_2 .

Design parameters of interest for both switching functions, $\Gamma_1(t)$ and $\Gamma_2(t)$, are their shape or time dependence, the range of coupling strength over which they are varied, the window in time over which they should be varied. There are also few design constraints. The temporal width of $\Gamma_1(t)$ or FWHM should be larger than the natural cavity decay into the CCW so as to allow the photon to escape yet smaller than round trip time. Similarly, properties of $\Gamma_2(t)$ will greatly depend on factors such as the CCW length, the group velocity, or the group velocity dispersion. Figure 9 shows the switching functions $\Gamma_1(t)$ and $\Gamma_2(t)$ qualitatively.

It was found that the optimum shape of switching functions $\Gamma_1(t)$ and $\Gamma_2(t)$ is a Gaussian profile. In a CCW with constant coupling between its cavities, when a photon is allowed to propagate freely, though highly localized initially (effectively represented by a delta function in space), it eventually exhibits a distribution in space that happens to be well approximated by a Gaussian. It may be that the distribution could be also approximated by other functions, for example, a squared hyperbolic secant. The authors believe it is worth further investigating the mechanism behind the broadening associated with the probability of finding the

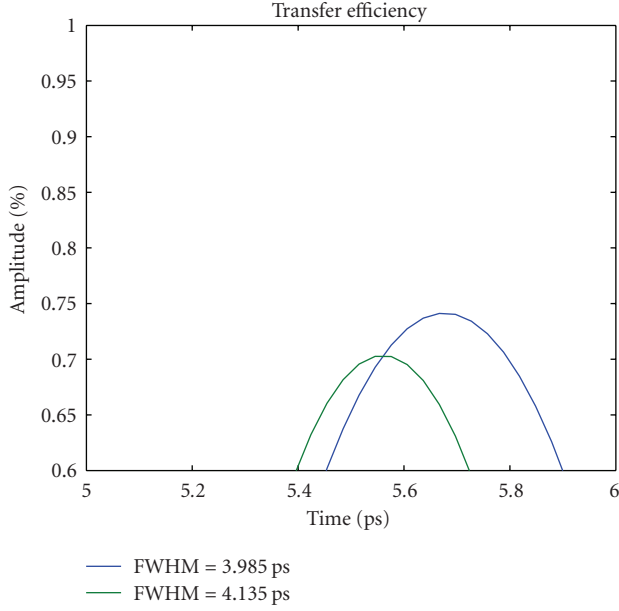


FIGURE 12: Transfer efficiency with time-varying resonant frequencies.

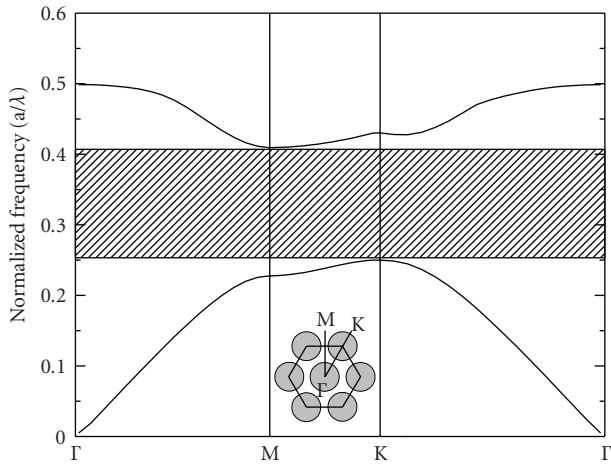


FIGURE 13: TE band diagram of a 2D photonic crystal with circular scatterers in a triangular lattice. The structure simulated here is a hole type crystal of index 3.4.

photon in space. In any case, this is certainly related to the fact that the coupled cavities have a finite Q which introduces an uncertainty in the time over which the photons actually hops from one cavity to the next. That being said, the context of Figure 9 is slightly different as it relates not just to a waveguide with constant coupling coefficient but to time-varying coupling coefficients. In other words, the coupling constant between two quasi-bound modes that are degenerate in frequency is varied. And the cavity Q depends on the coupling $\Gamma(t)$ where $Q = \omega/\Gamma(t)$. Providing that the switching function $\Gamma(t)$ has a Gaussian shape, the $Q(t)$ will also have a Gaussian shape, thus allowing for minimum reflections at the target cavity boundaries since the incoming

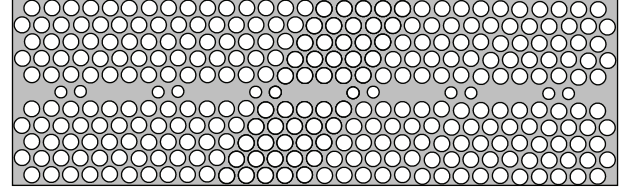


FIGURE 14: Structure of the high-Q cavity intended as a classical embodiment to the $j = 1$ and $j = N$ cavities in the quantum model above.

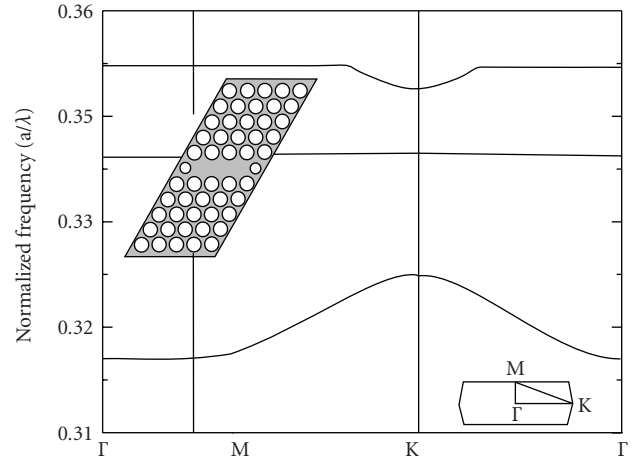


FIGURE 15: PWE calculation of our defect mode of interest over the full first Brillouin Zone. The cavity supercell is shown in the inset. There are only confined, nondispersive modes in the M crystal direction but along the K crystal direction, our intended direction of CCW propagation, dispersion is observed.

photon also has a Gaussian-like probability distribution in time.

As far as the range over which the coupling strength should be varied for $\Gamma_1(t)$, it is assumed that there is not any coupling, initially, between cavity 1 and cavity 2, yielding $\Gamma_1(0) = 0$. However, the maximum of the Gaussian shaped switching function is designed to be $\Gamma_{\max} = 1.594 \cdot 10^{12}$ rad/s, which corresponds to the regular coupling rate between neighboring cavities of the CCW. The minimum FWHM for $\Gamma_1(t)$ that allows the entire photon to leak out of the cavity was found to be 3 ps. The characteristics of $\Gamma_2(t)$ are engineered so as to maximize the transfer efficiency.

Figure 10 shows transfer efficiencies for various FWHM for $\Gamma_2(t)$ and a large range of t_2 . These transfer efficiencies are calculated assuming $\Gamma_1(t)$ with a FWHM equal to 3 ps, a peak coupling rate equal to $1.594 \cdot 10^{12}$ rad/s, and t_1 equal to 1.5 ps. A maximum transfer efficiency of 93% is obtained for $\Gamma_2(t)$ with a FWHM equal to 2.75 ps and a starting time t_2 equal to 7.25 ps. The transfer efficiency is defined as the ratio of the probability of finding a photon in cavity N following its capture (once $\Gamma_2(t)$ goes back to zero) over the probability of finding a photon in Cavity 1 before its release (when $\Gamma_1(0) = 0$), which is always unity.

Next, the case of time-varying resonant frequencies is considered. The unloading of the photon onto the waveguide

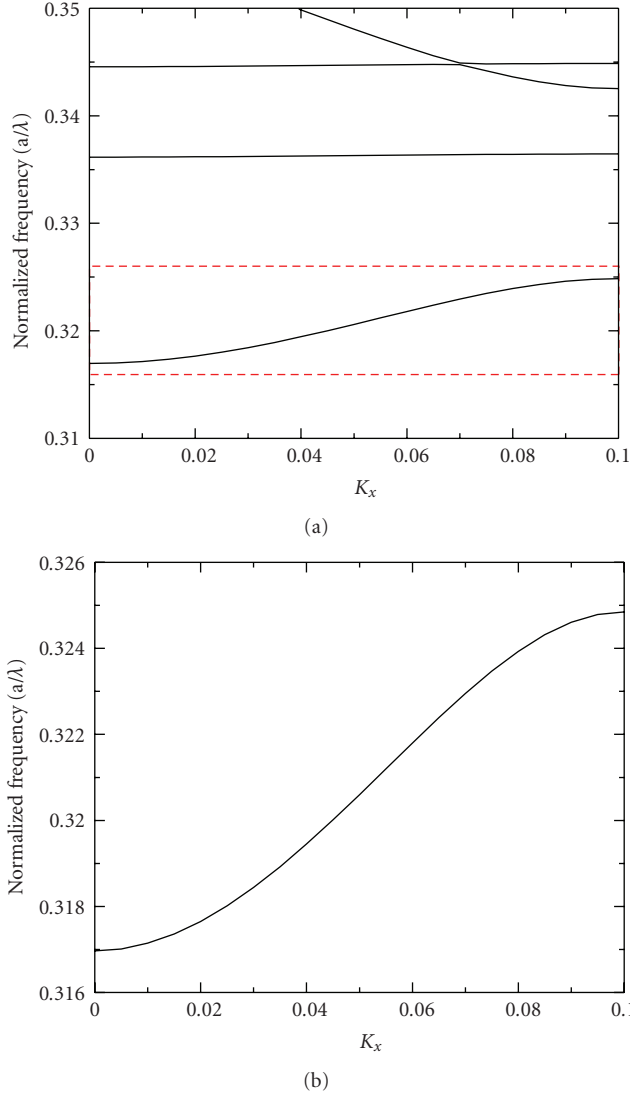


FIGURE 16: Dispersion relation for the L3s2 CCW structure described above. (a) we see that many modes exist in the crystal's photonic band gap, some with high confinement that result in no dispersion and others that allow coupled-cavity resonance for propagation that result in the sinusoidal k-relation from (4). The mode of interest is selected and zoomed in upon for (b).

is achieved by dynamically switching the resonant frequency of cavity 2 from $\omega_c + \Delta$ to ω_c starting at t_1 . Then, the loading of the photon from the waveguide into cavity N is achieved by dynamically switching the resonant frequency of cavity $N - 1$ from $\omega_c + \Delta$ to ω_c starting at t_2 and subsequently from ω_c back to $\omega_c + \Delta$.

Design parameters of interest for both switching functions, $S_1(t)$ and $S_2(t)$, are their shape or time dependence, the range of frequencies over which the cavity resonant frequencies are varied, the time window over which resonant frequencies should be varied. As far as design constraints, it is desirable that the amount of detuning Δ for the resonant frequency of the “barrier” cavities to be larger than the waveguide bandwidth to avoid any significant

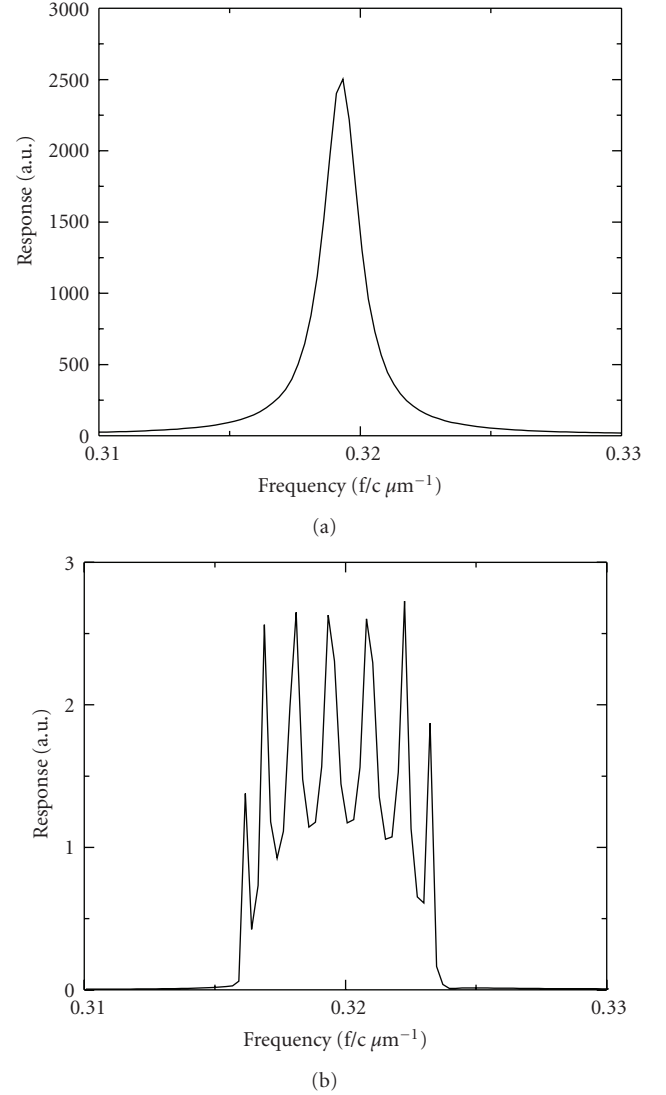


FIGURE 17: (a) represents the spectra inside a single L3s cavity isolated from any other cavities, while (b) represents the spectra through a 7 cavity coupled L3s2 system. Results calculated from FDTD.

coupling between the waveguide and the end cavities. Also, the duration of $S_1(t)$, which is the time during which the resonant frequency of cavity 2 is switched from $\omega_c + \Delta$ to ω_c , should be large enough for the photon to escape, yet smaller than the round trip time. Similarly, $S_2(t)$ needs to be large enough for the photon to be captured. Figure 11 shows $S_1(t)$ and $S_2(t)$ qualitatively.

It was found that the optimum shape for $S_1(t)$ and $S_2(t)$ is a square profile. In the case of the time-varying frequency scheme, the coupling is mostly dictated by ω ($\Gamma \ll \omega$), so until the frequency of the “barrier” cavity matches the frequencies of adjacent cavities, the probability of tunneling through is insignificant. That explains why a square profile is more appropriate. Earlier, in the case of the time-varying coupling coefficient scheme, the difference was that all the ω 's were the same; therefore, the probability of tunneling

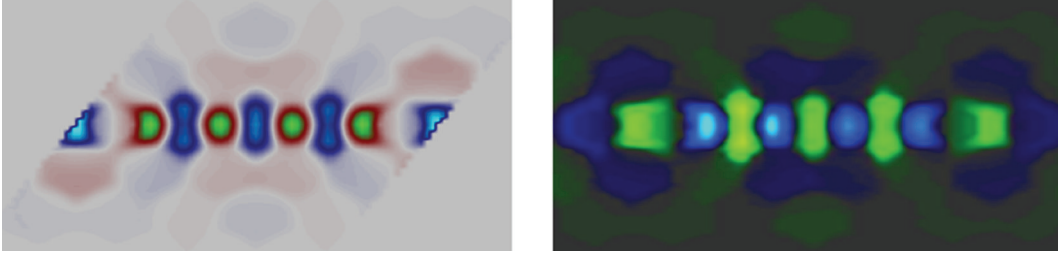


FIGURE 18: Simulated CCW modes in the L3s2 system. On the left, a PWE calculation of the allowed mode corresponding to the dispersive mode in Figure 15 matches well with the FDTD simulation of the propagating mode on the right, both showing the out of plane field component (H_y).

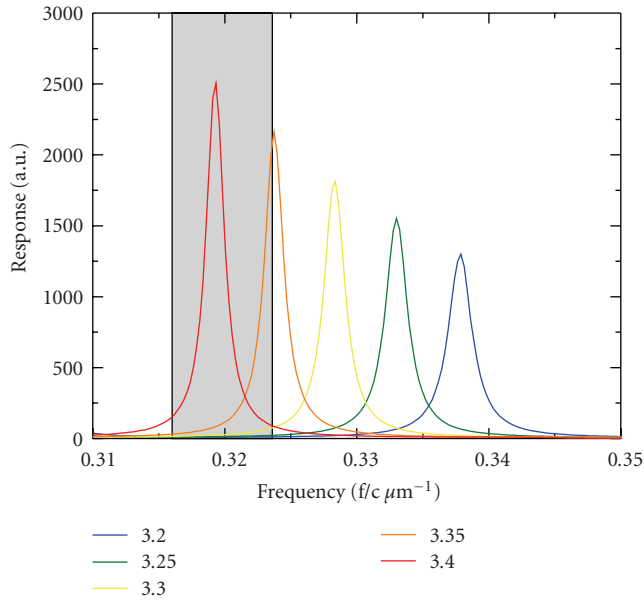


FIGURE 19: Cavity resonance shifting due to a change in material index of refraction. Using a standard index of 3.4 (red) as our base, to comply with Si or GaAs substrates, switching the barrier regions of our heterostructured cavity to an index of 3.3 (yellow) offers negligible overlap between “barrier” cavity resonances and the waveguide bandwidth (grey). Further confinement would be possible with lower switched index but is less physically reasonable.

through was only depending on $\Gamma(t)$. In fact, much higher transfer efficiencies were achieved for the time-varying frequency scheme with a square shape switching function with the prescribed duration (about 75%) compared to a Gaussian shape switching function with a wide range of duration (no more than 10%). The authors believe that the transfer efficiency could further be improved if the switching function was switched on and off adiabatically, resulting in a rounded square shape. In addition, the switching function duration is now chosen to correspond to approximately twice the photon lifetime in the “barrier” cavity since the photon has to both enter and exit the “barrier” cavity before it can reach the target cavity.

As far as the range over which the resonant frequency of the “barrier” cavities should be varied, we assume that each

cavity in the CCW has a Q of 1000 resulting in a coupling coefficient of $\Gamma = 1.594 \cdot 10^{12}$ rad/s at the wavelength of interest and a bandwidth of $BW = \omega \pm \kappa = 1 \pm 0.002$ in normalized units of frequency. In our case, this corresponds to $BW = 1.59 \cdot 10^{15} \pm 3.18 \cdot 10^{12}$ rad/s. Consequently, we designed the detuning parameter to be $\Delta = 3.24 \cdot 10^{12}$ rad/s such that $|\kappa| \leq \Delta \ll \omega$. Therefore, by switching “barrier” cavity frequencies from ω_c to $\omega_c + \Delta$, we are able to prevent coupling between the end cavities and the CCW.

Figure 12 shows transfer efficiencies for various FWHM for $S_2(t)$ and a large range of t_2 . These transfer efficiencies are calculated assuming $S_1(t)$ with a FWHM equal to 4.875 ps and t_1 equal to 1.5 ps. A maximum transfer efficiency of 75% is obtained for $S_2(t)$ with a FWHM equal to 3.985 ps and a starting time t_2 equal to 5.7 ps.

3. Physical Design

As a sort of proof of principal, a classical optical system was designed to compare and contrast the propagation properties of light in CCW systems. Using photonic crystal as a means to integrate such a coupled system allows great potential for high density integration of waveguides and high- Q cavities that are readily reproducible in fabrication. There has been much work showing from both theory and experiment, that photonic crystal CCW systems can exploit the unique dispersive properties discussed previously for applications of slow light pulse compression and transparency [27–30]. Many different systems have been shown to stop light including traditional defect waveguides with side-coupled integrated sequence of resonators. Initially, these systems seem identical to CCW structures; they both exhibit a cosine-like dispersion relation inside the photonic bandgap, which is eventually flattened adiabatically to stop the light. Differences become apparent when one consider the photonic wave function. In the CCW system under consideration, a highly localized photonic wave function is anticipated once the light is stopped, that is, within a single cavity. On the other hand, for defect waveguides with side-coupled integrated sequence of resonators, the photonic wave function would be spread over the defect waveguide and several cavities. For the reasons just mentioned, a CCW structure decrease device footprint. In addition, CCW structures lend themselves more readily to cavity QED applications. In this publication we focus on the maneuvering of light through a network of cavities only.

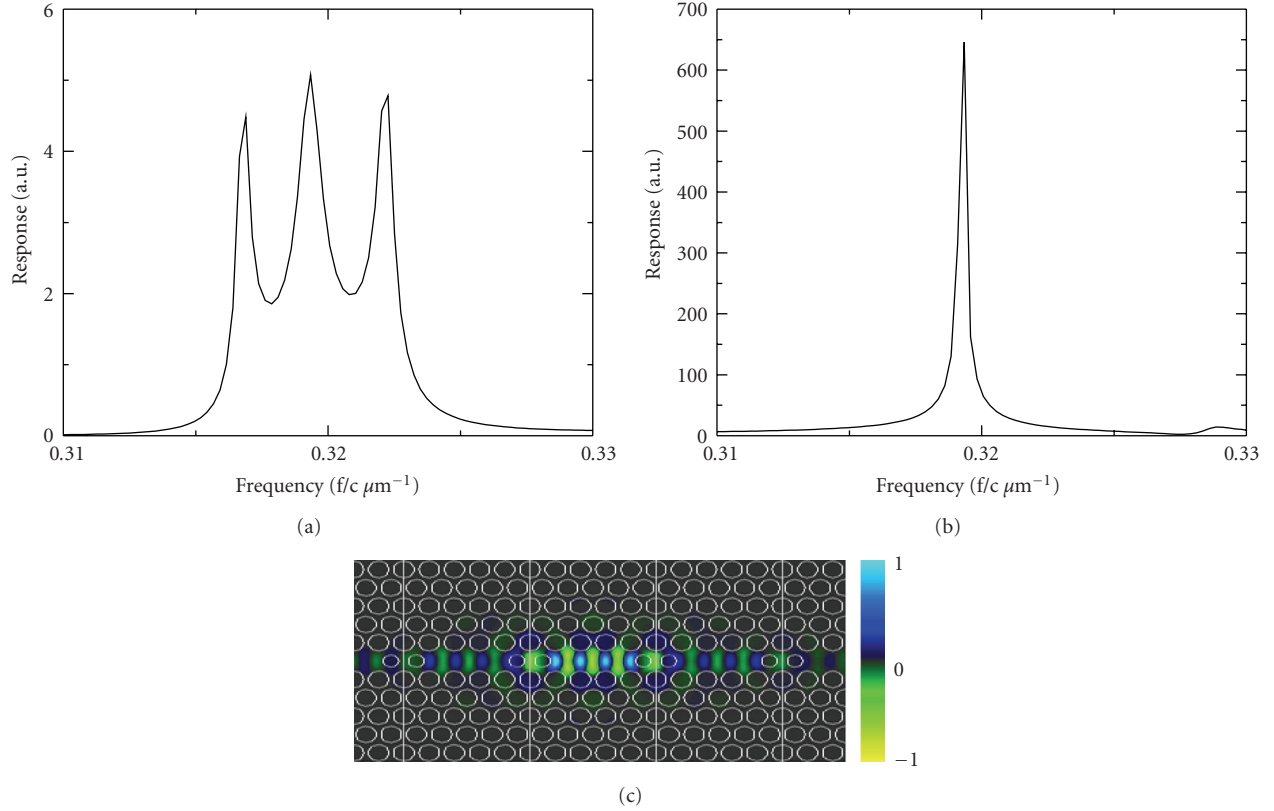


FIGURE 20: (a) spectra of 3 coupled cavities simulated through FDTD. (b) the first and third cavities have been index switched to show spectra that now represents an isolated heterostructured High-Q cavity. The spatial mode profile of this High-Q mode is also shown in (c).

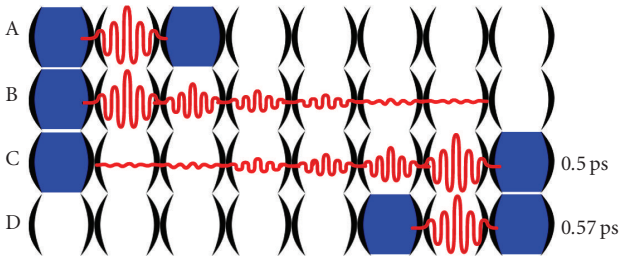


FIGURE 21: High Q cavity mode release and capture process. A shows the confined cavity with both barriers activated with an index of 3.3. B shows the opening of the inside cavity by index switching to $n = 3.4$. With the second cavity's outside barrier closed, C, the energy accumulates and is then trapped by closing the inner barrier of the second cavity in D.

The coupling of cavity modes to waveguide modes has been a topic of intense research effort for the realization of both quantum and classical integrated optical circuit [11, 31, 32]. It is therefore useful, in photonic crystal devices, to design similarities between isolated cavity modes and propagating CCW modes. This similarity makes for efficient coupling toward the effort of release and capture of optical energy as well as bends and splitters for waveguide routing [33, 34]. The bandwidth of a CCW band may also be adjusted by changing localization properties of the cavities, or the coupling strength (overlap integral) between

the localized cavity modes. For instance, decreasing the intercavity distance leads to a wider bandwidth [35].

With many such degrees of design freedom that impact the modes of both the isolated cavity and the CCW, use of photonic crystal cavities for analysis of a coupled cavity system is a fruitful choice. The remainder of this section will review the methods and findings of the design and characterization of a CCW system with isolated cavity release and capture switching ability.

3.1. Numerical Methods. Analysis of our classical system makes use of the standard numerical simulation tools employed in photonic crystal devices, Plane Wave Expansion (PWE), and Finite-Difference Time Domain (FDTD). The proposed embodiment of this CCW system in a photonic crystal featuring a triangular lattice of circular holes will be performed for TE (even) polarized light only. This choice of polarization allows both a more comfortable band gap in which to engineer defects as well as a more accurate approximation from a 3D slab to a 2D effective index method approximation for future work. All results presented herein may be taken as approximations to a 3D finite slab or simply as a proof of concept in an infinite 2D system. The potential barriers and loss mechanisms for moving to a fully 3D model will be discussed later.

PWE provides an initial glimpse of the resonant behavior of these index-periodic metamaterials. The band in which the structure exhibits this periodicity-induced resonance, as

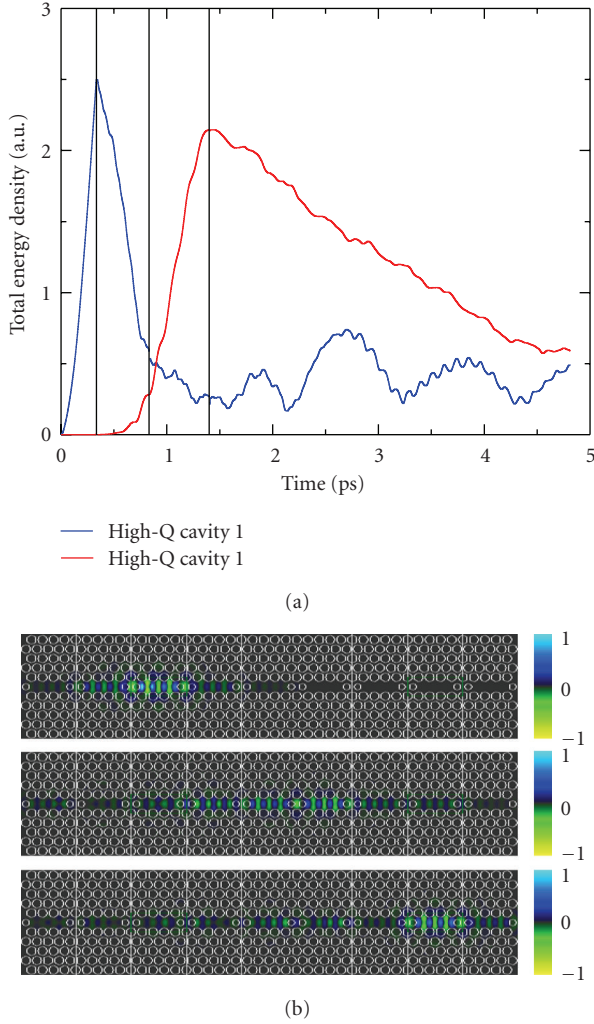


FIGURE 22: Three step release of an optical mode in a high-Q cavity into a CCW and capture into a second high-Q cavity with 77% efficiency. Energy density (a) and field evolution (b) are shown to illustrate the process.

shown in Figure 13 represents a range of frequencies in which light is not allowed to propagate in the structure.

It is then, in this forbidden spectral range that engineered crystal defects lead to allowed optical modes that may be localized (cavities) or allowed to propagate (waveguides). PWE will also provide the means to find the dispersion relation for our coupled-cavity waveguide modes which is key to the calculation of GVD.

Finally, FDTD is implemented to study the spectral response as well as the operational efficiency of these devices. This simulation tool allows the designers to observe how their device would operate under perfect conditions.

3.2. Structure. The envisioned system will consist of coupled cavities which exhibit guided modes as well as well-confined cavities that will exhibit high Q -factors in comparison. Lengths of CCW cavities will act as transmission lanes between the high- Q cavities and so the resonances of the two

structures will have to align. We choose, as a simple proof of concept, to implement L3s cavities for both the CCW unit cavity as well as the high Q cavity. L3 is the representation of a defect line cavity of three missing holes, while the s denotes that the holes on the ends of the cavity are reduced in size. This size reduction enables the designer to sculpt the cavity resonance but is not considered variable for the current study. The CCW will be a chain of these cavities as defects in a triangular array of air hole circles of $r = 0.4a$ with 2 hole spacers ($r = 0.3a$) between each cavity as shown in Figure 14. The variable a is the lattice spacing of holes in the crystal.

In order to create the optical isolation necessary between the high- Q cavity and the CCW chain, barriers of variable index material will be used. These regions represent targets for optically induced refractive index switching using off resonant excitation [22].

3.3. Coupled Cavity Waveguide. Implementation of our PWE scheme with the above device shows that light will be nondispersive and therefore strongly confined along the M crystal direction but will exhibit dispersion and therefore propagate along the K crystal direction, as shown in Figure 15.

By orthogonalizing the k -vectors calculated in the PWE scheme so as to consider only the K direction, we may increment the PWE's eigenvalue calculations along only the direction of propagation to simulate the CCW structure's dispersion relation, shown in Figure 16.

The resulting spectral signature of this mode dispersion is shown in Figure 17 and will result in as many peaks over the range of resonant frequencies as there are coupled cavities in the chain.

Finally, it is important for the spatial field mode profiles of our cavity and CCW to be similar in order to maximize coupling between the two structures. Using both PWE and FDTD simulation methods, we verify the spatial field dependence shown in Figure 18 of our mode of choice.

3.4. Cavity. Relying on FDTD and the analysis of spectra, the design of our cavity is made through observation of the behavior of cavity resonance with changes to surrounding regions. First, an isolated L3s cavity is simulated to establish a basis for the types of modes this sort of cavity is likely to support. This sort of isolated defect is unable to be readily released into a CCW chain, and so a heterostructured cavity is implemented by including index-switchable regions to act as barriers to confine light away from the CCW portion of the device. Because the resonances of identical cavities shift in materials of different refractive index, shown in Figure 19, it is possible to use this resonance mismatch as a confining mechanism.

By implementing switched index cavities as barriers for the generation of a high- Q cavity, the mode of interest for both barrier-open (left) and barrier-closed (right) three cavity segments are shown in Figure 20. While the heterostructured cavity is greatly diminished in Q -factor when compared to a single well isolated L3 cavity, it still represents a functional and well-confined optical mode that

is effectively isolated from the neighboring CCW chain. With a Q-factor just under 2000, this proof of concept cavity represents an area for future research in optimization if strong coupling is desired.

Now, as we look toward coupling this cavity mode to the CCW chain, it should be noted that the cavity resonance of our isolated cavity is now centered to the CCW spectral feature. With these tools, the release and capture of an optical cavity mode is now outlined.

3.5. Implementing Coupling Mechanism. To perform release of the cavity mode into the CCW chain, one cavity barrier is index switched (opened) by optically induced carrier injection. Now matching the chain region, the cavity mode is allowed to couple to the CCW resonance and propagate from cavity to cavity down the chain. As the energy propagates down the chain, it becomes distributed amongst the coupled cavities and must be collected in a two step process by which the propagating mode is stopped by the outside secondary cavity barrier and allowed to accumulate before the inside secondary cavity barrier is activated, trapping the mode in the secondary heterostructured cavity. The full three step release and capture process is diagrammed here in Figure 21.

4. Results and Discussion

Through the switching protocol described above, transfer of energy from the optical mode in one high-Q cavity, through a chain of 5 coupled cavities, to a second high-Q cavity was achieved in a 2D FDTD scheme with 77% efficiency. Confinement at the first cavity, propagation between cavities, and capture in the second cavity is shown in Figure 22.

5. Conclusion

We have demonstrated that in theory using both a quantum model and a classical model that single photons can be transferred efficiently on-chip from a high-Q cavity to another using coupled cavity waveguides if the dynamic coupling between nearest neighbor cavities is carefully engineered. From the quantum model, as far as single-photon trapping and releasing mechanisms are concerned, dynamically switching coupling coefficients between “end” cavities and the waveguide yields much higher single photon transfer efficiencies (93% versus 75%) than dynamically switching the resonant frequencies of the “barrier” cavities. However, so far, only the single-photon trapping and releasing mechanism based on dynamically switching the resonant frequencies of the “barrier” cavities was able to be implemented in a practical way within our classical model. The endeavor to realize this system in a realistic form of a 3D photonic crystal slab (PCS) presents two hurdles: increased numerical cost, and out of plane loss mechanisms. It is expected that the increased numerical cost may be greatly alleviated by using 2D approximation methods for TE (even) polarization. However, due to the low group velocity of CCW modes and the zero group velocity of the high-Q state, careful engineering of the Fourier components of

the field distributions in this system will be necessary to avoid coupling to out-of-plane radiative modes. Until then, though, the two models shown in this work yield strikingly similar single-photon transfer efficiencies ($\sim 75\%$), which reinforces the versatility of CCWs and the advantage of using such structures to implement photonic quantum networks.

Acknowledgment

The authors acknowledge support from NSF ECCS-0725514.

References

- [1] B. B. Blinov, D. L. Moehring, L. M. Duan, and C. Monroe, “Observation of entanglement between a single trapped atom and a single photon,” *Nature*, vol. 428, no. 6979, pp. 153–157, 2004.
- [2] W. Yao, R. B. Liu, and L. J. Sham, “Theory of control of the spin-photon interface for quantum networks,” *Physical Review Letters*, vol. 95, no. 3, Article ID 030504, 4 pages, 2005.
- [3] W. Yao, R. B. Liu, and L. J. Sham, “Theory of control of the dynamics of the interface between stationary and flying qubits,” *Journal of Optics B*, vol. 7, no. 10, pp. S318–S325, 2005.
- [4] D. L. Moehring, M. J. Madsen, K. C. Younge et al., “Quantum networking with photons and trapped atoms (invited),” *Journal of the Optical Society of America B*, vol. 24, no. 2, pp. 300–315, 2007.
- [5] T. Wilk, S. C. Webster, A. Kuhn, and G. Rempe, “Single-atom single-photon quantum interface,” *Science*, vol. 317, no. 5837, pp. 488–490, 2007.
- [6] M. N. Leuenberger, M. E. Flatté, and D. D. Awschalom, “Teleportation of electronic many-qubit states encoded in the electron spin of quantum dots via single photons,” *Physical Review Letters*, vol. 94, no. 10, Article ID 107401, 2005.
- [7] A. A. Houck, D. I. Schuster, J. M. Gambetta et al., “Generating single microwave photons in a circuit,” *Nature*, vol. 449, no. 7160, pp. 328–331, 2007.
- [8] J. Majer, J. M. Chow, J. M. Gambetta et al., “Coupling superconducting qubits via a cavity bus,” *Nature*, vol. 449, no. 7161, pp. 443–447, 2007.
- [9] D. I. Schuster, A. A. Houck, J. A. Schreier et al., “Resolving photon number states in a superconducting circuit,” *Nature*, vol. 445, no. 7127, pp. 515–518, 2007.
- [10] M. A. Sillanpää, J. I. Park, and R. W. Simmonds, “Coherent quantum state storage and transfer between two phase qubits via a resonant cavity,” *Nature*, vol. 449, no. 7161, pp. 438–442, 2007.
- [11] D. England, A. Faraon, B. Zhang, Y. Yamamoto, and J. Vuckovic, “Generation and transfer of single photons on a photonic crystal chip,” *Optics Express*, vol. 15, no. 9, pp. 5550–5558, 2007.
- [12] J. Q. Liao, Z. R. Gong, L. Zhou, Y. X. Liu, C. P. Sun, and F. Nori, “Controlling the transport of single photons by tuning the frequency of either one or two cavities in an array of coupled cavities,” *Physical Review A*, vol. 81, no. 4, Article ID 042304, 2010.
- [13] P. Chak, J. E. Sipe, and S. Pereira, “Hamiltonian formulation for light propagation in waveguide-microresonator structures,” in *Proceedings of the Postconference on Quantum electronics and Laser Science (QELS '03)*, Trends in Optics and Photonics Series, pp. QTuL6/1–QTuL6/3, June 2003.

- [14] A. Adibi, R. K. Lee, Y. Xu, A. Yariv, and A. Scherer, "Design of photonic crystal optical waveguides with singlemode propagation in the photonic bandgap," *Electronics Letters*, vol. 36, no. 16, pp. 1376–1378, 2000.
- [15] M. Bayindir and E. Ozbay, "Heavy photons at coupled-cavity waveguide band edges in a three-dimensional photonic crystal," *Physical Review B*, vol. 62, no. 4, pp. R2247–R2250, 2000.
- [16] M. Bayindir, B. Temelkuran, and E. Ozbay, "Propagation of photons by hopping: a waveguiding mechanism through localized coupled cavities in three-dimensional photonic crystals," *Physical Review B*, vol. 61, no. 18, pp. R11855–R11858, 2000.
- [17] M. Bayindir, B. Temelkuran, and E. Ozbay, "Tight-binding description of the coupled defect modes in three-dimensional photonic crystals," *Physical Review Letters*, vol. 84, no. 10, pp. 2140–2143, 2000.
- [18] Y. Xu, R. K. Lee, and A. Yariv, "Propagation and second-harmonic generation of electromagnetic waves in a coupled-resonator optical waveguide," *Journal of the Optical Society of America B*, vol. 17, no. 3, pp. 387–400, 2000.
- [19] S. Mookherjee, "Dispersion characteristics of coupled-resonator optical waveguides," *Optics Letters*, vol. 30, no. 18, pp. 2406–2408, 2005.
- [20] H. P. Seigneur, G. Gonzalez, M. N. Leuenberger, and W. V. Schoenfeld, "Dynamics of entanglement between a quantum dot spin qubit and a photon qubit inside a semiconductor high-Q nanocavity," *Advances in Mathematical Physics*. In press.
- [21] D. Press, K. De Greve, P. L. McMahon et al., "Ultrafast optical spin echo in a single quantum dot," *Nature Photonics*, vol. 4, pp. 367–370, 2010.
- [22] Y. Tanaka, J. Upham, T. Nagashima, T. Sugiya, T. Asano, and S. Noda, "Dynamic control of the Q factor in a photonic crystal nanocavity," *Nature Materials*, vol. 6, no. 11, pp. 862–865, 2007.
- [23] S. F. Preble, Q. Xu, and M. Lipson, "Changing the colour of light in a silicon resonator," *Nature Photonics*, vol. 1, no. 5, pp. 293–296, 2007.
- [24] P. O. Dong, L. Chen, Q. Xu, and M. Lipson, "On-chip generation of high-intensity short optical pulses using dynamic microcavities," *Optics Letters*, vol. 34, no. 15, pp. 2315–2317, 2009.
- [25] T. Tanabe, M. Notomi, H. Taniyama, and E. Kuramochi, "Dynamic release of trapped light from an ultrahigh-Q nanocavity via adiabatic frequency tuning," *Physical Review Letters*, vol. 102, no. 4, Article ID 043907, 2009.
- [26] F. Y. Gardes, G. T. Reed, N. G. Emerson, and C. E. Png, "A sub-micron depletion-type photonic modulator in silicon on insulator," *Optics Express*, vol. 13, no. 22, pp. 8845–8854, 2005.
- [27] T. J. Karle, Y. J. Chai, C. N. Morgan, I. H. White, and T. F. Krauss, "Observation of pulse compression in photonic crystal coupled cavity waveguides," *Journal of Lightwave Technology*, vol. 22, no. 2, pp. 514–519, 2004.
- [28] J. Hou, H. Wu, D. S. Citrin, W. Mo, D. Gao, and Z. Zhou, "Wideband slow light in chirped slot photonic crystal coupled waveguides," *Optics Express*, vol. 18, no. 10, pp. 10567–10580, 2010.
- [29] D. O'Brien, M. D. Settle, T. Karle, A. Michaeli, M. Salib, and T. F. Krauss, "Coupled photonic crystal heterostructure nanocavities," *Optics Express*, vol. 15, no. 3, pp. 1228–1233, 2007.
- [30] J. Jagerska, N. Le Thomas, V. Zabelin et al., "Experimental observation of slow mode dispersion in photonic crystal coupled-cavity waveguides," *Optics Letters*, vol. 34, no. 3, pp. 359–361, 2009.
- [31] A. Faraon, E. Waks, D. Englund, I. Fushman, and J. Vuckovic, "Efficient photonic crystal cavity-waveguide couplers," *Applied Physics Letters*, vol. 90, no. 7, Article ID 073102, 2007.
- [32] P. Yao and S. Hughes, "Controlled cavity QED and single-photon emission using a photonic-crystal waveguide cavity system," *Physical Review B*, vol. 80, no. 16, Article ID 165128, 2009.
- [33] Y. Huang and Y. W. Lu, "A defect effect to light transmission through acute bending coupled cavity waveguide in a two-dimensional photonic crystal," *Chinese Physics Letters*, vol. 26, no. 4, Article ID 047805, 2009.
- [34] E. Ozbay, M. Bayindir, I. Bulu, and E. Cubukcu, "Investigation of localized coupled-cavity modes in two-dimensional photonic bandgap structures," *IEEE Journal of Quantum Electronics*, vol. 38, no. 7, pp. 837–843, 2002.
- [35] Y. Wang, T. Wang, and J. Liu, "Waveguide modes in coupled-resonator optical waveguides," *Physics Letters A*, vol. 353, no. 1, pp. 101–104, 2006.

Research Article

Ultrabroadband Electro-Optic Modulator Based on Hybrid Silicon-Polymer Dual Vertical Slot Waveguide

Shouyuan Shi and Dennis W. Prather

Department of Electrical and Computer Engineering, University of Delaware, 140 Evans Hall, Newark, DE 19716, USA

Correspondence should be addressed to Shouyuan Shi, sshi@ee.udel.edu

Received 15 May 2010; Accepted 30 July 2010

Academic Editor: Ana Vukovic

Copyright © 2011 S. Shi and D. W. Prather. This is an open access article distributed under the Creative Commons Attribution License, which permits unrestricted use, distribution, and reproduction in any medium, provided the original work is properly cited.

We present a novel hybrid silicon-polymer dual slot waveguide for high speed and ultra-low driving voltage electro-optic (EO) modulation. The proposed design utilizes the unique properties of ferroelectric materials such as LiNbO_3 to achieve dual RF and optical modes within a low index nanoslot. The tight mode concentration and overlap in the slot allow the infiltrated organic EO polymers to experience enhanced nonlinear interaction with the applied electric field. Half-wavelength voltage-length product and electro-optic response are rigorously simulated to characterize the proposed design, which reveals ultrabroadband operation, up to 250 GHz, and subvolt driving voltage for a 1 cm long modulator.

1. Introduction

Low driving voltage and high-speed electro-optic (EO) modulators are of great interest due to their wide variety of applications including broadband communication, RF photonic links, millimeter wave imaging, and phased-array radars. In order to attain optical modulation at low driving voltages, a strong mode concentration and a tight mode overlap between optical and radio-frequency (RF) modes in the nonlinear EO material are required. Typically, to maintain a single mode operation in optical domain, the optical mode size is on an order of wavelength, that is, 2 μm at telecommunication region. As a result, to match with the optical mode, the RF guiding structure essentially has to reduce a factor of three orders of magnitude. Conventional traveling wave EO modulators are usually driven by RF transmission lines, such as coplanar waveguides (CPWs) and microstrip lines. These electrode designs provide not only high speed operation but also a strong overlap between optical and RF modes. While the device operates at very high frequency, that is, over 20 GHz, the RF wave propagation attenuation attributed from both conduction loss and dielectric loss becomes the key issue that prevents the device from operating over a wide bandwidth. Physically, a small mode size provides a strong RF field concentration, or a small mode volume, however,

leads to a significant increase in propagation loss. As a result, an optimal design of RF electrode design including signal electrode and gap between signal and ground is required to minimize the overall RF propagation loss.

To date, many high speed traveling wave EO modulators have been designed, fabricated, and characterized, leading to operation at speeds as high as 140 GHz. Most of these modulators were developed using crystalline EO materials, such as LiNbO_3 [1–5] and GaAs [6, 7]. Recently, tremendous efforts have gone into the development and optimization of organic EO polymers. State-of-the-art nonlinear electro-optic polymers have been reported to have an EO coefficient of $r_{33} = 100 \text{ pm/V}$ or higher [8–14], which is nearly an order of magnitude higher than the crystalline LiNbO_3 and two orders of magnitude higher than most III-V materials. With the recent breakthroughs in silicon photonics, specifically vertical and horizontal slot waveguides [15, 16], the silicon organic hybrid represents a tremendous opportunity to develop highly sensitive devices for an array of photonics applications [17–20]. A variety of designs including ridged slot waveguides and segmented slot waveguides have been proposed for modulation applications [21–24]. By placing low index EO polymer material in the slot region, the optical mode will be tightly confined in the nonlinear material. This requires an extremely small RF mode concentration

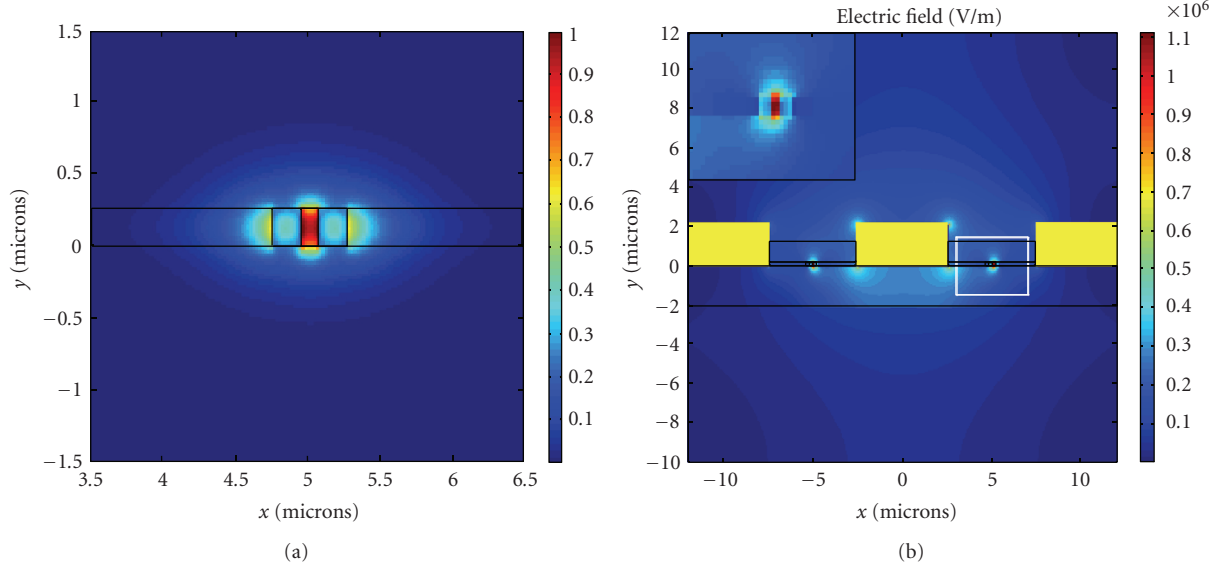


FIGURE 2: Optical and RF mode profiles. (a) Optical electric field distribution at a wavelength of 1.55 μm . (b) RF electric field distribution at a frequency of 100 GHz with 1 V applied between the signal electrode and ground. The colorbar scale confirms the field concentration near 1.1 MV/m within the low index EO polymer infiltrated slot. The dashed box indicates the position of the optical mode as shown in (a).

First, consider a quasitransverse electric (TE) mode in the optical domain, where the dominant electric field component is parallel to the horizontal plane, as shown in Figure 1. The electromagnetic boundary conditions reveal the electric field discontinuity across the slot, thereby resulting in an enhancement in the electric field strength in the low index material [15]. In order to characterize optical confinement within the polymer material, the confinement factor is defined as the ratio of the propagation power inside the slot to the total power of the guiding mode, $\Gamma_o = \int_{\text{Slot}} \text{Re}(\mathbf{E} \times \mathbf{H}) ds / \int_{\text{Waveguide}} \text{Re}(\mathbf{E} \times \mathbf{H}) ds$. The figure of merit, Γ_o , is strongly dependent on the design parameters, such as waveguide height, slot width, and silicon ridge width. Therefore, optimization of the design parameters is required to maximize mode confinement factor to achieve an improved EO modulation.

A full-vectorial finite-difference (FD) analysis [26] that is capable of handling anisotropic and lossy material properties is developed and employed to simulate the waveguiding characteristics, that is, the guided mode and effective index. We consider a slot waveguide with a gap size of $w_p = 120$ nm and a silicon ridge width of $w_{si} = 250$ nm. The EO polymer has a total height of $h_p = 1.2 \mu\text{m}$. Figure 2(a) shows the optical electric field distribution at the wavelength of 1.55 μm with an effective index of 2.027. Across the middle plane of the waveguide structure an enhancement of $(n_{si}/n_p)^2 = 4.7$ in the electric field can be observed. Based on the mode profile, the calculated optical confinement factor in the EO polymer is $\Gamma_o = 36.56\%$. The large mode concentration in the nanoslot provides an opportunity for the enhanced nonlinear interaction with applied electric field. As shown in Figure 2(a), the further extension of optical mode into top cladding of EO polymer and edge cladding of LiNbO₃ will lead to an improved EO modulation.

The strong optical mode confinement in the slot suggests a RF mode overlap in the slot to maximize the modulation. Due to the very extremely different wavelength scales between RF and optical waves, the design for RF mode in a nanometer-scale slot becomes extremely challenging. Efforts have been made to establish the electrical field in the vertical slot by highly doping the silicon. However, at high frequencies the doped silicon becomes extremely lossy rather than conductive, thereby prohibiting its high speed operation. With the application of LiNbO₃ as the outer claddings, let's also concern with concentrating the RF signal. While an RF signal is applied to the CPW electrodes, a CPW mode is established in which the dominant electric field in the gap between signal and ground is aligned in the x direction. Since LiNbO₃ material has a much larger dielectric constant than the silicon and EO polymer materials, the boundary conditions reveal that the resultant RF electric field inside the ferroelectric and silicon materials is much weaker than within the EO polymer. The weak electric field in the high dielectric constant materials indicates a small fraction of voltage drop across the materials; as a result, a large portion of the applied voltage is directly across the slot. The resulting structure creates an effective RF nanoslot waveguide within the transmission line. Due to the strong mode confinement in the low index EO polymer infiltrated slot, a lower overall RF effective index can be achieved. In the proposed design, the signal electrode width is $w_m = 8 \mu\text{m}$ and the CPW gap size is $w_{\text{gap}} = 6 \mu\text{m}$. The electrode thickness, h_m , is optimized to match the RF effective index with that of the optical mode, enabling high speed operation. The loss tangents of LiNbO₃ and silicon are 0.004 and 0.002, respectively, and the conductivity of gold is 4.1×10^7 S/m. As shown in Figure 2(a), a strong electric field confinement, over 1.1×10^6 V/m, is observed when a voltage of 1 V is applied across the signal

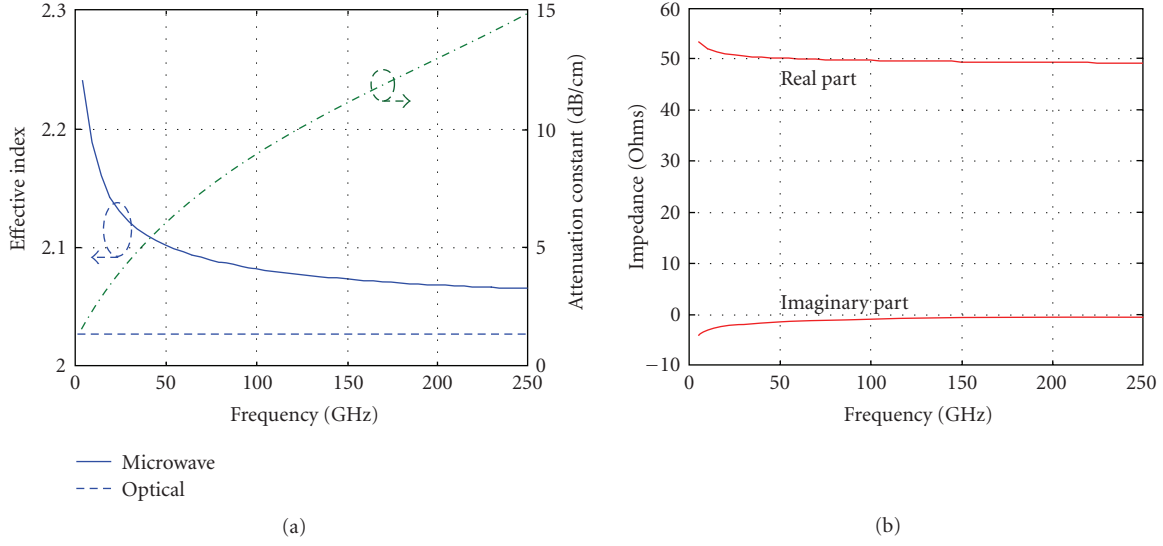


FIGURE 3: RF propagation characteristics of dual slot waveguide. (a) RF and optical effective indices and RF attenuation constant over the frequencies of 250 GHz. The dashed blue line indicates the effective optical index of 2.502. (b) Characteristic impedance.

electrode and ground at a frequency of 100 GHz. Such a strong electric field concentration will induce a significant optical index change in the nonlinear EO polymer material, resulting in a deep optical modulation. An ultrabroadband response that spans from DC to 250 GHz is performed by HFSS.

On the other hand, the introduction of the high dielectric constant material potentially allows for an increased electrode separation between signal and ground without significantly decreasing the electric field confinement in the slot. As a result, the RF mode will experience reduced conduction loss. This becomes of particular importance for the modulators to operate at high frequencies. Figure 3(a) shows the comparison between the optical effective index and frequency dependent RF effective index, as well as the attenuation constant for the RF slot waveguide. An optimal electrode thickness, $h_m = 2.2 \mu\text{m}$, is found to minimize the index mismatch to a value as low as 0.038 at high frequencies. Due to tight concentration in the slot, the overall RF effective does not vary significantly, and tends to be convergent to 2.065 at the frequencies over 50 GHz. Figure 3(b) shows the real and imaginary parts of the characteristic impedance. The finite conductivity has a strong impact on the characteristic impedance. At frequencies over 50 GHz, the characteristic impedance remains to be 49 Ohms.

3. Electro-Optic Modulation Analysis

In order to characterize the high speed electro-optic response and sensitivity of the proposed device based on the simulated optical and RF guided mode characteristics in the previous section, consider a traveling wave electro-optic modulator, where both optical and RF guided modes are copropagated along the same direction over a length of L . The RF voltage

amplitude along the transmission line can be expressed as [4, 27]

$$V(f_m, y) = V_0 e^{-\alpha_m(f_m)y} e^{j(k_m \delta y - 2\pi f_m t_0)}, \quad (1)$$

where V_0 is the amplitude of the RF wave at the input port, $k_m = 2\pi n_m / \lambda_m$ is the RF wave number, α_m is the RF attenuation constant, $\delta = 1 - n_o / n_m$ is the relative index mismatch between RF effective index n_m and optical effective index n_o , and f_m is the RF frequency. Driven by the microwave, the optical phase induced at the end of modulator is derived by integrating the induced phase over the modulator, given by

$$\Delta\phi(f_m) = \int_0^L \frac{2\pi}{\lambda_o} \Gamma V_0 e^{-\alpha_m(f_m)y} e^{j(k_m \delta y - 2\pi f_m t_0)} dy, \quad (2)$$

where the mode overlap integral factor, Γ , that characterizes the induced changes in refractive index for a given applied voltage of V_0 , is defined by the mode overlap integral between optical and RF electric fields in the cross section transversal to the modulator propagation direction,

$$\Gamma = \frac{1}{V_0} \frac{\iint_S (1/2) n_{\text{eff}}^3 r_{33}(x, z) E_m(x, z) |E_o(x, z)|^2 ds}{\iint_S |E_o(x, z)|^2 ds}, \quad (3)$$

where n_{eff} is the effective index of the optical mode, r_{33} is the EO coefficient distribution, and E_m and E_o are the RF and optical electric fields, respectively. To characterize the high-speed response of the modulator, the electro-optic response of the modulator, derived from the induced phase at a given

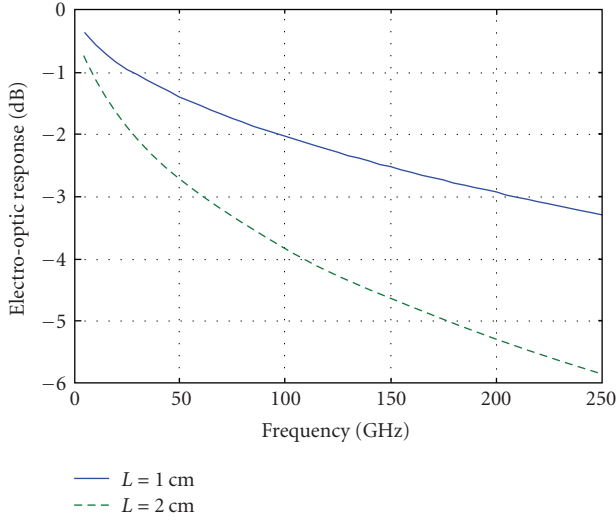


FIGURE 4: Electro-optical response of the proposed modulators with different modulator lengths of 1 and 2 cm.

TABLE 1: DC half-wavelength length-product.

r_{33} (pm/V)	DC $V_{\pi}L$ (mV·cm)
30	675.8
100	215.5
170	128.2

RF frequency of f_m , is defined as a normalized quantity compared to the phase change at DC,

$$m(f_m) = \frac{|\Delta\phi(f_m)|}{|\Delta\phi(0)|} = e^{-\alpha_m(f_m)L/2} \sqrt{\frac{\sinh^2(\alpha_m L/2) + \sin^2(k_m \delta L/2)}{(\alpha_m L/2)^2 + (k_m \delta L/2)^2}}. \quad (4)$$

From the above equation, the electro-optic response is strongly dependent on the RF loss coefficient and index matching, or velocity matching, between optical and RF guided modes. The half-wavelength voltage of $V_{\pi}(f_m)$ corresponding to a phase change of π over the interaction length of L to produce a zero optical output can be derived as,

$$V_{\pi}(f_m) = \frac{V_{\pi}(\text{DC})}{m(f_m)}, \quad (5)$$

where DC half-wavelength voltage is given by the $V_{\pi}(\text{DC}) = \lambda_o/2\Gamma L$. The longer the length of the modulator is, the lower the DC V_{π} is; however, the lower the EO response is due to RF loss. Therefore, there is an optimal length for achieving a minimum half-wavelength voltage at high frequency.

From the analysis of both RF and optical characteristics in the previous section, the electro-optic modulation can be characterized based on the DC half-wavelength voltage-

length product and the electro-optic response. The DC half-wavelength voltage-length product is strongly dependent on the mode overlap integral factor, Γ , that is inherently related to the RF and optical mode concentration and overlap, as well as the EO coefficients. To evaluate these expressions, the EO coefficient of the EO polymer is assumed to be $r_{33} = 30, 100$, or 170 pm/V [8, 11, 22, 28]. The resulting $V_{\pi}L$ is listed accordingly in Table 1, indicating nearly two orders of magnitude enhancement in EO modulation compared to traditional LiNbO₃ traveling wave modulators. Figure 4 depicts the EO response of the proposed modulators with two different lengths: $L = 1$ and 2 cm, obtained from (4). Minimal RF propagation loss and good index matching provide an ultrabroadband electro-optic response, that is, 250 GHz. The frequency-dependent driving voltage, derived from the DC $V_{\pi}L$ and electro-optic response $m(f_m)$, demonstrates a subvolt driving voltage, at ultra-high frequencies. The push-pull configuration of the modulator will further reduce the DC V_{π} by a factor of 2 if an intensity modulation is interested.

Compared to conventional traveling wave modulators, the proposed dual vertical slot waveguide EO modulators demonstrate superior advantages from a variety of aspects. The extremely strong RF and optical modes confinement within a nanoslot lead to a tight mode overlap, enhancing nonlinear interaction of EO polymer. The reduced RF loss due to a large electrode gap improves the electro-optic response, thereby enabling high speed operation. The application of exotic organic EO polymer owing to its high EO coefficient further lower the driving voltage, therefore enhancing sensitivity. In addition to these, the application of EO property of polymer requires careful material preparation, including EO activation. In order to activate the EO property, EO polymer is required to pole at an appropriate temperature with an extremely high field, that is, $50 \text{ V}/\mu\text{m}$ [22]. The proposed design may offer potential in the EO material poling process. An applied DC bias on the electrodes can be directly extended across the slot. For a given 120-nm slot and 40-V applied voltage, an electric field about $44 \text{ V}/\mu\text{m}$ can be produced. The small slot size and the strong field established with a low applied voltage make an in situ poling process of the polymer feasible.

4. Conclusion

In summary, we have presented an integrated RF and optical vertical dual slot waveguide traveling wave EO modulator. By harnessing the unique material properties of the ferroelectric LiNbO₃ material and organic EO polymers, the proposed design is able to tightly concentrate both RF and optical modes in a slot for maximizing the nonlinear interaction with the applied electric field. Numerical simulations are performed to characterize the design. The tight mode overlap and large EO coefficient of polymer significantly leverage the modulation sensitivity, leading to a subvolt driving voltage over a length of 1 cm. The improved electrode design significantly reduce the RF propagation attenuation, thereby enabling the design operate over the frequencies of 250 GHz.

Acknowledgments

The authors gratefully acknowledge Drs. Attila Szep, Robert Nelson, and Gernot Pomrenke from Air Force Research Lab for the valuable discussions and financial support for this research.

References

- [1] J. Macario, P. Yao, R. Shireen, C. A. Schuetz, S. Y. Shi, and D. W. Prather, "Development of electro-optic phase modulator for 94 GHz imaging system," *Journal of Lightwave Technology*, vol. 27, pp. 5698–5703, 2009.
- [2] K. Noguchi, O. Mitomi, and H. Miyazawa, "Millimeter-wave TiLiNbO_3 optical modulators," *Journal of Lightwave Technology*, vol. 16, no. 4, pp. 615–619, 1998.
- [3] Y. Liao, H. Zhou, and Z. Meng, "Modulation efficiency of a LiNbO_3 waveguide electro-optic intensity modulator operating at high microwave frequency," *Optics Letters*, vol. 34, no. 12, pp. 1822–1824, 2009.
- [4] Y.-Q. Lu, M. Xiao, and G. J. Salamo, "Wide-bandwidth high-frequency electro-optic modulator based on periodically poled LiNbO_3 ," *Applied Physics Letters*, vol. 78, no. 8, pp. 1035–1037, 2001.
- [5] D. Janner, M. Belmonte, and V. Pruneri, "Tailoring the electrooptic response and improving the performance of integrated LiNbO_3 modulators by domain engineering," *Journal of Lightwave Technology*, vol. 25, no. 9, pp. 2402–2409, 2007.
- [6] Q. Y. Lu, W. H. Guo, D. Byrne, and J. F. Donegan, "Design of low V- π high-speed GaAs travelling-wave electrooptic phase modulators using an n-i-p-n structure," *IEEE Photonics Technology Letters*, vol. 20, pp. 1805–1807, 2008.
- [7] M. Jarrahi, T. H. Lee, and D. A.B. Miller, "Wideband, low driving voltage traveling-wave Mach-Zehnder modulator for RF photonics," *IEEE Photonics Technology Letters*, vol. 20, no. 7, pp. 517–519, 2008.
- [8] Y. Enami, C. T. Derose, D. Mathine et al., "Hybrid polymersol-gel waveguide modulators with exceptionally large electro-optic coefficients," *Nature Photonics*, vol. 1, no. 3, pp. 180–185, 2007.
- [9] Y. Enami, D. Mathine, C. T. Derose et al., "Hybrid cross-linkable polymer/sol-gel waveguide modulators with 0.65 V half wave voltage at 1550 nm," *Applied Physics Letters*, vol. 91, no. 9, Article ID 093505, 3 pages, 2007.
- [10] M. Lee, H. E. Katz, C. Erben et al., "Broadband modulation of light by using an electro-optic polymer," *Science*, vol. 298, no. 5597, pp. 1401–1403, 2002.
- [11] C. T. DeRose, D. Mathine, Y. Enami et al., "Electrooptic polymer modulator with single-mode to multimode waveguide transitions," *IEEE Photonics Technology Letters*, vol. 20, no. 12, pp. 1051–1053, 2008.
- [12] E. M. McKenna, A. S. Lin, A. R. Mickelson, R. Dinu, and D. Jin, "Comparison of r_{33} values for AJ404 films prepared with parallel plate and corona poling," *Journal of the Optical Society of America B*, vol. 24, no. 11, pp. 2888–2892, 2007.
- [13] T. Gorman, S. Haxha, and J. J. Ju, "Ultra-high-speed deeply etched electrooptic polymer modulator with profiled cross section," *Journal of Lightwave Technology*, vol. 27, no. 1, pp. 68–76, 2009.
- [14] L. R. Dalton, P. A. Sullivan, and D. H. Bale, "Electric field poled organic electro-optic materials: state of the art and future prospects," *Chemical Reviews*, vol. 110, no. 1, pp. 25–55, 2010.
- [15] V. R. Almeida, Q. Xu, C. A. Barrios, and M. Lipson, "Guiding and confining light in void nanostructure," *Optics Letters*, vol. 29, no. 11, pp. 1209–1211, 2004.
- [16] R. Sun, P. Dong, N.-N. Feng et al., "Horizontal single and multiple slot waveguides: optical transmission at $\lambda = 1550$ nm," *Optics Express*, vol. 15, no. 26, pp. 17967–17972, 2007.
- [17] C. Koos, P. Vorreau, T. Vallaitis et al., "All-optical high-speed signal processing with silicon-organic hybrid slot waveguides," *Nature Photonics*, vol. 3, no. 4, pp. 216–219, 2009.
- [18] F. Dell'Olio and V. M. N. Passaro, "Optical sensing by optimized silicon slot waveguides," *Optics Express*, vol. 15, no. 8, pp. 4977–4993, 2007.
- [19] J.-M. Brosi, C. Koos, L. C. Andreani, M. Waldow, J. Leuthold, and W. Freude, "High-speed low-voltage electro-optic modulator with a polymer-infiltrated silicon photonic crystal waveguide," *Optics Express*, vol. 16, no. 6, pp. 4177–4191, 2008.
- [20] C. A. Barrios, "Ultrasensitive nanomechanical photonic sensor based on horizontal slot-waveguide resonator," *IEEE Photonics Technology Letters*, vol. 18, no. 22, pp. 2419–2421, 2006.
- [21] G. Wang, T. Baehr-Jones, M. Hochberg, and A. Scherer, "Design and fabrication of segmented, slotted waveguides for electro-optic modulation," *Applied Physics Letters*, vol. 91, no. 14, 2007.
- [22] T. Baehr-Jones, B. Penkov, J. Huang et al., "Nonlinear polymer-clad silicon slot waveguide modulator with a half wave voltage of 0.25 V," *Applied Physics Letters*, vol. 92, no. 16, Article ID 163303, 2008.
- [23] M. Hochberg, T. Baehr-Jones, G. Wang et al., "Towards a millivolt optical modulator with nano-slot waveguides," *Optics Express*, vol. 15, no. 13, pp. 8401–8410, 2007.
- [24] K. K. McLauchlan and S. T. Dunham, "Analysis of a compact modulator incorporating a hybrid silicon/electro-optic polymer waveguide," *IEEE Journal on Selected Topics in Quantum Electronics*, vol. 12, no. 6, pp. 1455–1460, 2006.
- [25] S. Shi and D. W. Prather, "Dual rf-optical slot waveguide for ultrabroadband modulation with a subvolt V_p ," *Applied Physics Letters*, vol. 96, Article ID 201107, 2010.
- [26] Z. Zhu and T. G. Brown, "Full-vectorial finite-difference analysis of microstructured optical fibers," *Optics Express*, vol. 10, no. 17, pp. 853–864, 2002.
- [27] R. C. Alferness, "Waveguide electrooptic modulators," *IEEE Transactions on Microwave Theory and Techniques*, vol. 30, no. 8, pp. 1121–1137, 1982.
- [28] S.-K. Kim, Y.-C. Hung, W. Yuan et al., "Metal-slotted polymer optical waveguide device," *Applied Physics Letters*, vol. 90, no. 24, Article ID 243507, 3 pages, 2007.

Research Article

Microcavity Silicon Photodetectors at 1.55 μm

M. Casalino,¹ G. Coppola,¹ M. Giofrè,¹ M. Iodice,¹ L. Moretti,² I. Rendina,¹ and L. Sirleto¹

¹ Department of Naples, Institute for Microelectronics and Microsystems, National Council of Research, Via P. Castellino 111, 80131 Naples, Italy

² Department of Mathematics, Seconda Università degli Studi di Napoli, Via Vivaldi 43, 81100 Caserta, Italy

Correspondence should be addressed to M. Casalino, maurizio.casalino@na.imm.cnr.it

Received 25 June 2010; Revised 16 September 2010; Accepted 22 October 2010

Academic Editor: Snjezana Tomljenovic-Hanic

Copyright © 2011 M. Casalino et al. This is an open access article distributed under the Creative Commons Attribution License, which permits unrestricted use, distribution, and reproduction in any medium, provided the original work is properly cited.

The design, the realization, and the characterization of silicon resonant cavity enhanced (RCE) photodetectors, working at 1.55 μm , are reported. The photodetectors are constituted by a Fabry-Perot microcavity incorporating a Schottky diode. The working principle is based on the internal photoemission effect. We investigated two types of structures: top and back-illuminated. Concerning the top-illuminated photodetectors, a theoretical and numerical analysis has been provided and the device quantum efficiency has been calculated. Moreover, a comparison among three different photodetectors, having as Schottky metal: gold, silver, or copper, was proposed. Concerning the back-illuminated devices, two kinds of Cu/p-Si RCE photodetectors, having various bottom-mirror reflectivities, were realized and characterized. Device performances in terms of responsivity, free spectral range, and finesse were theoretically and experimentally calculated in order to prove an enhancement in efficiency due to the cavity effect. The back-illuminated device fabrication process is completely compatible with the standard silicon technology.

1. Introduction

In the last two decades, there has been growing interest in photonic devices based on Si-compatible materials [1, 2] in the field of both optical telecommunications and optical interconnects. In this context, tremendous progresses in the technological processes have allowed to realize effectively fully CMOS compatible optical components, such as low-loss waveguides, high-Q resonators, high speed modulators, couplers, and optically pumped lasers [3–8]. All these devices have been developed to operate in the wavelength range from the C optical band (1528–1561 nm) to the L optical band (1561–1620 nm) where the defect-free intrinsic bulk Si has minimal absorption. On the other hands, this transparency window limits the Si applications as absorbing material for infrared photodetection, so that the development of high-performance waveguide-integrated photodetectors on Si-CMOS platform has remained an imperative but unaccomplished task. In order to develop all Si photodetectors and to take advantage of the low-cost standard Si-CMOS processing technology without additional materials or process steps, a number of options have been proposed, in particular, the two-photon absorption (TPA) [9], the incorporation of

optical dopants/defects with mid-bandgap energy levels into the Si lattice [10, 11], and the internal photoemission effect (IPE) [12]. The IPE has been recently used also in silicon photodetectors realized with plasmonics structures [13, 14].

Silicon infrared photodiodes based on the IPE are usually employed in infrared imaging systems [15]. Unfortunately, due to their low potential barriers (≤ 0.25 eV), they must work at cryogenic temperature (70 K) in order to avoid high dark-current densities. The main advantages of these devices reside in their large bandwidth and simple fabrication process, but, due to the leakage photon flux within the metallic layer, their quantum efficiency (number of collected electrons per incident photon) is very small. In this paper, with the aim to enhance the device quantum efficiency at room temperature, top- and back-illuminated photodetectors at 1.55 μm , based on IPE and incorporated into a microcavity structure, have been investigated. A theoretical and numerical analysis of a top-illuminated structure has been provided, and in order to estimate the device theoretical quantum efficiency, we have taken advantage of the analytical formulation of the Fowler's theory [16], including the image force effect and its extension for thin films. On the other

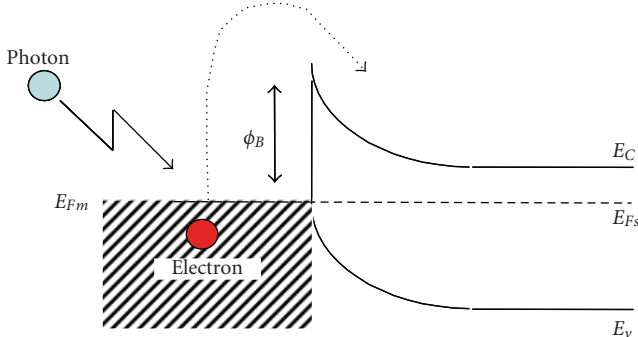


FIGURE 1: Energy band diagram for a metal-semiconductor junction.

hand, concerning the device optical analysis, a numerical approach, based on the transfer matrix method (TMM), has been implemented. We prove that a significant enhancement in quantum efficiency can be achieved by using an RCE structure. A comparison among three different Schottky barrier silicon photodetectors, having as metal layers: gold, silver, and copper, has been proposed. Our numerical results prove that in order to improve the device quantum efficiency, the Schottky barrier plays a key role.

However, concerning the top-illuminated structure, the crucial point is the realization of a metal thin film (semitransparent). The precise control of the thin metal

thickness and an acceptably low defect concentration are not trivial tasks. Therefore, the design, the realization, and the characterization of back-illuminated RCE photodetectors having a thick metal layer as top mirror, have been reported. In order to experimentally prove the responsivity (ratio between photogenerated current and incident optical power) enhancement, which can be achieved by using a resonant structure, a comparison between a Schottky diode, with and without Bragg reflector, has been made. An improvement in responsivity at $1.55 \mu\text{m}$ has been theoretically and experimentally demonstrated for the Cu/p-Si Schottky diode provided by a high reflectivity Bragg mirror.

2. Internal Photoemission Theory

Internal photoemission is the optical excitation of electrons in the metal to an energy above the Schottky barrier and then transport of these electrons to the conduction band of the semiconductor (Figure 1).

The standard theory of the photoemission from a metal into the vacuum is due to Fowler [16]. In a gas of electrons obeying the Fermi-Dirac statistics, if the energy of the incoming photons is close to the potential barrier ($h\nu \approx \Phi_B$), the fraction (F_e) of the absorbed photons, which produce photoelectrons with the appropriate energy and moment before scattering to contribute to the photocurrent, is given by

$$F_e = \frac{[(h\nu - (\phi_{B0} - \Delta\phi_B))^2 + (kT\pi)^2/3] - 2(kT)^2 e^{-h\nu - ((\phi_{B0} - \Delta\phi_B))/kT}}{8kTE_F \log[1 + e^{(h\nu - (\phi_{B0} - \Delta\phi_B))/kT}]}, \quad (1)$$

where $h\nu$ is photon's energy, Φ_{B0} is the potential barrier at zero bias, $\Delta\phi_B$ is the lowering due to the image force effect (as we will see later), and E_F is the metal Fermi level. As it is possible to see in (1), F_e is strongly depending on the potential barrier height of the metal-semiconductor interface.

In order to study the quantum efficiency for thin metal films, the theory must be further extended, taking into account multiple reflections of the excited electrons from the surface of the metals film, in addition to the collisions with phonons, imperfections, and cold electrons. Assuming a thin metal film, a phenomenological, semiclassical, ballistic transport model for the effects of the scattering mechanisms resulting in a multiplicative factor for quantum efficiency was developed by Vickers [17]. According to this model, the accumulated probability P_E that the electrons will have sufficient normal kinetic energy to overcome the potential barrier is given by

$$P_E \cong [1 - e^{-(d/L_e)}]^{1/2}, \quad (2)$$

where d is the metal thickness and L_e is the mean free path.

In order to complete the internal photoemission theory, the image force between an electron and the metal surface must be taken into account. The image force effect causes a lowering ($\Delta\phi_B$) and displacement (x_m) of the metal-semiconductor interface potential barrier. These barrier lowering and displacement are given by [18]

$$x_m = \sqrt{\frac{q}{16\pi\epsilon_{Si}} \frac{W}{|V_{Bias}|}}, \quad \Delta\phi_B = \sqrt{\frac{q}{4\pi\epsilon_{Si}} \frac{|V_{Bias}|}{W}}, \quad (3)$$

where ϵ_{Si} is the permittivity of silicon (10^{-12} C/cmV), W is the depletion width, and V_{Bias} the applied bias voltage.

Finally, the probability that an electron travels from the metal-semiconductor interface to the Schottky barrier maximum without scattering in the Si is taken into account by the barrier collection efficiency η_c , which is given by [19]

$$\eta_c = e^{-(x_m/L_s)}, \quad (4)$$

where L_s is the electron scattering length in the silicon. It is worth noting that by increasing the bias voltage, a shift of Schottky barrier closer to metal-semiconductor interface is obtained. Therefore, the barrier collection efficiency increases.

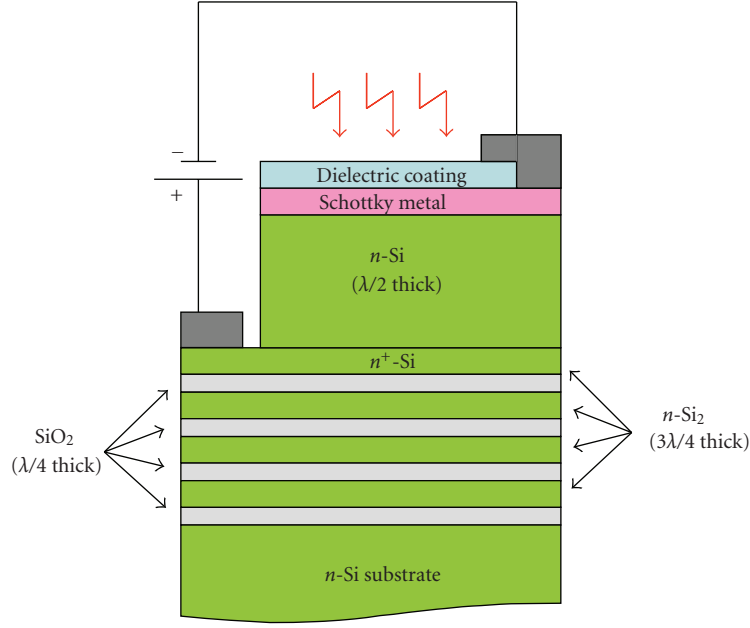


FIGURE 2: Schematic cross-section of top-illuminated RCE Schottky photodetector.

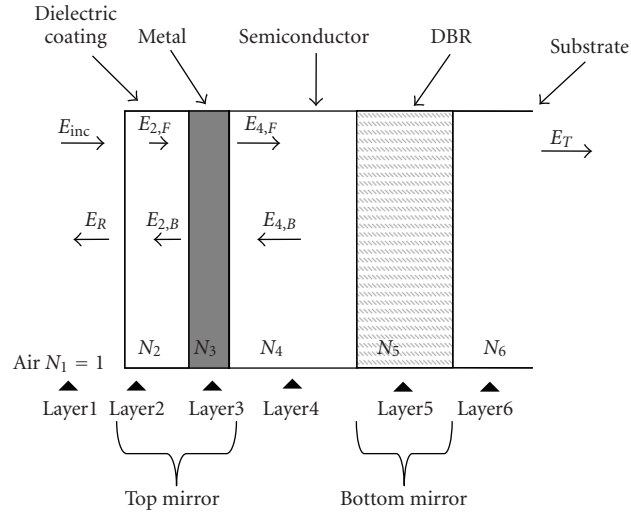


FIGURE 3: Schematic of the multilayer RCE photodetector.

3. Top-Illuminated Device

3.1. Proposed Device. The sketch of the proposed top-illuminated photodetector is shown in Figure 2.

The resonant cavity is a Fabry-Perot surface normal structure. It is formed by a buried reflector, a metallic top mirror, and, in the middle, a $\lambda/2$ silicon cavity. On top of the $\lambda/2$ silicon cavity has been deposited a semitransparent Schottky metal and a coating dielectric layer, working as top reflector of the resonant cavity. We point out that our structure is different from the RCE Schottky photodetectors in which the Schottky contact is only an electric contact and not the active layer. In our device, the metal layer works as

top contact, as active (absorbing) layer, and as mirror. This is the crucial point and the novelty of our device.

The distributed Bragg reflector (DBR) could be formed by alternate layers of Si and SiO₂ having refractive indices 3.45 and 1.45, respectively. One of the many benefits of this reflector is the large index contrast provided by Si/SiO₂ structures allowing the realization of high-reflectivity and wide spectral stop-band DBR. Commercially reproducible dielectric mirrors consisting of a two-period DBR fabricated using a double silicon-on-insulator (DSOI) process have been successfully realized showing a reflectivity of 92.7% at 1550 nm [20, 21]. In the same way, it could be possible to realize DBR formed of more than two Si/SiO₂ pairs. The

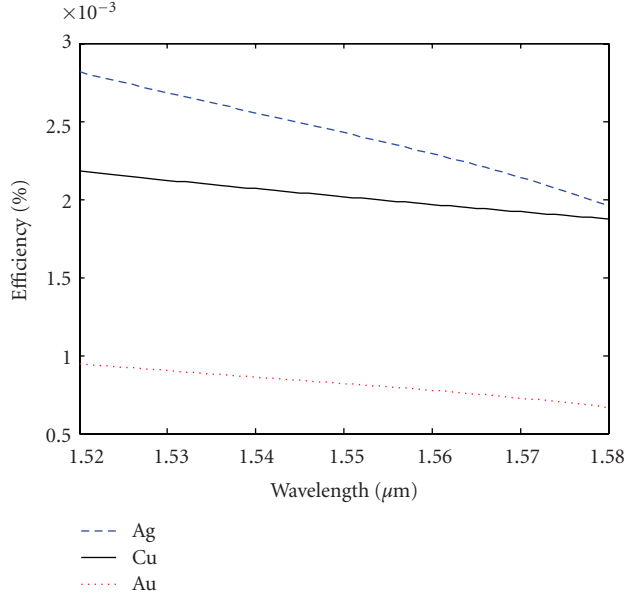


FIGURE 4: Calculated quantum efficiency versus wavelength for devices without DBRs having various metals as top mirror: Ag (blue dashed line), Cu (black solid line), and Au (red dotted line).

TABLE 1: Optical and electrical properties for three metals: gold, silver, and copper.

Metal	Complex refractive index (N)	Mean free path (L_e) [μm]	Fermi level (E_F) (eV)	Potential barrier (Φ_B) (eV)
Au	0.174-j9.960	0.055	5.530	0.780
Ag	0.450-j9.290	0.057	5.480	0.780
Cu	0.145-j9.830	0.045	7.050	0.580

use of SOI substrate has been investigated extensively for the fabrication of Si-based photodetectors; this technique is particularly attractive given the widespread acceptance of SOI technology as a platform for high performance CMOS [22]. The benefits gained by using SOI substrates, due to the high index contrast of the buried oxide, would be the same offered by substrates constituted with more Si/SiO₂ pairs. Starting from these considerations, in our design we propose a DBR centred at 1.55 μm formed by 4 periods of Si/SiO₂ having thicknesses of 340 nm (limitations in fabrication process usually do not allow to realize a Si layer thickness as thin as $(\lambda/4n)$; for this reason a thickness of $(3\lambda/4n)$ was considered [20]) and 270 nm, respectively. Reflectivity of the proposed Si/SiO₂ DBR is 0.99 at 1550 nm.

In order to achieve an Ohmic contact, the top layer of the DBR is supposed to be realized by a very thin but heavily doped 10^{19} cm^{-3} silicon layer. Concerning the top reflector of the resonant cavity, we consider three metals: gold, silver, and copper, whose optical and electrical properties are summarized in Table 1 [21, 23, 24].

The efficiency of the RCE-PD is given by (5) [17]

$$\eta = A_T F_e P_E \eta_c, \quad (5)$$

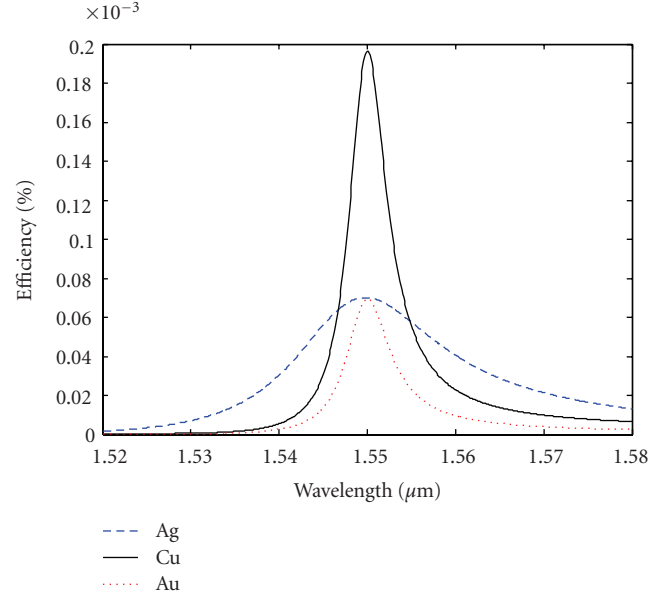


FIGURE 5: Calculated quantum efficiency versus wavelength for devices with DBRs formed by 4 Si/SiO₂. Top mirror is realized with various metals: Ag (blue dashed line), Cu (black solid line), and Au (red dotted line).

where A_T is the total optical absorbance of the metal while F_e , P_E , and η_c have been previously introduced. The cavity effect is taken into account in the calculation of the A_T factor, which has been carried out by using a transfer matrix method (TMM) [24, 25].

3.2. Absorbance Calculation and Quantum Efficiency. In order to estimate the quantum efficiency, the calculation of the absorbance (A_T) is numerically carried out by TMM. Normal incidence condition and the restriction to variations of $n(z)$, that is, the unidimensional refractive index profile, along the propagation direction (z) are taken into account.

Let us consider a general structure for proposed photodetector in which layer 3 is the absorbing material (Figure 3).

As shown in Figure 3, let $E_{2,F}$ ($E_{4,F}$) and $E_{2,B}$ ($E_{4,B}$) be the frequency domain electric field complex amplitudes of the forward and backward travelling plane waves in layer 2 (layer 4); the total powers incident on and going out from the metal are

$$\begin{aligned} P_{\text{input}} &= \frac{n_2}{2\eta_0} |E_{2,F}|^2 + \frac{n_4}{2\eta_0} |E_{4,B}|^2 \\ &= \left(n_2 \left| \frac{M_{A11}}{M_{TOT11}} \right|^2 + n_4 \left| \frac{M_{B21}}{M_{TOT11}} \right|^2 \right) \frac{|E_{\text{inc}}|^2}{2\eta_0}, \\ P_{\text{output}} &= \frac{n_2}{2\eta_0} |E_{2,B}|^2 + \frac{n_4}{2\eta_0} |E_{4,F}|^2 \\ &= \left(n_2 \left| \frac{M_{A21}}{M_{TOT11}} \right|^2 + n_4 \left| \frac{M_{B11}}{M_{TOT11}} \right|^2 \right) \frac{|E_{\text{inc}}|^2}{2\eta_0}, \end{aligned} \quad (6)$$

where η_0 is the vacuum characteristic impedance.

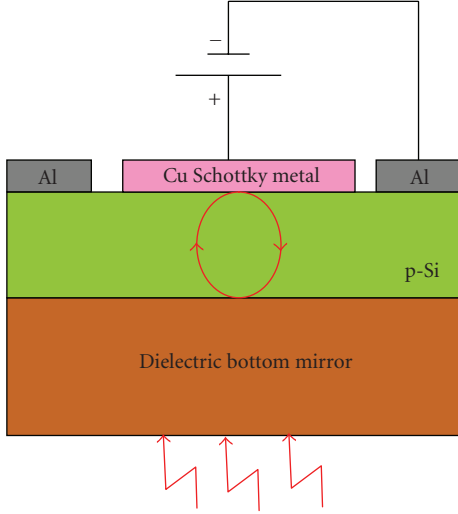


FIGURE 6: Schematic cross-section of the proposed back-illuminated RCE Schottky photodetector.

Air being the first layer considered ($n_1 = 1$) and P_{inc} being the power incident on the whole system, absorbance in the metal layer is given by

$$A_T = \frac{P_{input} - P_{output}}{P_{inc}} = \left\{ \left(n_2 \left| \frac{M_{A_{11}}}{M_{TOT_{11}}} \right|^2 + n_4 \left| \frac{M_{B_{21}}}{M_{TOT_{11}}} \right|^2 \right) - \left(n_2 \left| \frac{M_{A_{21}}}{M_{TOT_{11}}} \right|^2 + n_4 \left| \frac{M_{B_{11}}}{M_{TOT_{11}}} \right|^2 \right) \right\} \quad (7)$$

where n_2 and n_4 are the real parts of the refractive index of the 2th and 4th layer, respectively.

We point out that we could apply the power balance to the whole device instead that to the only metal layer, but, in this case, we would have considered also the absorbance contribution due to the layer heavily doped on top of the DBR necessary to achieve Ohmic contact (Figure 2).

A_T depends critically upon the metal thickness. The value of thickness must be a compromise between the top reflectivity value and the absorbance of metal layer. In order to calculate the maximum absorbance, the resonance condition must be imposed

$$2\beta(\lambda_0)L + \psi_1(\lambda_0) + \psi_2(\lambda_0) = 2\pi, \quad (8)$$

where $\beta = 2n\pi/\lambda_0$ is the propagation constant, L is the thickness of silicon cavity and, ψ_1 and ψ_2 are the phases introduced by the top and bottom mirror, respectively.

An analytical formulation of the quantum efficiency for a simplified RCE-PD structure with lossless mirrors was given by Kishino et al. [26]. In the case of an absorbing mirror, such as the semitransparent metallic top mirror of RCE Schottky PDs, the previous formulation is no longer valid. Therefore, in order to calculate the device maximum

TABLE 2: Cavity parameter coming out from our simulations.

Metal	Cavity thick-ness (L) [μm]	thick-ness (d) [nm]	R_1	Ψ_1 [rad]	A_T	Q value
Au	0.420	30	0.920	-2.140	0.780	525
Ag	0.410	20	0.730	-2.110	0.930	153
Cu	0.420	32	0.930	-2.360	0.740	585

quantum efficiency, the following methodology has been adopted:

- (1) bottom-mirror reflectivity and phase (R_2 , ψ_2) have been calculated. They result in 0.990 and 3.11 rad, respectively,
- (2) top-mirror reflectivities and phases (R_1 , ψ_1) have been calculated for metal thicknesses ranging from 0 to 50 nm consequently, the value of silicon cavity thickness yielding a resonance condition can be obtained by (8). Finally, the resulting absorbance is calculated using (7). We obtain a curve of absorbance depending on the metal thickness in the range of 0–50 nm and we consider the maximum,
- (3) dielectric coating thickness, chosen in order to avoid perturbation of resonance condition, is a Si_3N_4 layer, having refractive index 2.0 and thickness of 390 nm, and
- (4) at this point, the parameters of the optimized cavity are fixed and the quantum efficiency as a function of wavelength in the range of interest can be calculated using (1)–(5), (7).

The parameters calculated by the aforementioned methodology have been summarized in Table 2.

Efficiency versus wavelength for various metals has been reported for a device without DBR in Figure 4 and with DBR in Figure 5, respectively.

It is worth noting that a significant quantum efficiency enhancement of two order of magnitude is achieved by using a resonant cavity structure. We note that the copper top contact cavity has the best quantum efficiency (about 0.2%, corresponding to a responsivity of 2.5 mA/W at 1550 nm) and selectivity due to its lower potential barrier and to its higher reflectivity, respectively. It is interesting in comparing gold and silver, due to the same value of barrier (Table 1), we get the same order of efficiency (about 0.06%, corresponding to a responsivity of 0.75 mA/W at 1550 nm), but in the case of gold a better selectivity, due to the higher reflectivity, is obtained.

4. Back-Illuminated Device

4.1. Proposed Device. The sketch of the proposed back-illuminated device is shown in Figure 6.

The resonant cavity is a surface normal Fabry-Perot structure. It is formed by a dielectric bottom mirror, a metallic top mirror, and, in the middle, a silicon cavity. The advantage of a back-illuminated device is that the top

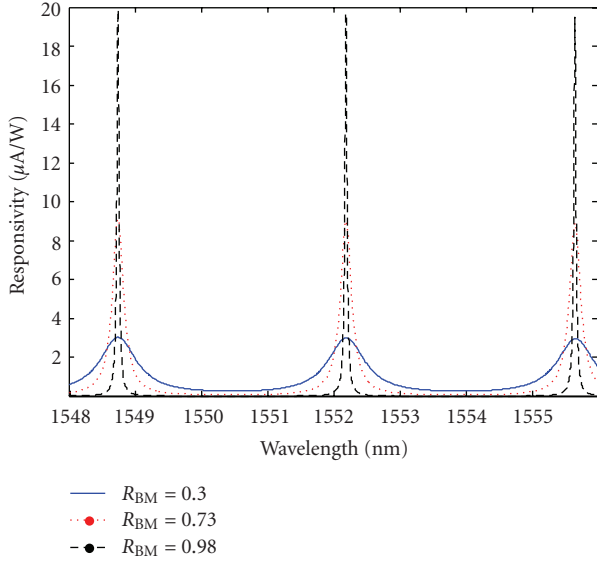


FIGURE 7: Responsivity versus Wavelength at bottom-mirror reflectivities (R_{BM}) of 0.3 (blue solid line), 0.73 (red dotted line), and 0.98 (black dashed line).

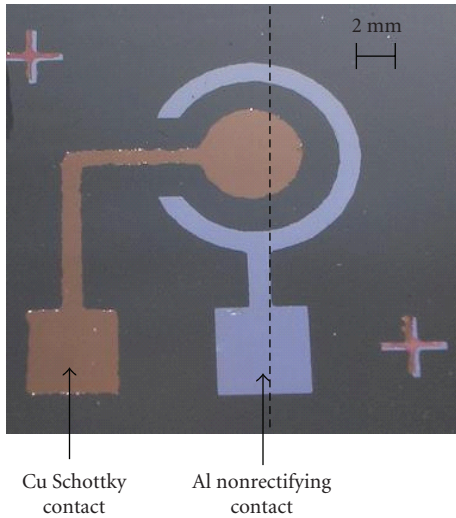


FIGURE 8: Top view of the back-illuminated realized photodetector.

mirror can be realized very thick reducing the importance of the roughness control during metal deposition process. The dielectric bottom reflector will be realized by alternating layers of amorphous hydrogenated silicon (a-Si:H) and silicon nitride (Si_3N_4) having $\lambda/4$ thicknesses.

4.2. Responsivity Calculation. By (1)–(5) and (7), devices having bottom-mirror reflectivities (R_{BM}) of 0.3 (reflectivity of a silicon/air interface), 0.73, and 0.98 were numerically investigated. All optical and electrical properties for silicon and copper used in our simulations are reported in Table 3 [21, 23–27].

TABLE 3: Optical and electrical properties for silicon and copper used in our simulations.

	Complex refractive index at 1550 nm	Thickness [μm]	Mean free path (L_e) [μm]	Fermi level (E_F) [eV]	Potential barrier (Φ_B) [eV]
Copper (Cu)	0.145-j9.830	0.20	0.045	7.050	0.720
Silicon	3.48	100	—	—	—

TABLE 4: Cavity parameters coming out from our simulations.

	Peak responsivity [$\mu\text{A/W}$]	Cavity finesse
Cu/p-Si photodiode with bottom reflectivity at 1550 nm of 0.30	3	4.7
Cu/p-Si photodiode with bottom reflectivity at 1550 nm of 0.73	9.1	16.5
Cu/p-Si photodiode with bottom reflectivity at 1550 nm of 0.98	19.9	89

In Figure 7, responsivity (linked to the efficiency by the formula: $R = (\lambda[\text{nm}]/1242)\eta$) versus wavelength at various bottom-mirror reflectivities is reported.

The results coming out of our simulation are summarized in Table 4.

In all cases, the free spectral range is 3.3 nm. It is worth noting that a responsivity enhancement is achieved by using resonant cavity structure at higher finesse. The maximum responsivity of $19.9 \mu\text{A/W}$ obtained in our simulations is about two orders of magnitude lower compared with the top-illuminated structure numerically investigated above. This is expected from the fact that in top illuminated structure the goal was to optimize the device in order to get the highest efficiency while in this back-illuminated structure the layer thicknesses are chosen taking into account our capability to realize a preliminary device in order to make a comparison between theoretical and experimental data.

4.3. Device Fabrication. In order to validate our numerical results, we only fabricated back-illuminated structures in two variants: one with high-reflectivity bottom mirror realized with 5 pairs of a-Si:H/ Si_3N_4 and one with a low reflectivity bottom mirror realized with simple silicon/air interface. Both structures have been provided by Cu metal working as the top mirror.

The samples were fabricated starting from a slightly doped (10^{14} cm^{-3}) p-type bi-polished $100\text{-}\mu\text{m}$ -thick silicon wafer.

The collecting ohmic contact was realized on the top of the samples. The collecting contact was made by a 200-nm -thick aluminum film, thermally evaporated at $3 \cdot 10^{-6}$ mbar and 150°C , and patterned by a lift-off process of photoresist Shipley S1813 which, deposited by a spincoater at 4000 rpm, has a thickness of $1.4 \mu\text{m}$. Then, an annealing at 475°C in

TABLE 5: Value of thicknesses and refractive indices as calculated.

	\bar{D} [nm]	n_{1550}
a-Si:H	108	3.58
Si ₃ N ₄	220	1.82

nitrogen for 30 min, in order to get a not-rectifying behavior, was carried out [28].

On the back of one device, a multilayer Bragg mirror was fabricated by Plasma Enhanced Chemical Vapor Deposition technique (PECVD). The mirror is composed by a quarter-wave stack of a-Si:H and Si₃N₄ layers, having nominal refractive index, at 1550 nm, of 3.52 and 1.82, respectively. Silicon nitride was deposited at pressure of 1.2 mbar, temperature of 250°C, at 30 W of RF power. In the deposition chamber, 10 sccm of NH₃, 88 sccm of SiH₄ (5% in He), and 632 sccm of N₂ were flowed. The deposition rate is 22.93 nm/min, and the suitable Si₃N₄ thickness was obtained with a process time of 9 min and 17 sec. The amorphous hydrogenated silicon, instead, was deposited at pressure of 0.8 mbar, temperature of 250°C, power of 2 W, and a SiH₄ (5% in He) flow of 600 sccm. The a-Si:H deposition rate is 3.15 nm/min, and the suitable thickness was obtained with a process time of 34 min and 56 sec.

Finally, the Schottky contact was fabricated on top of both samples. Copper was thermally evaporated and patterned by liftoff, so obtaining a metal thickness of 200 nm, thicker than optical field penetration depth. The collecting contact and the Schottky contact are shaped by a ring and a disk having radius of about 2 mm, as shown in Figure 8.

4.4. Device Characterization

4.4.1. Bragg Mirror Reflectivity Characterization. As far as the realization of our device is concerned, the crucial point is the Bragg mirror. Bragg reflectivity measurements were carried out by means of Spectroscopic Ellipsometry (SE) [29, 30]. Spectroscopic ellipsometric data were acquired by a Jobin Yvon UVISSEL-NIR phase-modulated spectroscopic ellipsometer apparatus, at 70° angle of incidence, operating from 280 to 1600 nm. The optical properties of a-Si:H and Si₃N₄, that is, the complex refractive index dispersion spectra, were calculated using the Tauc-Lorentz dispersion model [31–33]. The thicknesses and the refractive indices at $\lambda = 1550$ nm, for both a-Si:H and Si₃N₄ films, are summarized in Table 5.

The Bragg mirror theoretical model is composed by five distinct pairs of a-Si:H/Si₃N₄ layers, deposited on single-crystal silicon substrate, and by a superficial roughness, modelled by a Bruggeman effective medium approximation (EMA) [34], and consisting of 50% of air and 50% of a-Si. The fitting procedure between the experimental data and the theoretical model was executed using the Levenberg-Marquardt algorithm and returned a fit goodness factor $\chi^2 = 2.9$. Starting from the results shown in Table 5, a simulated reflectivity at normal incidence has been reported in Figure 9 (solid line).

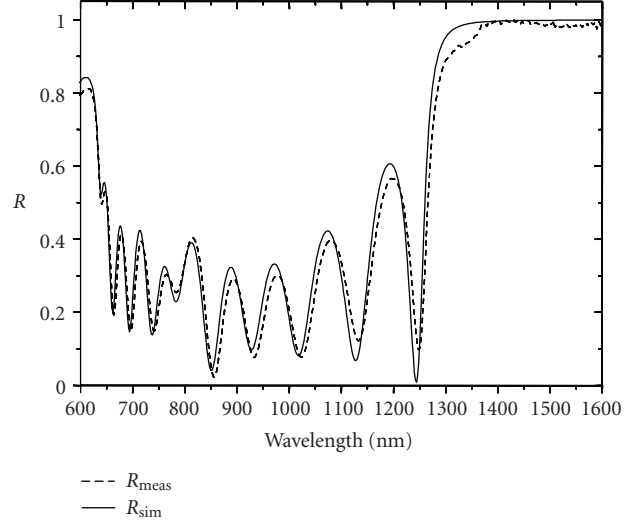


FIGURE 9: Measured and simulated reflectivity of the Bragg mirror, formed by 5 pairs of a-Si:H/Si₃N₄, from 600 to 1600 nm at normal incidence.

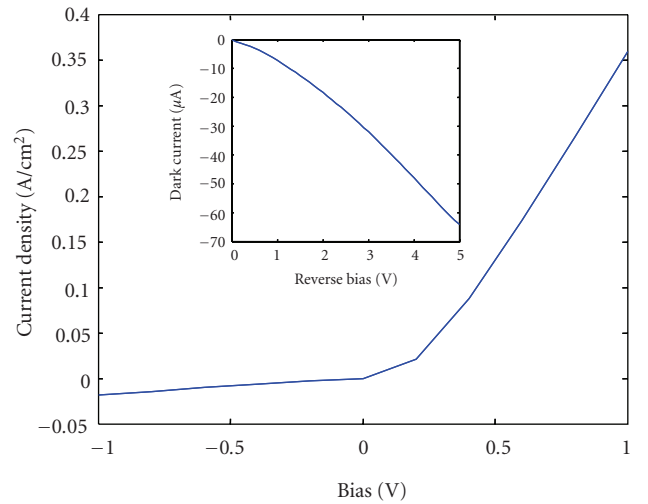


FIGURE 10: J-V characteristic of the realized Cu/p-Si Schottky diode. The inset shows diodes dark current.

Finally, the reflectivity spectra of the Bragg reflector was measured at normal incidence by means of a Y optical reflection probe (Avantes), connected to a white light source and to an optical spectrum analyzer (Ando, AQ6315B). The comparison between simulated and measured (dotted line) Bragg mirror reflectivity, for light normally incident in the range 600–1600 nm, is reported in Figure 9.

4.4.2. Electrical Characterization. Typical density current-voltage (J-V) curve of Cu/p-Si diode, obtained by a parameter analyzer (Hewlett Packard 4145B), is depicted in Figure 10.

The Schottky barrier height (SBH) was deduced fitting the experimental J-V characteristic, in the forward bias

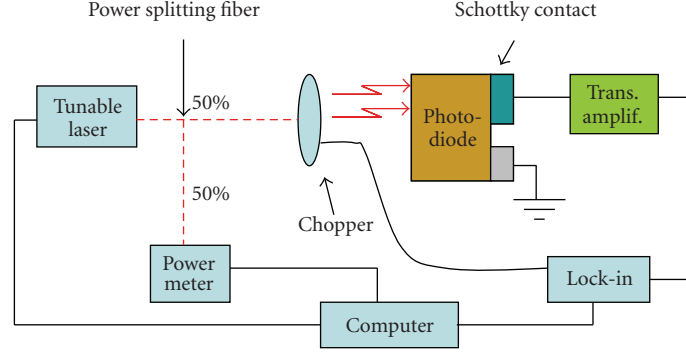


FIGURE 11: Experimental setup for external responsivity measurements.

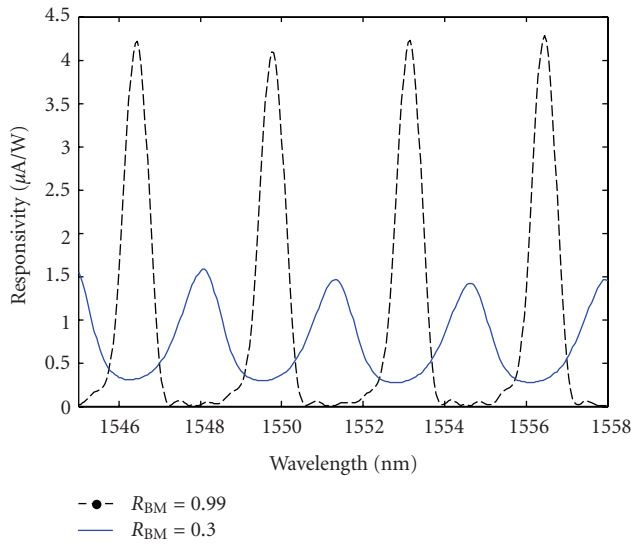


FIGURE 12: Measured responsivity versus wavelength for two realized devices: having bottom mirror reflectivity (R_{BM}) of 0.3 (blue solid line) and 0.99 (black dashed line), respectively.

region, to the following equation of the Schottky diode (9) [18]:

$$J = A^{**} T^2 e^{-\Phi_B/V_T} \left(e^{-((V - R_s I)/\eta V_T)} - 1 \right), \quad (9)$$

where R_s is the series resistance, Φ_B the potential barrier, η the ideality factor, T the absolute temperature, and V_T is the thermal voltage. The calculated SBH is 0.72 ± 0.01 eV.

The maximum detectable wavelength is given by (10):

$$\lambda_{\max} [\text{nm}] = \frac{1242}{\phi_B}. \quad (10)$$

We obtain that Cu/p-Si photodiodes are able to detect wavelengths up to 1725 nm.

4.4.3. Optical Characterization. The experimental set-up for external responsivity measurements is shown in Figure 11. The laser beam emitted by a wavelength tunable laser is split by a Y fiber junction. One branch is used to monitor the

optical power, while the other one is collimated, chopped, and sent onto the device. The photocurrent produced by our device is measured by a lock-in amplifier. A transimpedance amplifier is employed to provide a reverse bias to the photodetector and at the same time for reducing the dark current. The dark current cancellation circuit realised by using a transimpedance amplifier has a limited bandwidth; however, it is adequate for our scope, that is dc or quasistatic measurements [35].

Responsivity measurements were carried out in the range of 1545–1558 nm (step of 0.05 nm). Figure 12 shows the room temperature responsivity versus the wavelength in two conditions: device with a bottom-mirror reflectivity (R_{BM}) of 0.3 (blue solid line) and 0.99 (black dashed line), respectively. The measured free spectral range of 3.3 nm agrees with the value numerically calculated. By looking at device having $R_{BM} = 0.3$, the measured cavity finesse F and responsivity are 2.9 and $1.6 \mu\text{A/W}$, respectively. Moving our attention to the device having $R_{BM} = 0.99$, we get a measured cavity finesse F and responsivity of 4.7 and $4.3 \mu\text{A/W}$, respectively.

By comparing Figures 7 and 12, we note that while the experimental and numerical free spectral range agree, as far as finesse and peak responsivity are concerned, experimental and numerical values show a discrepancy. In our opinion, such a discrepancy can be due to the cavity losses, which are not taken into account in our simulations. In fact, it is well known that if we assume a Fabry-Perot interferometer having ideal plane-parallel plates, the finesse is determined only by the reflectivity R of the mirrors. In practice, however, deviations of the surfaces from an ideal plane, slight inclinations of the two surfaces, and surface irregularities cause imperfect superposition of the interfering waves. This results in a broadening of the transmission peak and a decreasing of the total finesse [36].

5. Conclusions

In this paper, a new approach for sub-bandgap detection at $1.55 \mu\text{m}$ in Si-based devices is investigated. The proposed devices are RCE structures incorporating silicon photodetectors based on the internal photoemission effect. We investigated two types of structures: top and back illuminated.

Concerning the top-illuminated photodetectors, a device theoretical investigation has been carried out. A methodology based on TMM has been implemented in order to design and to optimize the structures. We proved that a significant enhancement in quantum efficiency, of about two orders of magnitude, can be achieved due to the effect of the Fabry-Perot microcavity. Moreover, a comparison among three different photodetectors, having as Schottky metal: gold, silver, or copper, was proposed. We proved that due to its lowest potential barrier, the best quantum efficiency has been obtained by considering copper as Schottky metal, demonstrating that the metal-silicon interface potential barrier plays a key role.

It is worthy noting that the fabrication of top illuminated devices could be not simple, in fact, the precise control of the thin metal thickness and an acceptably low defect concentrations are not trivial tasks. For these reasons, back illuminated devices constituted by a thick metal layer as top mirror have been realized.

Concerning the back-illuminated photodetectors, a theoretical and experimental investigation on devices having bottom mirror reflectivities of 0.3 and 0.99, respectively, have been carried out. Simulated and measured responsivities around 1550 nm show a good agreement from a qualitative point of view, demonstrating that the responsivity enhancement is strictly linked to the increased cavity finesse.

Even if the measured responsivities could be already suitable for power monitoring applications, we believe that our results could be further improved by investigating more complex microcavities at higher finesse (for example, ring resonator), which could be also very promising in the integration of photonic components with integrated circuit electronics enabling interconnection bandwidth that is not limited by the RC time constant and reliability constraints of metal lines.

References

- [1] L. C. Kimerling, L. Dal Negro, S. Saini et al., "Monolithic silicon microphotronics," in *Silicon Photonics*, L. Pavesi and D. J. Lockwood, Eds., vol. 94 of *Topics in Applied Physics*, pp. 89–119, Springer, Berlin, Germany, 2004.
- [2] B. Jalali and S. Fathpour, "Silicon photonics," *Journal of Lightwave Technology*, vol. 24, no. 12, pp. 4600–4615, 2006.
- [3] L. K. Rowe, M. Elsey, N. G. Tarr, A. P. Knights, and E. Post, "CMOS-compatible optical rib waveguides defined by local oxidation of silicon," *Electronics Letters*, vol. 43, no. 7, pp. 392–393, 2007.
- [4] L. Vivien, D. Pascal, S. Lardenois et al., "Light injection in SOI microwaveguides using high-efficiency grating couplers," *Journal of Lightwave Technology*, vol. 24, no. 10, pp. 3810–3815, 2006.
- [5] Q. Xu, S. Manipatruni, B. Schmidt, J. Shakya, and M. Lipson, "12.5 Gbit/s carrier-injection-based silicon micro-ring silicon modulators," *Optics Express*, vol. 15, no. 2, pp. 430–436, 2007.
- [6] C. P. Michael, M. Borselli, T. J. Johnson, C. Chrystal, and O. Painter, "An optical fiber-taper probe for wafer-scale microphotonic device characterization," *Optics Express*, vol. 15, no. 8, pp. 4745–4752, 2007.
- [7] A. Liu, L. Liao, D. Rubin et al., "High-speed optical modulation based on carrier depletion in a silicon waveguide," *Optics Express*, vol. 15, no. 2, pp. 660–668, 2007.
- [8] A. Liu, H. Rong, R. Jones, O. Cohen, D. Hak, and M. Paniccia, "Optical amplification and lasing by stimulated Raman scattering in silicon waveguides," *Journal of Lightwave Technology*, vol. 24, no. 3, pp. 1440–1455, 2006.
- [9] T. K. Liang, H. K. Tsang, I. E. Day, J. Drake, A. P. Knights, and M. Asghari, "Silicon waveguide two-photon absorption detector at 1.5 μm wavelength for autocorrelation measurements," *Applied Physics Letters*, vol. 81, no. 7, p. 1323, 2002.
- [10] J. D. B. Bradley, P. E. Jessop, and A. P. Knights, "Silicon waveguide-integrated optical power monitor with enhanced sensitivity at 1550 nm," *Applied Physics Letters*, vol. 86, no. 24, Article ID 241103, 3 pages, 2005.
- [11] H. Chen, X. Luo, and A. W. Poon, "Cavity-enhanced photocurrent generation by 1.55 μm wavelengths linear absorption in a p-i-n diode embedded silicon microring resonator," *Applied Physics Letters*, vol. 95, no. 17, Article ID 171111, 2009.
- [12] S. Zhu, M. B. Yu, G. Q. Lo, and D. L. Kwong, "Near-infrared waveguide-based nickel silicide Schottky-barrier photodetector for optical communications," *Applied Physics Letters*, vol. 92, no. 8, Article ID 081103, 2008.
- [13] A. Akbari and P. Berini, "Schottky contact surface-plasmon detector integrated with an asymmetric metal stripe waveguide," *Applied Physics Letters*, vol. 95, no. 2, Article ID 021104, 2009.
- [14] Y. Wang, X. Su, Y. Zhu et al., "Photocurrent in Ag-Si photodiodes modulated by plasmonic nanopatterns," *Applied Physics Letters*, vol. 95, no. 24, Article ID 241106, 2009.
- [15] W. F. Kosonocky, F. V. Shallcross, T. S. Villani, and J. V. Groppe, "160 \times 244 element PtSi Schottky-barrier IR-CCD image sensor," *IEEE Transactions on Electron Devices*, vol. 32, no. 8, pp. 1564–1573, 1986.
- [16] R. H. Fowler, "The analysis of photoelectric sensitivity curves for clean metals at various temperatures," *Physical Review*, vol. 38, no. 1, pp. 45–56, 1931.
- [17] V. E. Vickers, "Model of Schottky barrier hot-electron-mode photodetection," *Applied Optics*, vol. 10, no. 9, pp. 2190–2192, 1971.
- [18] S. M. Sze, *Physics of Semiconductor Devices*, John Wiley & Sons, New York, NY, USA, 1981.
- [19] H. X. Yuan and A. G. U. Perera, "Dark current analysis of Si homojunction interfacial work function internal photoemission far-infrared detectors," *Applied Physics Letters*, vol. 66, no. 17, pp. 2262–2264, 1995.
- [20] M. K. Emsley, O. Dosunmu, and M. S. Ünlü, "Silicon substrates with buried distributed Bragg reflectors for resonant cavity-enhanced optoelectronics," *IEEE Journal on Selected Topics in Quantum Electronics*, vol. 8, no. 4, pp. 948–955, 2002.
- [21] E. Y. Chan and H. C. Card, "Near IR interband transitions and optical parameters of metal-germanium contacts," *Applied Optics*, vol. 19, no. 8, pp. 1309–1315, 1980.
- [22] G. G. Shahidi, "SOI technology for the GHz era," *IBM Journal of Research and Development*, vol. 46, no. 2-3, pp. 121–131, 2002.
- [23] E. Y. Chan, H. C. Card, and M. C. Teich, "Internal photoemission mechanisms at interfaces between germanium and thin metal films," *IEEE Journal of Quantum Electronics*, vol. 16, no. 3, pp. 373–381, 1980.
- [24] P. Yeh, *Optical Waves in Layered Media*, John Wiley & Sons, New York, NY, USA, 1988.

- [25] M. A. Muriel and A. Carballar, "Internal field distributions in fiber Bragg gratings," *IEEE Photonics Technology Letters*, vol. 9, no. 7, pp. 955–960, 1997.
- [26] K. Kishino, M. S. Unlu, J. Chyi, J. Reed, L. Arsenault, and H. Morkoc, "Resonant cavity-enhanced (RCE) photodetectors," *IEEE Journal of Quantum Electronics*, vol. 27, no. 8, pp. 2025–2034, 1991.
- [27] E. D. Palik, *Handbook of Optical Constants of Solids*, Academic Press, San Diego, Calif, USA, 1985.
- [28] H. C. Card, "Aluminum-silicon Schottky barriers and ohmic contacts in integrated circuits," *IEEE Transactions on Electron Devices*, vol. 23, no. 6, pp. 538–544, 1976.
- [29] K. Vedam, "Spectroscopic ellipsometry: a historical overview," *Thin Solid Films*, vol. 313–314, pp. 1–9, 1998.
- [30] G. E. Jellison Jr., "The calculation of thin film parameters from spectroscopic ellipsometry data," *Thin Solid Films*, vol. 290–291, pp. 40–45, 1996.
- [31] G. E. Jellison Jr. and F. A. Modine, "Parameterization of the optical functions of amorphous materials in the interband region," *Applied Physics Letters*, vol. 69, no. 3, pp. 371–373, 1996.
- [32] G. E. Jellison Jr., F. A. Modine, P. Doshi, and A. Rohatgi, "Spectroscopic ellipsometry characterization of thin-film silicon nitride," *Thin Solid Films*, vol. 313–314, pp. 193–197, 1998.
- [33] P. Doshi, G. E. Jellison Jr., and A. Rohatgi, "Characterization and optimization of absorbing plasma-enhanced chemical vapor deposited antireflection coatings for silicon photovoltaics," *Applied Optics*, vol. 36, no. 30, pp. 7826–7837, 1997.
- [34] D. E. Aspnes, J. B. Theeten, and F. Hottier, "Investigation of effective-medium models of microscopic surface roughness by spectroscopic ellipsometry," *Physical Review B*, vol. 20, no. 8, pp. 3292–3302, 1979.
- [35] S. Donati, *Photodetectors: Devices, Circuits, and Applications*, Prentice Hall PTR, Upper Saddle River, NJ, USA, 1999.
- [36] W. Demtroder, *Laser Spectroscopy: Vol. 1: Basic principles*, chapter 4, Springer, Berlin, Germany, 2008.